In Situ Direct-Write Materials Processing Methods in Electron Microscopes

A Dissertation Presented for the
Doctor of Philosophy
Degree
The University of Tennessee, Knoxville

John Charles Lasseter
August 2024

DEDICATION

This work is dedicated to:

Christina Scarlett Franklin

ACKNOWLEDGEMENTS

I would like to thank my wife, Scarlett, for supporting me in this long journey. I'd also like to thank my family and friends who helped me get here today. My fellow graduate students Reece, Spencer, Kyle, Matt, David and Grace deserve heartfelt appreciation for all the help, collaboration, and camaraderie shared over the years. A special thanks to Oak Ridge National Lab and the Center for Nanophase Materials Science staff and facilities who made this all possible through years of training and assistance. Additionally, I'd like to thank my advisors Philip Rack and committee members Steven Randolph, Dustin Gilbert and Gong Gu for the invaluable help, patience, and support shown over the years. Finally, I'd also like to thank my internship advisor Mina Yoon, my undergraduate research advisors Adrienne Friedli and Piotr Kaszynski for starting me on this path in undergraduate school.

ABSTRACT

Focused beam induced processing holds great promise for advanced nanoscale device design and prototyping but often has severe limitations in material quality, purity and compatibility. In particular focused electron beam induced deposition (FEBID) can create 3D nanostructures of extremely complex geometries, but the deposited material purity is often very low (< 10% metal). *Ex situ* functionalization processes, such as sputter coating, do not conformally coat the nanostructures but instead apply pure material from the top down. Here, a laser based photothermal coating method leveraging the geometry-dependent thermal transport properties is used to apply high-quality pure material conformally coat the exposed nanostructures and is not limited to a specific nanostructure or substrate material. Additionally, focused electron beam induced etching (FEBIE) is used to investigate a low damage, chemical etching process of the transition metal dichalcogenide MoS_2 [Molybdenum disulfide] in contrast to more common, but much more damaging physical methods like focused ion beam (FIB) patterning. Experimental techniques such as scanning electron microscopy (SEM), scanning transmission electron microscopy (STEM), atomic force microscopy (AFM), energy dispersive spectroscopy (EDS/EDX), Raman and photoluminescence spectroscopy are used to fully characterize the investigated processes and materials. Additionally, finite element modeling (FEM) and automated SEM video analysis are employed to investigate the time dependent dynamics of the processes.

TABLE OF CONTENTS

LIST OF TABLES

LIST OF FIGURES

Introduction

Motivation

The primary motivations of this research are to advance the prototyping capabilities of electron microscopes by: (1) developing a direct-write chemical vapor deposition technique for the functionalization of nanostructures primarily created through focused electron beam induced deposition, (2) refine that photothermal process for functional device usage and (3) characterize the electron-beam induced etching of transition metal dichalcogenides for next-generation devices.

Literature Review

Direct-Write Nanofabrication

After the integrated circuit revolutionized device fabrication and vacuum-tubes were replaced with transistors, industry created millimeter-scale devices before turning toward the microscale and found massive improvements year-over-year. Devices were usually made using an indirect-write process called photolithography, roughly translating to “light writing on stone”. To create a device lithographically, a liquid with a dissolved organic polymer is placed on a surface, spun at high speeds and then baked to form a thin film. This film is then exposed to high-energy light through a stencil, which, similar to painting, shows the pattern by the gaps of the stencils. Metaphorically in the same way a poster can be created by using the right stencils complex devices utilize lithographic stencils (masks).

There are different kinds of polymer resists to expose. For a positive resist, where there are gaps in the mask and the light is allowed to shine through, the polymer is modified by the exposure

and breaks down leaving the surface exposed only in those areas, but the rest is still coated by a thin film of unexposed and stable polymer. Negative resists do the opposite, the exposure strengthens the polymer and makes it resistant to dissolution; the two are schematically compared in Figure 1.

After a resist pattern has been defined, subtractive or additive process are used to create useful devices. Other materials can be placed on the device and the pattern realized by removal of the thin polymer layer by a solvent like isopropyl alcohol or acetone, or the substrate itself can be etched away for functionality. Then a solvent is chosen that does not dissolve deposits or the substrate, the material in the exposed areas are stuck to the surface, and the rest of it washes off as the polymer dissolves. These processes are overviewed in Figure 2. The process is 'indirect' as we must make a pattern and do some extra processing to realize the final device – what we write, or pattern with traditional lithography methods is not directly our desired result, simply a steppingstone to it.

Unfortunately, these indirect processes become much more expensive and challenging at the nanoscale which has led to incremental progress in industry and deviation from Moore's law. Direct-write processes, in contrast, can also create flat pseudo-2D devices but require fewer processing steps to realize the result leading to more complex devices with a fast-prototyping cycle. More importantly, complex 3D structures are comparatively trivial to create via direct write methods. Several direct-write nanostructure fabrication methods are overviewed, but electron/ion beam based fabrication methods are arguably the most flexible and accessible available.

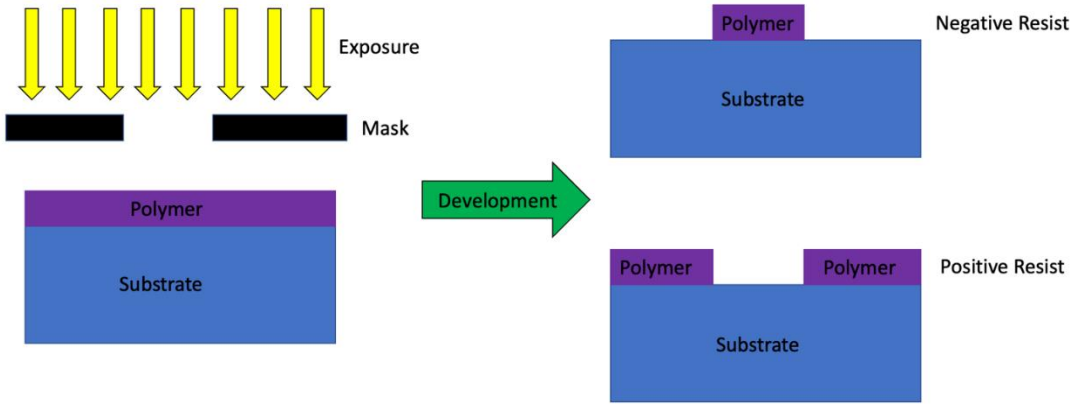

Figure 1. A comparison of negative and positive photoresists, and the exposure process using a traditional photomask mask. In electron-beam lithography, no photomask is used; the exposure is a single focused point exposure instead of a wide flood exposure.

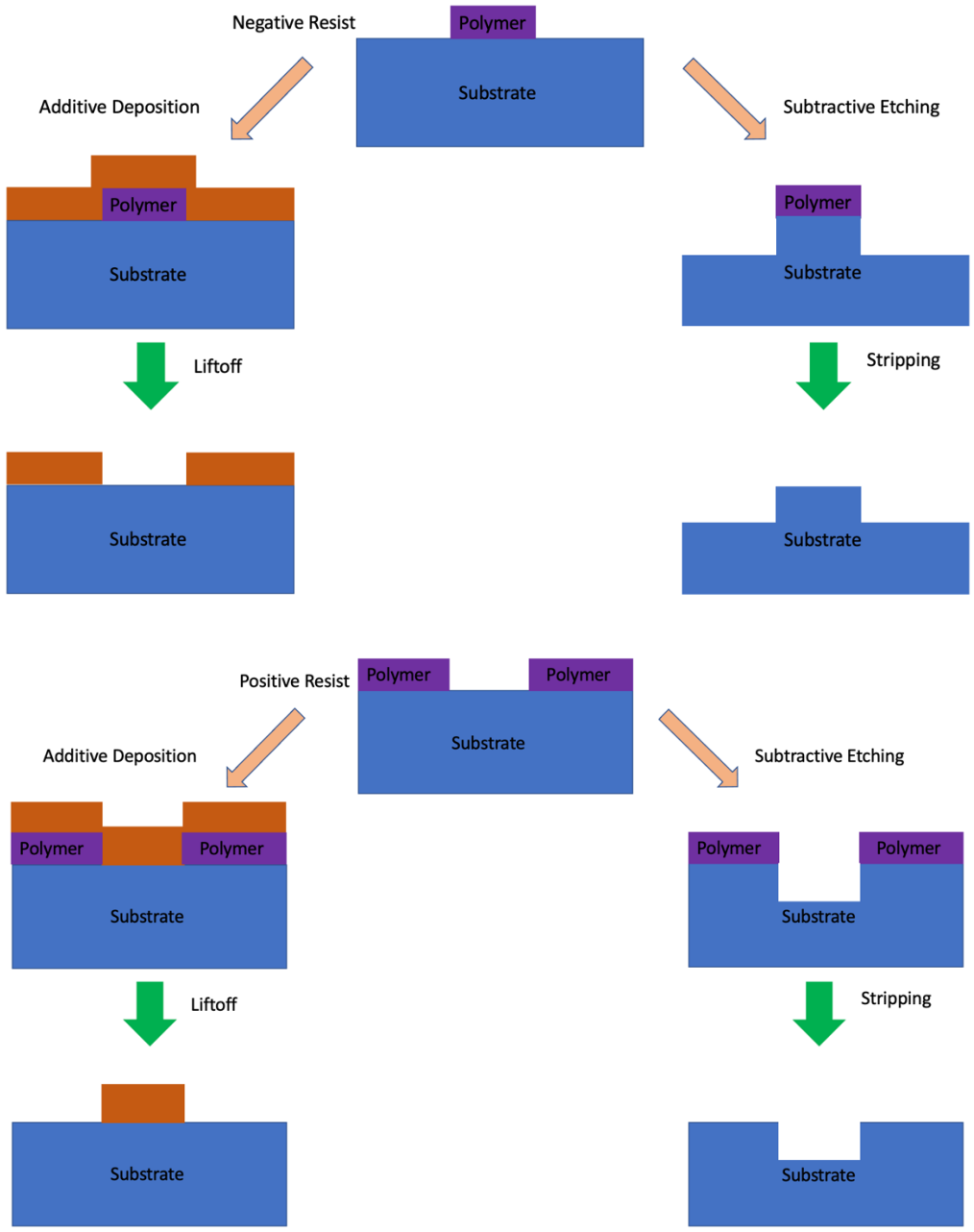

Figure 2. A schematic representation of negative and positive photoresist comparing their use in substrate modification using additive and subtractive processes.

One common direct-write nanofabrication process is through the use of ‘inks’, which is material dissolved in a solvent. Many modern printers utilize the concept, termed ‘inkjet’, but the results are far too large for nanoscale usage – patterned features are usually greater than 100 micrometers.[1] Dip-pen nanolithography utilizes an atomic force microscope (AFM) tip, which is simply a tiny pyramid on an oscillating lever that moves over the surface with the pyramid tip, the process was described in a review by Zhang, *et.al.* and is schematically shown in Figure 3. Surface information and images can be derived from how the lever is affected by the surface-tip contact.

In order to utilize the AFM technique as a fabrication method material is purposefully fed to the tip as it is moved along the surface, which leaves behind a trace forming solid structures. In thermal dip-pen heat can be used to melt metals placed on the tip, which allows the direct production of structures composed of otherwise difficult to manipulate metals, and deposition can be toggled on and off by heat control and cooling the material below its freezing point to stop the material flow. The ultimate spatial limit to the dip-pen process is debated, but reports show features around 10 nanometers are achievable.[1] 3D structures are generated in an additive fashion, by stacking 2D layers on top of each other rapidly. The same can technically be done with traditional lithography methods, but the lengthy and involved number of processing steps to create multiple layers in indirect-write methods is a magnet for defects and errors.

Another direct-write technique is electrohydrodynamic printing, where an electric field is used to guide the fluid material onto the surface, and with a scannable stage complex patterns can be directly written on the surface, which is shown in Figure 4.[2] The best reported resolution available with this technique is on the order of 10’s of nanometers; more recently, 30 nanometer

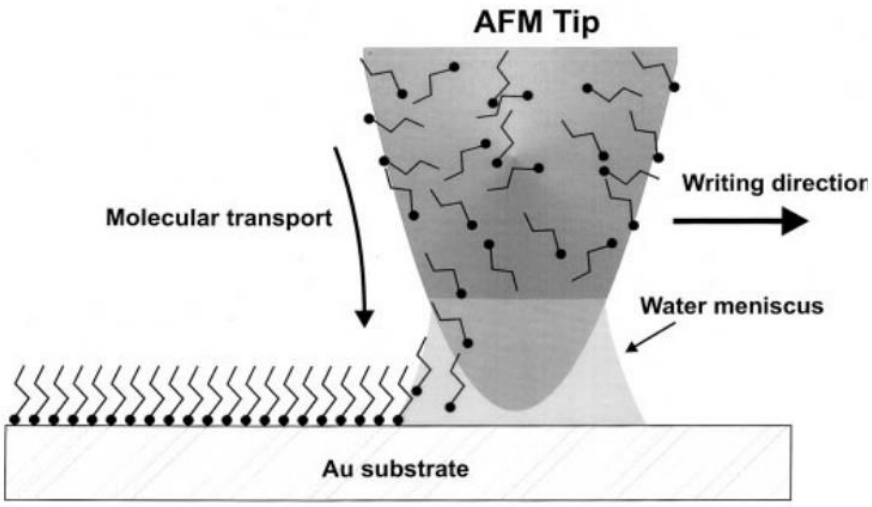

Figure 3. The Dip-Pen nanolithography method, which relies on the liquid molecular transport to the substrate delivered by a scanned atomic-force microscope tip. Figure reproduced from the review by Zhang, *et. al.*[1]. © 2009 IEEE.

features have been demonstrated.[3] Imprinting is an old technology, but recent nanoimprint lithography (NIL) achieves impressively small structures with high throughput, with the caveat ofmask fabrication. A resist layer is placed onto a surface, and the mask with the imprinting pattern mechanically deforms the resist, which can then be cured thermally or via UV. 6 nm dots and 10 nm holes have recently been reported.[4] Figure 5 outlines the mask-based process, the residual layer can directly be used as a nanostructure, or as a mask usable in traditional lithography processes for deposition or etching.

Another modern nanoscale method is two-photon lithography. A resist is coated on the surface, and electrons freed by the first photon are further energized at the laser focal point to induce crosslinking. After development, only the crosslinked regions remain. In 2022, 26 nm features were achieved with a 730 nm fs laser.[5] Figure 6 shows a schematic of the two-photon process.

Focused Electron Beam Induced Deposition and Etching

However, while there are many other interesting and functional 3D manufacturing methods electron/ion beam induced deposition (FEBID/FIBID) is perhaps the most developed, accessible, and flexible direct-write method available for nanoscale 3D structures. Figure 7 showcases some of the extreme complexity FEBID is capable of.

Features as small as 10 nm have been reported, and much progress has been made in accurately creating complex nanostructures via FEBID by detailed modeling, simulations[6,9–13] and 3D computer aided design infrastructure[14–16]. As shown in Figure 8, the nanostructures are created

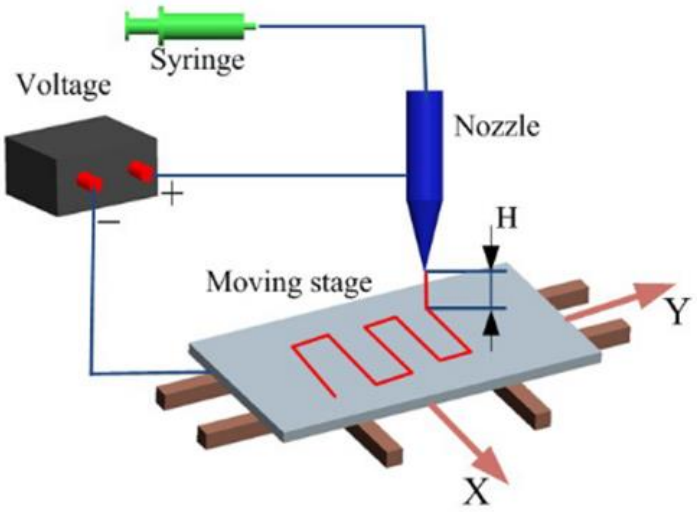

Figure 4. The electrohydrodynamic printing process, where a scanning stage with a bias applied between it and the printing nozzle guides the material onto the surface by electrostatic forces. Figure reproduced from Zhang, *et. al.*[2]. Used with permission of the Royal Society of Chemistry, from Micro/nanoscale electrohydrodynamic printing: from 2D to 3D, Zhang, Bing; He, Jiankang; Li, Xiao; Xu, Fangyuan; Li, Dichen, Volume 8, 2016; permission conveyed through Copyright Clearance Center, Inc.

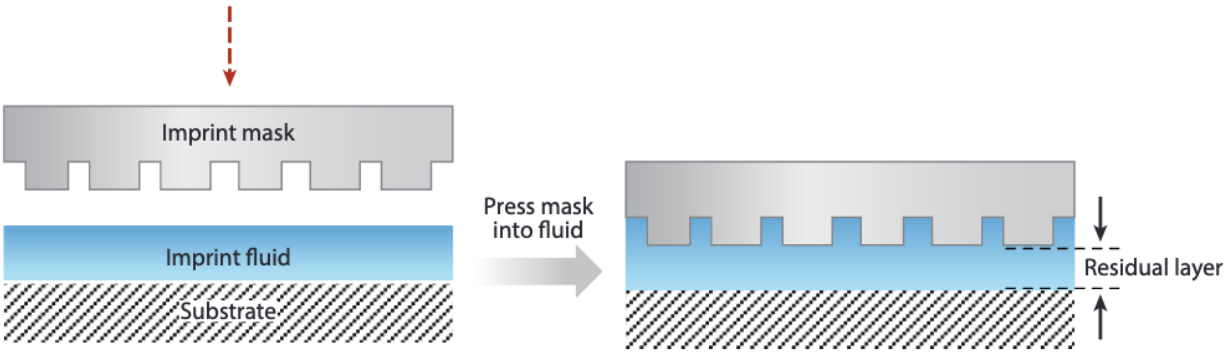

Figure 5. The nanoimprint lithography process, reproduced from Traub, *et. al.*[4] As shown, mechanical deformation of the resist is the key in this process, allowing nanometer structures that can be cured under the diffraction limit, or thermally. Used with permission of Annual Reviews, Inc., from Advances in Nanoimprint Lithography, Traub, Matthew C.; Longsine, Whitney; Truskett, Van N., Volume 7, 2010; permission conveyed through Copyright Clearance Center, Inc.

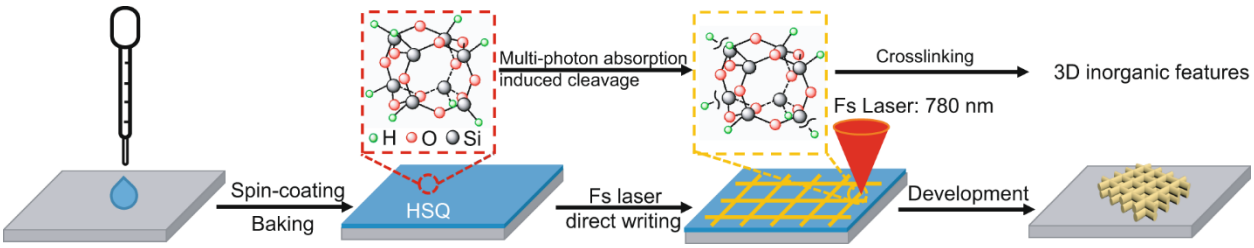

Figure 6. A schematic of two-photon lithography, where synchronized lasers with different λ's work in sync to crosslink-resist, while unexposed areas are washed away with development. Figure reproduced from Jin, *et. al.*[5] under a Creative Commons Attribution 4.0 International License (http://creativecommons.org/licenses/by/4.0/), with no changes made.

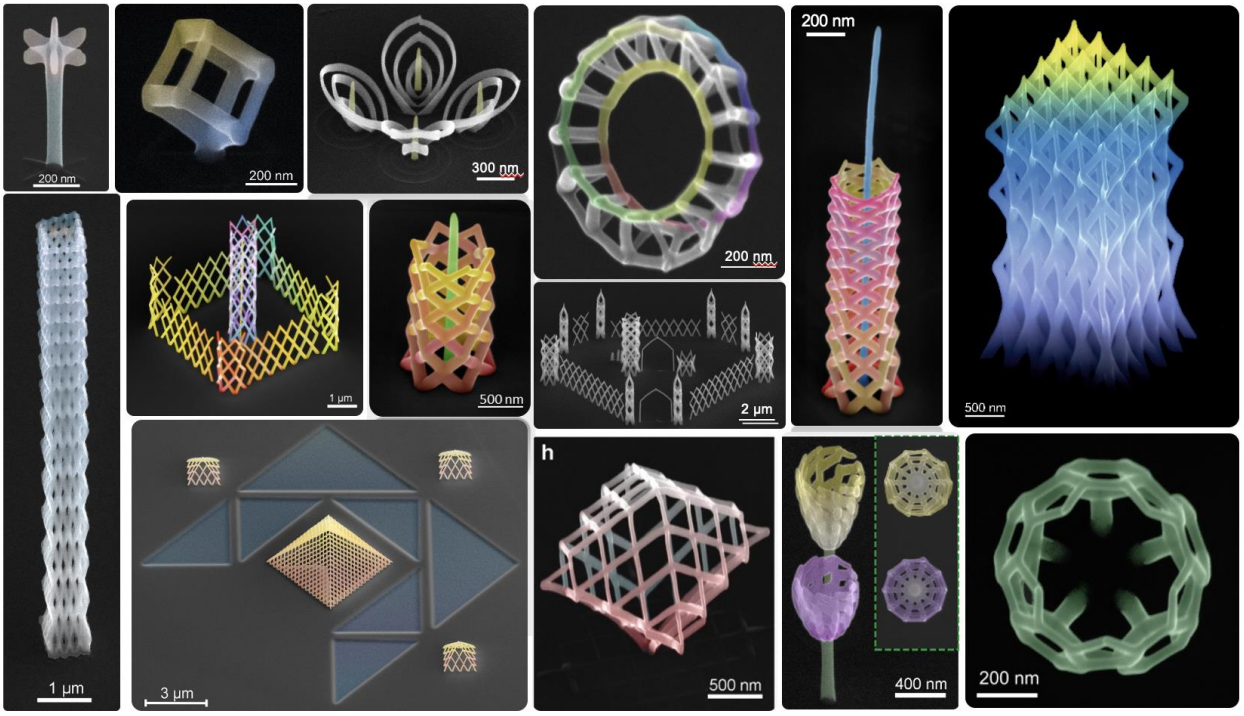

Figure 7. A collection of complex FEBID structures, images reproduced from literature and unpublished images[6–8]. Reprinted from Winkler, R.; Fowlkes, J. D.; Rack, P. D.; Plank, H. 3D Nanoprinting via Focused Electron Beams. *J. Appl. Phys.* **2019**, *125* (21), 210901, https://doi.org/10.1063/1.5092372, with the permission of AIP Publishing [7]. Reprinted (adapted) with permission from Winkler, R.; Schmidt, F.-P.; Haselmann, U.; Fowlkes, J. D.; Lewis, B. B.; Kothleitner, G.; Rack, P. D.; Plank, H. Direct-Write 3D Nanoprinting of Plasmonic Structures. *ACS Appl. Mater. Interfaces* **2017**, *9* (9), 8233–8240. Copyright 2017 American Chemical Society.

by flowing a precursor gas into the chamber where the gas is decomposed into solid structures by the incident beam.

There are several factors that influence beam-induced deposition. The beam energy, interaction volume, secondary electron (SE) escape volume and gas environment all have major impacts on the as-deposited structure. The deposition process is guided by primary electrons from the beam, but scattered secondary electrons produced through elastic and inelastic losses can decompose the precursor as well in the area around the deposited structure outside of the design. Higher beam energies lead to a tighter, higher-resolution beam which enables the deposition of narrow narrower structures while a lower energy beam leads to a higher electron concentration at the surface and larger, quick depositions. High energy beams efficiently pass through the structure as it forms, enabling accurate creation of standing 3D structures (Figure 7), but low energy beams induce unwanted deposition on lower levels as it passes through the structure which makes complex standing structures difficult to fabricate with low-energy FEBID due to the SE yield and distribution of low energy beams. The SE yield is influenced heavily by both the substrate and beam energy, but the SE energy distribution mainly depends on the nature of the substrate (work function, Fermi energy, and atomic number), but is less impacted by primary beam energy above 100 eV.[17] The SE yield has the largest impact on FEBID depositions, which in turn is driven by the penetration depth and interaction volume of the beam – thus, higher energy beams with high penetration depths have a lower SE yield at the surface which leads to the highly controlled depositions previously mentioned. There are similar arguments with FIBID, but due to ions having significant mass sputtering effects quickly become relevant. In FIBID with large ions, like gallium, the primary beam path sputters the deposited precursor away while the secondary electrons

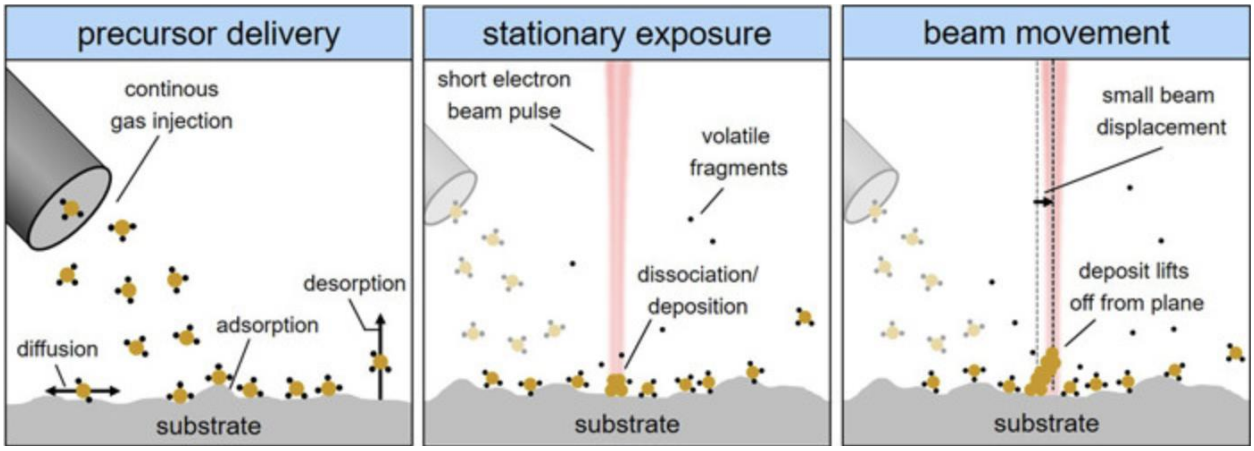

Figure 8. The FEBID/FIBID process showing how adsorbed gas species on the substrate are decomposed by the beam to deposit nanostructures. Reprinted from Winkler, R.; Fowlkes, J. D.; Rack, P. D.; Plank, H. 3D Nanoprinting via Focused Electron Beams. *J. Appl. Phys.* **2019**, *125* (21), 210901, https://doi.org/10.1063/1.5092372, with the permission of AIP Publishing [7].

continue to drive deposition in the immediate area and can lead to hollow pipe-like structures when depositing a nanorod. Due to sputtering efficiency lowering with increasing material atomic number and hardness, FIBID deposition with specific precursors, like $W(CO)_6$ shows more resistance to these sputtering effects. Additionally, atoms like Ga can also change the electronic properties of the substrate and deposition.

FEBID/FIBID comes with a few drawbacks. For starters, beam-induced deposition is difficult to parallelize, so large patterns take a long time on expensive microscopes. More importantly however is the material quality of the deposition – the organometallic precursors can create structures with as low as single digit percent of the desired metals, and over 90% amorphous carbon. There has been progress developing precursors with higher-purity deposits and various metal carbonyls have been explored with differing optimum metal content: $Cr(CO)_6$ – 20-40[18] at.%, $Mo(CO)_6$ – 8-20[19,20] at.%, $W(CO)_6$ – 37-58[21–23] at.%, $Fe(CO)_5$ – 80-95[24–26] at.%, $Fe_2(CO)_9$ – 80-93[27,28] at.%, $Co_2(CO)_8$ – 73-100[22,27,29–31] at.% and $Ni(CO)_4$ – 95[32] at.%. Additionally, several groups have explored subsequent coating processes[33], post-electron beam induced curing[34–39], co-deposition with purification gases[40,41], beam-induced post-purification with oxidizing[42–46] and reducing[47] precursors, post-deposition annealing[34,43,48–50], and synchronized pulsed laser FEBID[51,52]. Interestingly, FIBID enhances atomic rearrangement during the deposition due to elastic collisions, which can lead to higher-purity structures without extra purification efforts. In fact, the notoriously hard to metalize $(CH_3)_3Pt(CpCH_3)$ FEBID-FIBID comparison reports that FIBID depositions can see metal purity increases greater than 10% simply by choosing FIBID over FEBID.[53] Additionally, FIBID depositions can report improved resistivity values at room temperature over FEBID, but cryogenic conditions show the opposite effect.[54]

FEBID/FIBID is most commonly used in lithographic mask repair and transmission electron microscopy (TEM) sample preparation, but functionalized devices have also been demonstrated, for example as nanomechanical resonating sensors[55,56], advanced scanning probe tips[57], chiral plasmonics[58], plasmonic split ring resonators[33], and magnetic architectures[59].

Much progress has been made in creating high purity nanostructures, where gold, silver, and other metals at a nanoscale size show strong plasmonic interactions between the free electrons in the metal and the incident light. Plasmonic behavior can be described accurately from a classical viewpoint, and the size, shape and dielectric environments of plasmonic nanoparticles are the dominating factors in the plasmonic response[28]. Plasmon behavior has two major varieties, bulk surface plasmon polaritons (SPP) and localized surface plasmon resonances (LSPR) in nanomaterials; Figure 9 schematically illustrates the difference between these behaviors, showing the larger-scale bulk phenomena vs the localized nanostructure response.

Both of these plasmonic responses have been used for hundreds of years without understanding the physical phenomena, for example gold nanoparticles are suspended in stained glass windows to realize different colors, but the modern world has seen great strides in targeted plasmonic functionalization in nano-optic sensing and waveguides[61], chemical and biological sensing[62], raman scattering enhancement[63], meta-atoms[64], single-molecule coupling[65], photosynthetic devices[66], and optical photodetection[67]. Currently, plasmonic circuits and photonic interfaces are rapidly progressing fields[68] with innovative ideas emerging as candidates for next-generation computer chips[69–71].

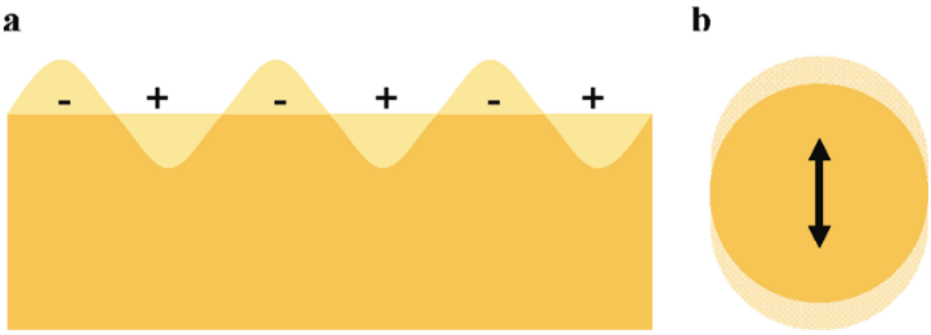

Figure 9. (a) A surface plasmon polariton (SPP), (b) a localized surface plasmon resonance (LSPR). Reprinted (adapted) with permission from Mayer, K. M.; Hafner, J. H. Localized Surface Plasmon Resonance Sensors. *Chem. Rev.* **2011**, *111* (6), 3828–3857. https://doi.org/10.1021/cr100313v.[60] Copyright 2011 American Chemical Society.

Dimethyl gold aceytlacetate is a well-known FEBID precursor for the deposition of gold containing nanostructures, but as-deposited FEBID has a weak plasmonic signal due to the high (60-90%+) carbon content[72]. With sufficiently high purity gold deposits, a wealth of plasmonic research can be enabled by new directed nanoscale deposition techniques. Currently, purification techniques of FEBID Au structures successfully raise the Au purity above 50% but can lead to deformation as shown in Figure 10. Split-ring resonators have been synthesized using multi-step fabrication methods, where FEBID deposits are functionalized by sputtered gold.[33]

FEBID/FIBID structures have also been functionalized magnetically, and nanomagnetics is a subject of intense research with implications for high-density storage and sensing. FEBID/FIBID is uniquely tailored for the creation of 3D magnetic nanodevices[73], and magnetic scanning probe microscopy tips from the $Co_2(CO)_8$ precursor were shown to be able to achieve an imaging resolution of 40nm[74] by Utke *et. al.* in 2002, and 10nm resolution was achieved by Belova *et. al.* in 2012[75]. Belova indicated that their spatial resolution was limited by their material purity and tip sharpness, and their best imaging tip was reported as 60% Co with a 20 nm tip diameter. As a result of the highly-customizable magnetism complex FEBID structures offer, many magnetic precursors have been investigated for a variety of applications – $Ni(PF_3)_4$[76], $Ni(C_5H_4CH_3)_2$[76,77], $HFeCo_3(CO)_{12}$[78], $Fe_2(CO)_9$[28,79–81], $Fe(C_5H_5)_2$[82–84], $Fe_3(CO)_{12}$[85], $Fe(CO)_5$[24–26,82,86–112], $Co(CO)_3NO$[22,113–119], and the highly-used $Co_2(CO)_8$[22,27,29–31]. Figure 11 shows FEBID enhanced tips on commercial MFM tips.

While there are different fabrication methods for the creation of 3D nanostructures, FEBID/FIBID stands out from the others due to accessibility, flexibility, and broad community utilizing functional direct-write 3D devices for research and industry. This nanofabrication

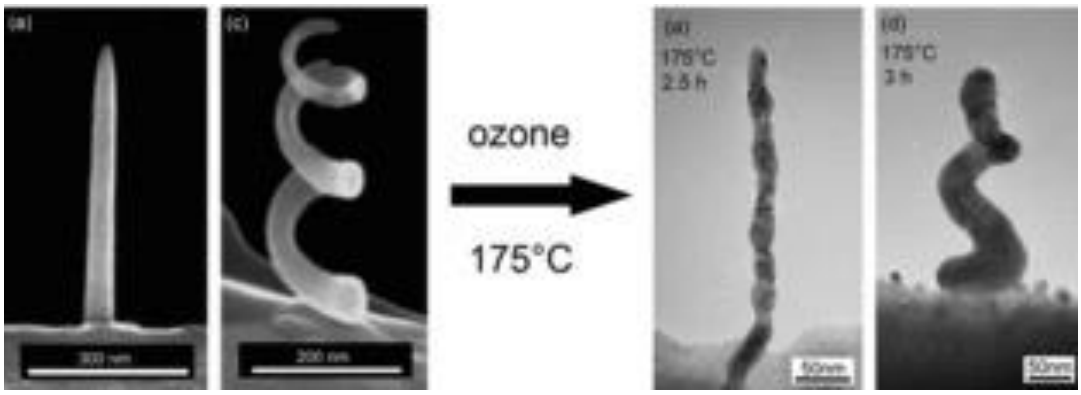

Figure 10. (a,b) As deposited FEBID structures from Au(acac) and (c,d) purified structures with different structural morphologies. Figure from Höflich, K.; Yang, R. B.; Berger, A.; Leuchs, G.; Christiansen, S. The Direct Writing of Plasmonic Gold Nanostructures by Electron-Beam-Induced Deposition. *Adv. Mater.* **2011**, *23* (22–23), 2657–2661. https://doi.org/10.1002/adma.201004114[72]. © 2011 WILEY-VCH Verlag GmbH & Co. KGaA, Weinheim.

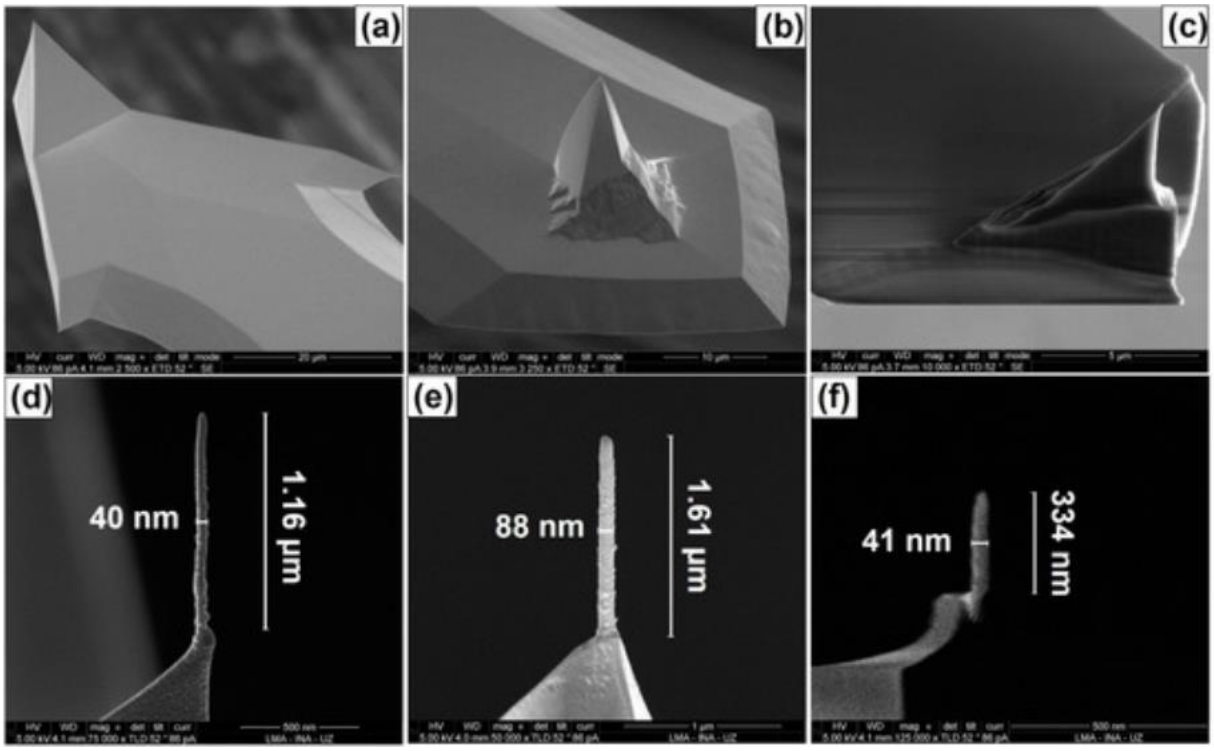

Figure 11. (a-c) Commercial MFM tips, (d,f) Fe and (e) Co FEBID supertips placed on top of the commercial tips. Figure reproduced from Navarro, *et. al.*[120]. Reprinted under a Creative Commons Attribution (CC BY) license (https://creativecommons.org/licenses/by/4.0/), with no changes made.

method is therefore a priority for new investigations of functional material coatings to enable further functionalization and new device technologies.

CHAPTER I

Selected Area Deposition of PtC_x Nanostructures: Implications for Functional Coatings of 3D Nanoarchitectures

John Lasseter,[1,2], Philip D. Rack[1], Steven J. Randolph[2,]*

1. Department of Materials Science and Engineering, University of Tennessee, Knoxville, Tennessee 37996, United States

2. Center for Nanophase Materials Sciences, Oak Ridge National Laboratory, Oak Ridge, Tennessee 37830, United States

[*]Corresponding author email: randolphsj@ornl.gov

Author Contributions

Reprinted with permission from ACS Appl. Nano Mater. 2022, 5, 8, 10890–10899. Copyright 2022 American Chemical Society[121]. John Lasseter performed the depositions, imaging, computer vision processing, and energy dispersive x-ray spectroscopy (EDX/EDS) and led the finite-element modeling. Finite-element modeling was assisted by Steven Randolph. John Lasseter wrote the first draft and Steven Randolph and Philip D. Rack edited the manuscript. Philip D. Rack and Steven Randolph conceptualized the experimental plan.

Abstract

We report that selected area deposition of 3D nanostructures is induced via a pyrolytic laser chemical vapor deposition (CVD) process where the selected area heating results from the unique photothermal transport regime that is intrinsic to 3D nanostructure. PtC_x composite nanostructures were deposited by focused electron beam induced deposition (FEBID) and used as the 3D

templates. Subsequent simultaneous localized delivery of an organometallic PtC_x precursor and pulsed 915 nm laser irradiation to the pre-defined nanostructures results in selected area deposition on the FEBID features. Results indicate the ability to initiate the process on sub-diffraction-limit nanoscale features. To elucidate the mechanisms that are operative in the selected area deposition, we analyze the effects of laser repetition rate, power, and pulse duration. Thermal simulations corroborate that the pseudo-1D thermal transport of the nanostructure geometry coupled with the optical and thermal properties of the nanostructure govern the CVD reaction. The results demonstrated here suggest that controlling the thermal transport in nanomaterial architectures could be a useful means to spatially control localized photothermally stimulated chemical reactions and induce selected area reaction.

Introduction

Additive manufacturing and direct write processes have experienced significant growth in the past decade where new materials, techniques, and applications have all emerged. Various size scales have been explored historically but recent pushes have extended three dimensional additive manufacturing towards the micro and nanoscale[122,123]. While several techniques like direct-ink writing[124,125], multi-photon lithography[126,127], electrohydrodynamic printing[128], dip-pen lithography[129], laser induced[130–133] and other methods[134] in principle work in the sub-micron regime, focused electron and ion beam induced deposition (FEBID/FIBID) is likely the most developed technique for synthesizing complex architectures in three dimensions. Several applications have been demonstrated including nanomechanical resonating sensors[55,56], advanced scanning probe tips[57], chiral plasmonics[58], plasmonic split ring resonators[33], and magnetic architectures[59].

In FEBID a focused electron beam is used to decompose precursor molecules that adsorb onto the substrate resulting in the condensation of by-products and the formation of a nanoscale deposit. While accurate control through detailed modeling, simulations[6,9–13] and 3D computer aided design infrastructure[14–16] have all been realized for FEBID, challenges remain in this technique. Likely the biggest obstacle for wider scale adoption is the resultant, material quality due to residual carbon incorporation from organometallic precursor fragments[34]. Various precursors have been explored which result in different functionality and purity (see Barth *et al.*[18] for a review of precursors). Trimethyl(methylcyclopentadienyl)platinum ($MeCpPtMe_3$) is the most common precursor and depending on the dose, beam energy, and residual water in the chamber the resultant PtC_x deposit varies from $\sim 5<x<8$[135]. Various metal carbonyls have been explored and the optimum metal content varies: $Cr(CO)_6$ – 20-40 at.% [18], $Mo(CO)_6$ – 8-20 at.% [19,20], $W(CO)_6$ – 37-58at.% [21–23], $Fe(CO)_5$ – 80-95 at.% [24–26], $Fe_2(CO)_9$ – 80-93at.% [27,136], $Co_2(CO)_8$ – 73-100at.% [22,27,29–31] and $Ni(CO)_4$ – 95at.%[32]. Additionally, several groups have explored subsequent coating processes[33], post-electron beam induced curing[34–39], co-deposition with purification gases[40,41], beam-induced post-purification with oxidizing[42–46] and reducing[47] precursors, post-deposition annealing[34,43,48–50], and synchronized pulsed laser FEBID[51,52] all aimed at improving material properties without sacrificing the nanoscale 3D direct-write attributes that make the process attractive.

Thus, while FEBID/FIBID are excellent for nanoscale dimensional control, the poor materials quality makes subsequent deposition techniques an important area to study. It is well known the spatial confinement in FEBID nanostructures can result in pseudo 1D heat transport, which results in nanostructure heating that alters the precursor adsorption and decomposition

kinetics/thermodynamics[137–140]. PtC_x nanostructures grown via FEBID are used as templates for subsequent selected area laser deposition. For convenience we use the same precursor (trimethyl (methylcyclopentadienyl) platinum ($MeCpPtMe_3$)) as both the FEBID precursor as well as the precursor for the subsequent selected area laser deposition. As we will show, while the ~ 100 μm diameter focused laser spot irradiates both the underlying substrate and the FEBID nanostructures, the combined optical and thermal properties of the nanoscale FEBID architectures induce selected area photothermal nanostructure heating that may exceed the thermal decomposition threshold of precursor molecules while the underlying substrate is well below the threshold. While we employ FEBID-synthesized architectures for the selected area photothermal chemical vapor deposition (CVD), the strong geometric contribution to thermal transport at the nanoscale implies applicability to other 3D nanofabrication techniques described above. Generally, the phenomenon should be compatible with any nanostructure of proper optical, thermal, and geometric characteristics. Because FEBID deposits using most organometallic precursors result in high carbon content, they have limited as-deposited functionality; thus, the laser CVD process can be used to subsequently selectively coat the 3d architectures with materials containing the desired functionality. Future plans include magnetic coatings with $Co_2(CO)_8$) precursor, and plasmonic coatings derived from dimethyl gold acetylacetonate.

Results and Discussion

Our initial experiments were designed to assess the feasibility of photothermally driving a CVD process that selectively deposits on FEBID 3D nanostructures. Figure 12a illustrates schematically the process where initially a series of nanopillars were grown to various heights via the standard FEBID process using the $MeCpPtMe_3$ precursor, which nominally produces deposits

of PtC_x where $5 < x < 10$. Figure 12b illustrates that when the pseudo 1D nanopillars are subsequently exposed to focused, pulsed laser irradiation simultaneously with $MeCpPt^{IV}Me_3$ precursor – the pulsed laser photothermally heats the FEBID nanopillars and induces thermal decomposition of the precursor. Since the photothermal CVD is driven largely by the characteristic photothermal response of the nanostructure, the deposition can be accomplished on a variety of substrates with only small changes in the growth (see Supporting information S1). Thermal modeling shows significant shifts in the substrate thermal conductivity only modestly shifts the peak temperature.

While other coating approaches are useful in "blanket" covering the 3D structures and substrates simultaneously, the laser induced photothermal CVD enables area selectivity and a unique regime where deposition occurs only on the FEBID nanostructures as dictated by their thermal transport and material properties. It should be noted that we utilized $MeCpPtMe_3$ *in-situ* both for FEBID and CVD as a matter of convenience to demonstrate the more generalized phenomenon. Again, it is anticipated that nanostructures grown via other techniques can also be selectively deposited and the laser CVD process should be ubiquitous to other precursors that do not photolytically decompose, so different materials/functionalities can be achieved with judicious choice of the 3D template and CVD precursors. To test our hypothesis that the selected area deposition is governed by the thermal resistance of the nanostructure a series of FEBID nanopillars with various heights and similar diameters were deposited. The photothermal CVD process was documented via sequential SEM secondary electron (SE) imaging resulting in videos (Supporting video V1) that were analyzed frame-by-frame with a semi-automated, computer vision algorithm

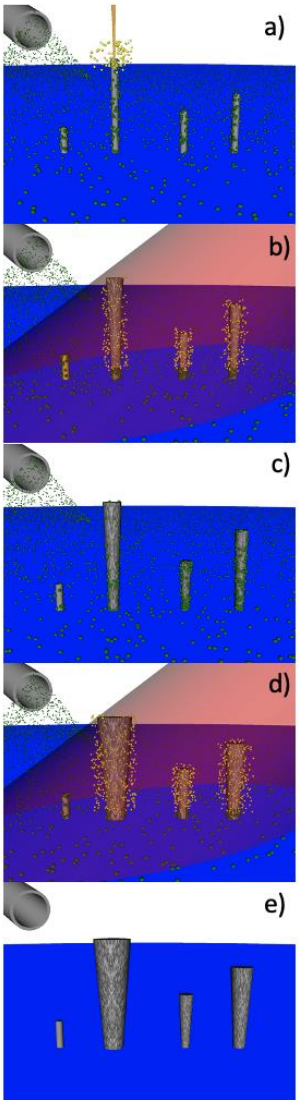

Figure 12. Schematic images of localized photothermal deposition of nanostructures. a) As-deposited PtC_x nanostructures formed by focused electron beam induced deposition from $MeCpPtMe_3$ (green spheres) forming C_yH_z by-products (yellow spheres) and a condensed nanopillar deposit (grey). In a general sense, FEBID follows the scheme $C_5H_4CH_3Pt(CH_3)_3$ (*g*) + *e*- ⟶ PtC_x(*s*) + C_yH_z (*g*). Subsequent pulsed laser selected area deposition illustrating various times during the growth during the b) and d) laser-on and the c) and e) laser-off time. During the laser-on, the pulsed laser selectively heats the deposited nanostructure and raises the nanostructure above the decomposition threshold of the precursor molecules and thus decomposes the molecules into a condensed deposit and C_yH_z by-products. This reaction can be approximated by the scheme $C_5H_4CH_3Pt(CH_3)_3$ (*g*) + *hn* ⟶ PtC_x(*s*) + C_yH_z (*g*) where laser-induce PtC_x deposits selectively on the FEBID. During the laser-off time, the pillars are below the decomposition temperature and thus precursors adsorb and desorb on the deposit until the next laser pulse.

(Supporting information S2). To confirm the nanostructure evolution is not dominated by the electron beam exposure that occurs during imaging, exposures with and without video capture were taken and minimal difference was observed in these experiments. Additionally, deposition was attempted with and without the precursor gas flow to confirm the adventitious adsorbed carbon was not the precursor source and minimal changes were observed without platinum precursor flow.

To correlate the selected area deposition to nanostructure temperature, the measurements from the computer vision analysis of the evolving features were used as input to a COMSOL heat flow model derived from the absorbed laser energy and the nanostructure properties. The power input to the nanostructure for the simulation is estimated from fractional laser energy absorbed in the nanopillar $Q_{abs}=P_o \times (1-R) \times (1-e^{-A2r}) \times \frac{2rl}{\pi r_{laser}^2}$) where P_o is the total laser power, R is the reflectance $[(1-n_{PtCx})^2+k_{PtCx}^2]/[(1+ n_{PtCx})^2+ k_{PtCx}^2]$, A is the linear absorption or attenuation coefficient ($4\pi\ kPtC_x/\lambda$), l is the nanopillar length, r is the nanopillar radius, r_{laser} is the laser spot radius and λ is the laser wavelength. The optical constants n_{PtCx} and k_{PtCx} are the refractive index and extinction coefficient of the nanopillar template and were taken from previous literature to be 1.87 and 0.31, respectively, which was approximated by the Maxwell-Garnett effective medium approximation for PtC_5[141] and the heat capacity, and density were previously reported to be, 1250 kg/m^3, and 700 J/(kg-K), respectively[142]. The geometry of the nanopillar was simplified and assumed to be a cylindrical shape using an effective radius. To determine the effective radius, we used our computer vision algorithm to measure the pillar radius every pixel, which for our typical image is on the order of 4 nm along the nanopillar length. We subsequently average the measured radii but exclude the top and bottom 20% of the as-growing structure. The thermal conductivity of the nanopillar was estimated to be 8.0 W/(m-K). It is important to note that the thermal

conductivity was used as a tuning parameter to calibrate our simulations to the experimental observations. By simulating the pillar geometry and laser conditions at which the onset of laser CVD is observed we varied the thermal conductivity of the pillar material until our simulated peak nanopillar temperatures were approximately equal to the reported thermal decomposition temperature of the precursor (~ 600 K)[143]. The underlying assumption here is that the onset of laser CVD in our experiments occurs when the peak nanopillar temperature reaches this decomposition temperature, which ignores any potential catalytic effects of the nanostructure. Conveniently, the thermal conductivity of the nanopillar indicated by our tuning simulations is consistent with previous literature reports[144]. See Supporting information S3 for full sensitivity analysis of the thermal simulations.

The calculated absorbed power is then evenly distributed in the nanopillar volume which acts as the source term for the thermal model. COMSOL then discretizes or meshes the nanopillar and substrate and solves the heat transfer in the solid via finite element using the following equation, $\rho C_p \frac{\delta T}{\delta t} + \nabla q_{cond} = Q_{abs}$ where q_{cond} is the heat flux by conduction (note we ignore radiation). The substrate is chosen to be deliberately large enough that we can set radial and lower z-dimensional constant temperature boundary conditions of 293 K without impacting peak temperatures at the nanopillar tip (see Supporting information S4). This results in temporal and spatial temperature information in the nanopillars. As will be shown the peak temperature is located at the top of the nanopillar. Furthermore, the laser heating occurs rapidly on the order of 1-2 μs and then saturates. While the specific time of this saturation depends on the nanopillar geometry and properties, when we report the peak temperature, it is the temperature at the end of the pulse width and the top of the nanopillar.

In the plots that follow, the following procedure is used to generate the color-coded data which represents the modeled temperature. Scanning electron "videos" are collected in situ during the growth and at specific time increments the nanopillar length and effective radius are measured. Using the cylindrical approximation and the experimental laser parameters, the absorbed power is determined, and the cylinder is automatically constructed in COMSOL. The time dependent absorbed laser energy (integrated for power) is applied evenly to the cylinder and the full temporal and spatial temperature dependence of the nanopillar and substrate is determined. The peak temperature is determined for each time stamp and plotted as the heat map of the data. It is important to note that the modeling is semiquantitative and is intended to be illustrative. We interrogate several geometries (pillar height/diameters), and laser parameters such as power, pulse width, and frequencies. While some of the experiments show growth and modeled temperatures slightly below the threshold values and some exhibit growth initiation above the threshold values, we believe the preponderance of the data all point to a thermally driven CVD process as described in detail below.

During the experiment, the incident laser power was incrementally increased as indicated in Figure 13a until selected area deposition was evident on all nanopillars. The laser pulse duration (10 μs) and repetition rate (1000 Hz) were held constant for these experiments to probe the how power and geometry affected the growth.

Figure 13b-e are SEM image captures at various times (see Supporting video V1 for the full experiment). To visualize the impact of the thermal resistance, the data points are colored coded with the simulated temperature where the evolving simulated temperature is based on the geometric data extracted via the computer vision algorithm, subsampling every 5 frames (see

Supporting information S2 for details). The overarching trends illustrate that consistent with the higher thermal resistance ($l/K\pi r^2$), where K is the thermal conductivity, the taller nanopillars initiate photothermal CVD at lower laser power, whereas shorter nanopillars require higher power. Notably, all the nanopillars turn-on at similar simulated temperatures. The dark blue data points are zero laser power time intervals where the laser power was manually changed.

For long deposition durations, the experimental structures develop complex geometries. For instance, the large thermal mass of the substrate results in a low temperature boundary condition, which inhibits photothermal CVD near the base of the nanopillars. As a result, the nanostructures evolve from a cylinder to a more inverted conical shape as opposed to a conformal and isotropic cylinder. While we model the temperature during growth using a simplified cylindrical geometry, we acknowledge this deviation as a source of underestimating of the nanopillar temperature.

Specifically, the low to zero growth at the pillar base will add a high series thermal resistance. Our initial expectations were that as the nanopillars widened, the thermal resistance would decrease, the thermal mass would increase, and thus the nanopillar temperature would fall and yield lower photothermal CVD rates. However, simulations predict that some final structures are hotter than the initial as absorbance and the thermal series resistance at the base is operative. The expanding nanopillar suggests again that we are underestimating the nanostructure temperature due to the persistence of the thermal restriction at the base. Indeed, we observe experimentally that the long-exposure structures see phase-separation and what appears to be a flowing, molten phase (See Supporting video V2). Figure 13f) shows 3D rendered heat maps of our cylindrical

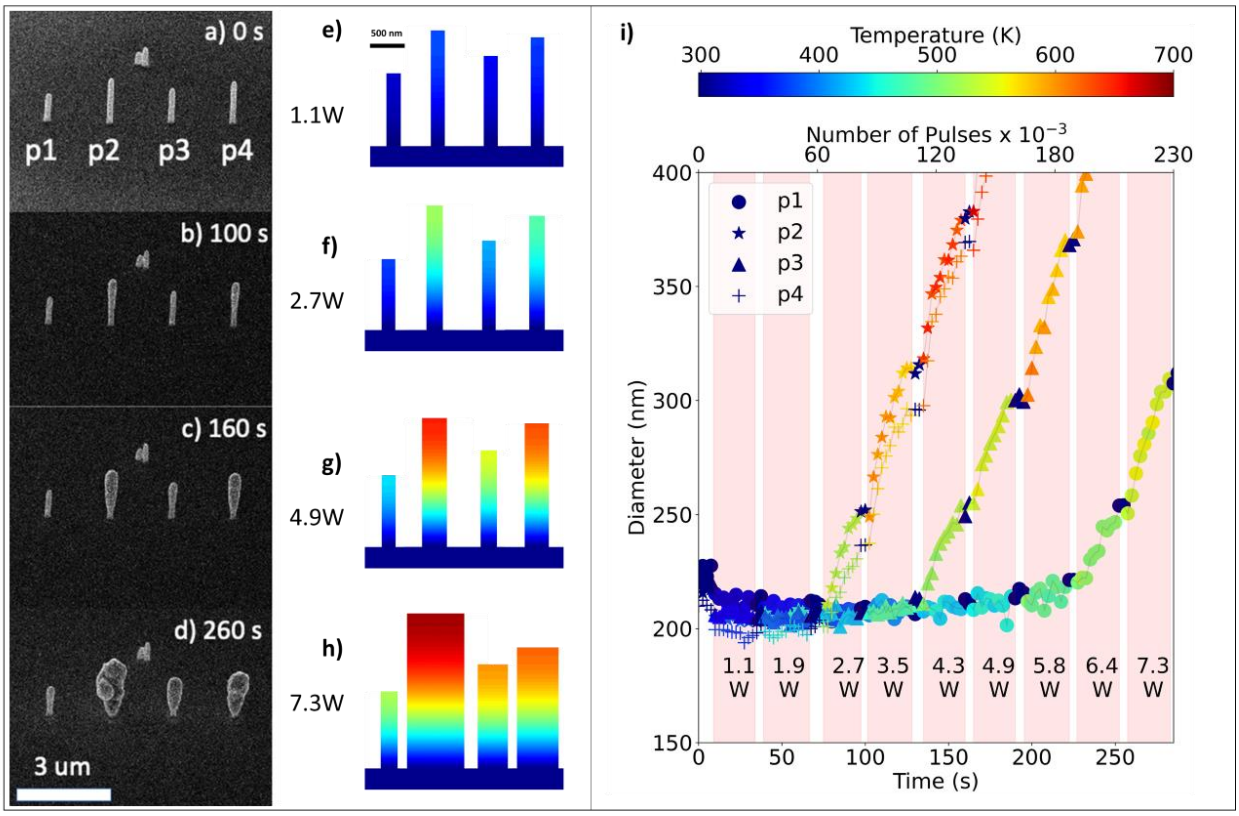

Figure 13. a) SEM images of as-deposited FEBID nanopillars of similar width grown to different heights and b)-d) selected area laser growth at various time stamps (the scale bar in d) applies to all SEM images). The laser growth conditions are 10 μs, 1000 Hz (0.01 duty cycle) where the laser power varies with time and can be inferred from the radius diameter versus time plot of the experiments shown in i). e-h) Corresponding maps of the modeled temperature of the 4 nanopillars at the end of a 10 μs laser pulse at the laser power listed in each panel. The modeled pillar geometry is constructed using cylindrical geometry approximations made from the neighboring SEM image. (note that the scale bar in e) applies to all of the modeled pillars in e-h)). i) Plot of nanopillar diameter as a function of total time (bottom axis) and laser pulse number (top axis). The laser power was systematically increased during the experiment where the highlighted regions list the applied laser power listed. The corresponding data point is color-coded with temperature based on a COMSOL simulation of the geometry approximated from the captured SEM image at that time stamp.

approximation of the experimental geometries as extracted from the SEM image datasets in Figure 13d at the experimental optical power of 4.9 W. These simulations offer further insights into nanostructure evolution. Note the shortest nanopillar has the lowest temperature and is below the decomposition temperature and thus is not growing consistent with Figure 13a. The third nanopillar has experienced growth and the simulated temperature is comparable to the decomposition temperature. The second and fourth nanopillars are the hottest and have similar temperatures and have the steepest slopes consistent with higher growth rates. The top is hotter due to the quasi-1D heat transport confinement that occurs on the nanoscale. The tip stays above the decomposition temperature longer, thus deposition is preferred there. Inset next to each 3D nanopillar are time-temperature plots of the tip of the nanopillars. As demonstrated, the rise and fall time are on the order of 1 μs so the temperatures all saturate at the peak temperatures during each 10 μs pulses. More discussion on the validity of the thermal model and the time constant will be discussed below in the pulse width study.

To further explore the effect of geometry on the thermal resistance and initiation of the selected area deposition, several nanopillars of similar height were deposited with variable diameters. Figure 14a illustrates the pillar diameter versus time (and number of pulses delivered) for the various nanopillar widths and Figure 14b-c are the as-FEBID grown and post laser exposure SEM images, respectively. The laser power was again incrementally increased over time to note the onset of photothermal CVD. As is observed, the various diameters all initiate at the same laser power however, the nanopillars have slightly different simulated temperatures, where the smaller diameters are slightly higher than the larger diameters. Consistent with the higher temperatures, the diameter growth rates are higher for the narrower nanopillars. The fact that the growths all

turn-on at the same power, does emphasize the point that while the thermal resistance increases with smaller diameter, the absorbed power below the absorption depth also decreases so the optical properties are also critical to the characteristic growth. From the narrowest pillar in Figure 14, we estimate a per laser pulse diameter growth rate of ~ 8 pm/per pulse. See Table 1 for summary of conditions and growth rates for experiments in Figure 14 and Figure 15. Two possibilities for the selected area deposition mechanism are decomposition of precursor gas that is adsorbed during the laser-off time or decomposition of precursor gas molecules that arrive while the nanostructure is above a threshold decomposition temperature. To rationalize the deposition rate and test the proposed mechanisms, a series of photothermal CVD depositions were performed with constant laser pulse width (10 μs), on fixed geometry nanopillars and variable pulse repetition rate (250-5000 Hz). In this case, the lower repetition rate data has a longer inter-pulse delay time (ranging from 4000 to 250 μs, respectively). Figure 15 is the nanopillar diameter versus a) real time, b) number of pulses, and c) total laser on time (duty cycle x processing time). As illustrated, the rates (slopes) of the diameter versus pulse number is constant, which suggests that the deposition rate is constant. While at high repetition rate, the FEBID contribution during imaging is minimal, at lower frequency the laser duty cycle is sufficiently small that FEBID during imaging is non-negligible and affects the growth. Thus, there is some nanopillar broadening, which interestingly shortens the incubation number of pulses to initiate the growth. This again could be indicative of an absorption dominated initiation where the increasing nanopillar cross-sectional area increases the optical power absorption faster than the decrease in thermal resistance. Regardless of the incubation time, the near constant growth rate over the 20x change in frequency suggests the growth is dominated by the flux of $MeCpPtMe_3$ molecules that arrive at the nanostructure above

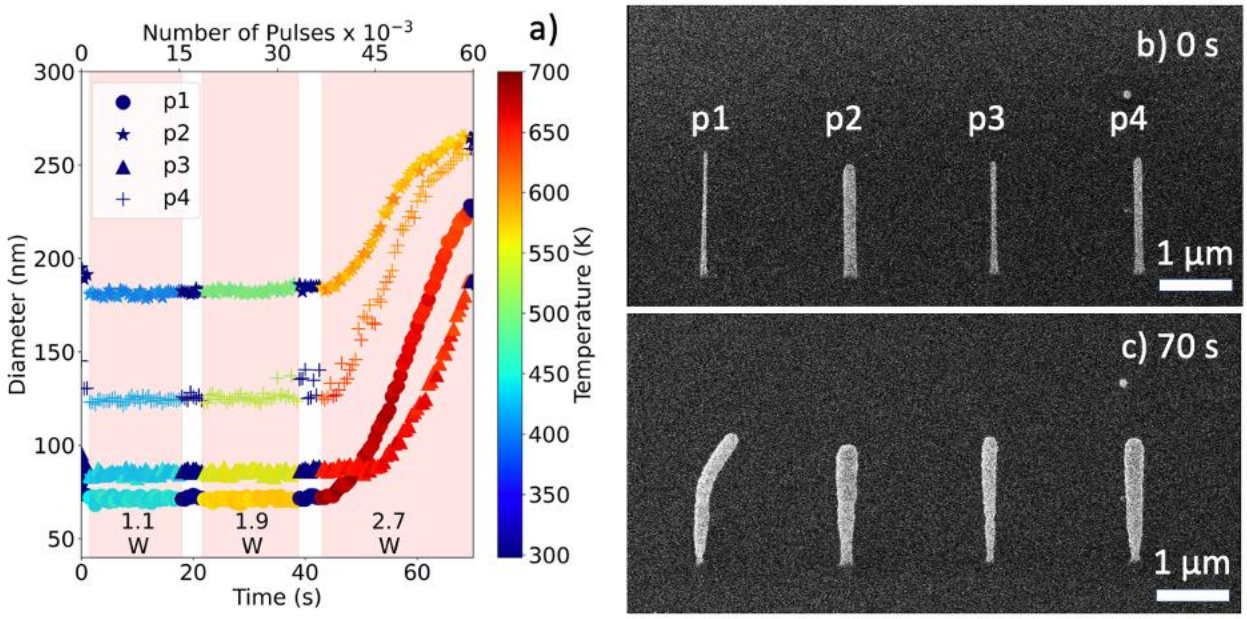

Figure 14. Plot of the a) nanopillar diameter as a function of time and number of laser pulses for nanopillars of similar initial height but variable initial diameter. SEM images of b) the as FEBID deposited and c) after selected area deposition.

Table 1. Summary of diameter growth rates at various experimental parameters.

Figure	Label	Laser Rate (Hz)	Pulse Width (μs)	Laser Power (W)	Deposition Rate (nm/s)	Deposition Rate (pm/pulse)
Figure 14	p3	1000	10	2.7	5.08	5.08
Figure 14	p2	1000	10	2.7	5.38	5.38
Figure 14	p4	1000	10	2.7	7.41	7.41
Figure 14	p1	1000	10	2.7	7.97	7.97
Figure 15 (a-c)	250 Hz	250	10	4.9	0.73	2.92
Figure 15 (a-c)	500 Hz	500	10	4.9	1.77	3.54
Figure 15 (a-c)	1000 Hz	1000	10	4.9	4.65	4.65
Figure 15 (a-c)	5000 Hz	5000	10	4.9	9.10	1.82
Figure 15 (d-f)	3 μs	1000	3	4.9	0.47	0.47
Figure 15 (d-f)	5 μs	1000	5	4.9	0.87	0.87
Figure 15 (d-f)	20 μs	1000	20	4.9	2.09	2.09
Figure 15 (d-f)	50 μs	1000	50	4.9	2.16	2.16

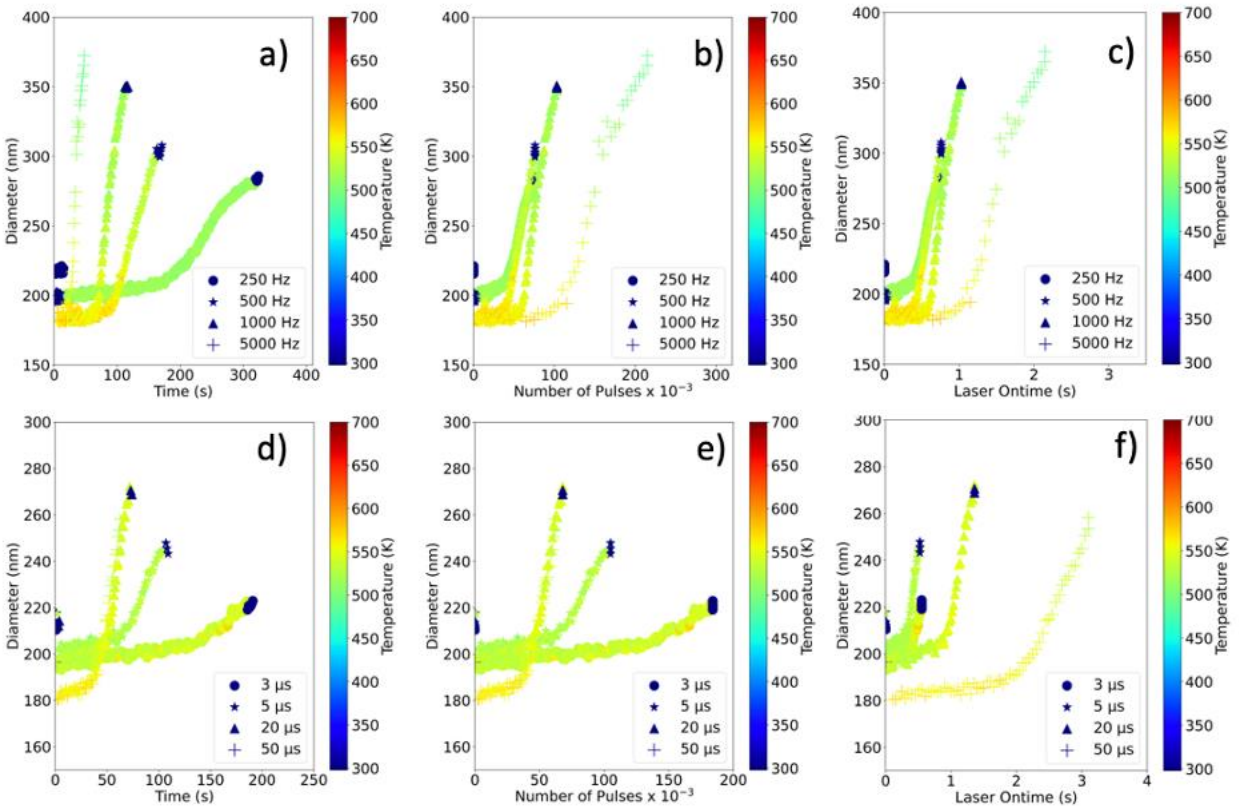

Figure 15. Plots of the diameter growth rate as a as a function of a) time, b) pulses and c) total laser on time processed at with various laser frequencies (noted in the figure legends). Plots of the diameter growth rate as a function of d) time and e) pulses and f) total laser on time processed at with various laser pulse widths (noted in the figure legend).

a critical decomposition temperature. Based on our previous estimate of the $MeCpPt^{IV}Me_3$ flux in our system ($1.8x10^3$ molecules/(nm^2-s)), we calculate a diameter per pulse (10 μs) growth rate of ~6 pm/pulse, which is in good agreement with the measured values. Deviations in the gas flux, and the thermal rise/decay time could both contribute to the differences in our model and experimentally observed per-pulse growth rates.

Finally, we investigate the effect that pulse width (3-50 μs) has on the growth rate, where we keep frequency (1000 Hz) and fixed nanopillar geometry constant. Figure 15 is the nanopillar diameter versus d) processing time, e) number of pulses, and f) total laser on-time (duty cycle x processing time). As shown in Supporting information S5, is important to note that at 10 μs pulse duration we are well within a steady-state thermal regime. Because the rise and fall time of the laser heating is on the order of 2 μs, thus the temperatures all saturate in this time scale.

We expect the nanostructure does not reach the precursor decomposition temperature with a pulse duration below ~2 μs, which has been confirmed experimentally (see 1 μs data in Supporting information S6). Thus, the laser exposure time is proportional to the pulse width and thus as illustrated in Figure 15e the per pulse growth rate is roughly proportional to the pulse width, except that the 20 and 50 μs data are similar. Figure 15f normalizes the data to total laser on-time. Interestingly, the initial incubation laser on-time to start growth is proportional to the effective initial diameter which scales with the pulse width. This diameter-dependence may again be indicating the importance of the optical absorption term in this length scale as larger initial cross-sectional areas decrease this incubation time. We speculate one cause could be a reordering of the nanostructure that is governed by the initial stages of laser irradiation where the as-FEBID deposited nanopillars densify proportional to the laser pulse width, and thus have slower initial

growth. In future work, we will study in more detail the effects that the initial densification has on the growth process, including the density, optical, and thermal properties. Suffice it to say that there are subtle feedback processes involved in the early stages of the laser irradiation that affects the subsequent growth.

Summarily, the selected area laser CVD process is controlled by several variables. First of all, we show that the growth is consistent with a photothermal CVD process in which the high temperatures are selectively achieved on the nanostructures relative to the substrate because of the combined optical and thermal properties of the nanoscale geometries. Because the growth only occurs when the structures exceed the threshold for the precursor dissociation, and because we are implementing a pulsed laser source, the laser power and duty cycle of the laser (pulse width and frequency) affects the growth rate normalized by the processing time. Finally, consistent with most thermal CVD processes, the growth rate is also dependent on the precursor flux. In our experiments constant precursor flux is maintained by: 1) consistent positioning of the processing region relative to the gas injection system; 2) constant precursor temperature; and 3) monitoring a constant chamber pressure.

To elucidate the elemental distribution of the laser deposited structures, high-resolution EDS is presented in Figure 16b. It can be seen by the EDS map that the bright crystallites in the SEM are platinum-rich and point spectra in these regions confirm the higher platinum concentration. However as seen in the cross-section of Figure 16d, the platinum nanoparticles seem to migrate towards the surface, so the carbon-rich interior makes it difficult to determine the exact purity, due to the extended penetration of the electron beam. The phase separation and larger crystallites are not unexpected. Because of the limited solubility of Pt and C, the typical FEBID-

grown material is a nanogranular composite of Pt grains in an amorphous carbon matrix. As several have observed, annealing or higher temperature growth of PtC_x deposits, results in coarsening of the Pt grains. Similar observations have been made in FeCO deposits[145] from the $Fe_2(CO)_9$ precursor, where initially homogeneous amorphous FeCO nanowire deposits were grown, in situ STEM characterization revealed phase separation and coarsening of Fe grains along the nanopillar axis. As discussed above, the $Co_2(CO)_8$ precursor results in much higher purity as-deposited FEBID Co nanowires up to ~ 70%[146]. They also showed that annealing these structures in vacuum up to 600ºC result in a purity on the order of 95% with a concomitant narrowing of the nanowire. The improved crystallinity and purity results in superior magnetic properties.

In Figure 17a, we demonstrate the ability to uniformly and selectively deposit on an array of simple FEBID structures in parallel with reasonable fidelity despite somewhat inhomogeneous laser irradiance in the field of view of the image (~ 20x20 μm). Additionally, Figure 17c demonstrates a functionalized head-to-head 3D split ring resonator[33]; while Pt is not plasmonically active, selectively functionalizing these structures with gold using for instance the common FEBID gold acetylacetonate precursor could lead to plasmonically active 3D structures[33]. Future work will explore new precursors to realize magnetic ($Co_2(CO)_8$)[147], and plasmonic (Au precursors), as well as co-reactants such as oxygen and water to reduce the carbon content in the functional coatings.

Experimental/Methods

All experiments were conducted in a dual beam FIB/SEM (FEI Nova 600) equipped with gas injection system (GIS) hardware for deposition of platinum and an in-situ pulsed laser

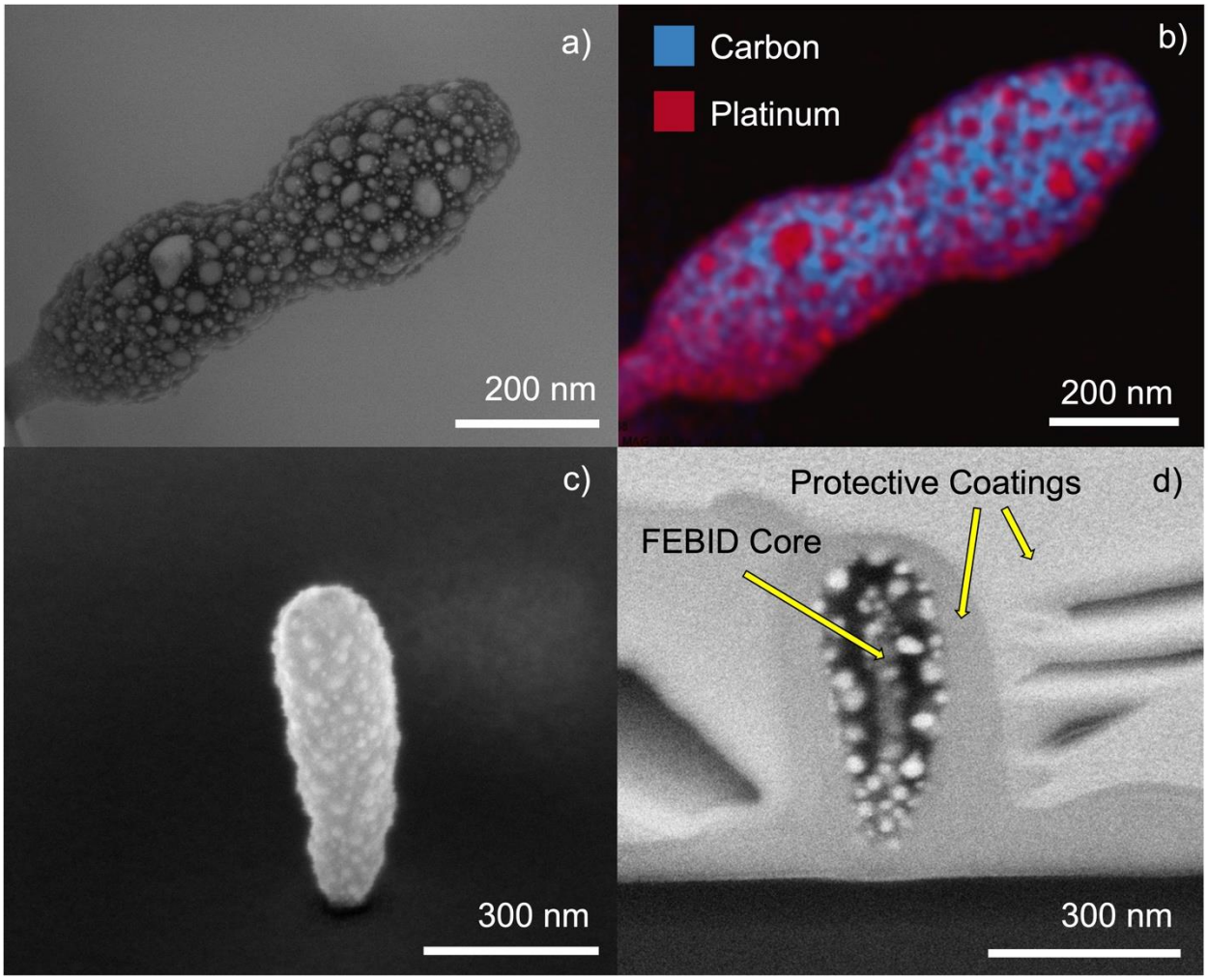

Figure 16. a) SEM image and b) EDS map of a nanopillar after selected area laser processing. EDS maps of the pillar showing platinum-rich regions embedded in a C matrix indicating phase separation and Pt grain growth during the laser processing. c) SEM image of an as laser grown pillar and the associated backscatter SEM image of a FIB cross-section showing the phase separation where Pt are the bright regions. The light, top amorphous material is a focused ion beam induced deposition protective layer for cross-sectioning, and the darker amorphous layer under that is initial FEBID protective deposition. The EBID as-deposited nanostructures were grown using a single pixel dwell at 5kV, 98 pA. 75nm beam diameter by defocusing, for 40s (a,b) and 30s (c,d) Laser CVD was accomplished using 4.8W, 10 μs 915 nm pulses at 1kHz for 60 s.

system (Waviks Vesta) focused coincident to the electron beam at the eucentric position of the system.

The laser source consists of 3 fiber-coupled laser diodes with wavelengths (915 nm, 785 nm, and 405 nm) delivering focused, unpolarized light with variable pulse duration (10 ns to continuous wave) with repetition rates ranging up to several MHz. Note the 20 W 915 nm laser is coupled to a multimode fiber with a ~ 100 μm diameter and the several hundred mW 785 nm and 405 nm laser diodes are coupled to a 5 μm diameter single mode fiber. All the experiments here used the 915 nm multimode fiber system. Positioning of GIS and the laser source on opposing sides of the chamber allows for simultaneous insertion of the laser source and GIS needle with both directed coincidentally to the eucentric position. This configuration is well suited for the required experiments due to the ability to tilt the stage between FEBID and laser CVD positions without losing focus/positioning of the SEM, laser, or GIS.

While we have demonstrated that this process is nearly substrate-independent, all systematic data presented here was performed on a silicon substrate. All work presented here was carried out using a 5 keV and 98 pA for FEBID growth and in situ imaging. The nanopillar height is controlled by adjusting the beam current density and exposure time. The nanopillar diameter can be intentionally increased by applying a defocus to increase the beam diameter (which also reduces the current density) for a single pixel dwell or by patterning multiple pixels in an area scan. The GIS is inserted while the stage is at 0^{o} tilt at the eucentric height, the GIS valve is opened and allowed to stabilize for a several minutes, and the patterning of single or arrays of FEBID nanopillars is initiated such that nanopillars grow normal to the plane of the sample. In the case

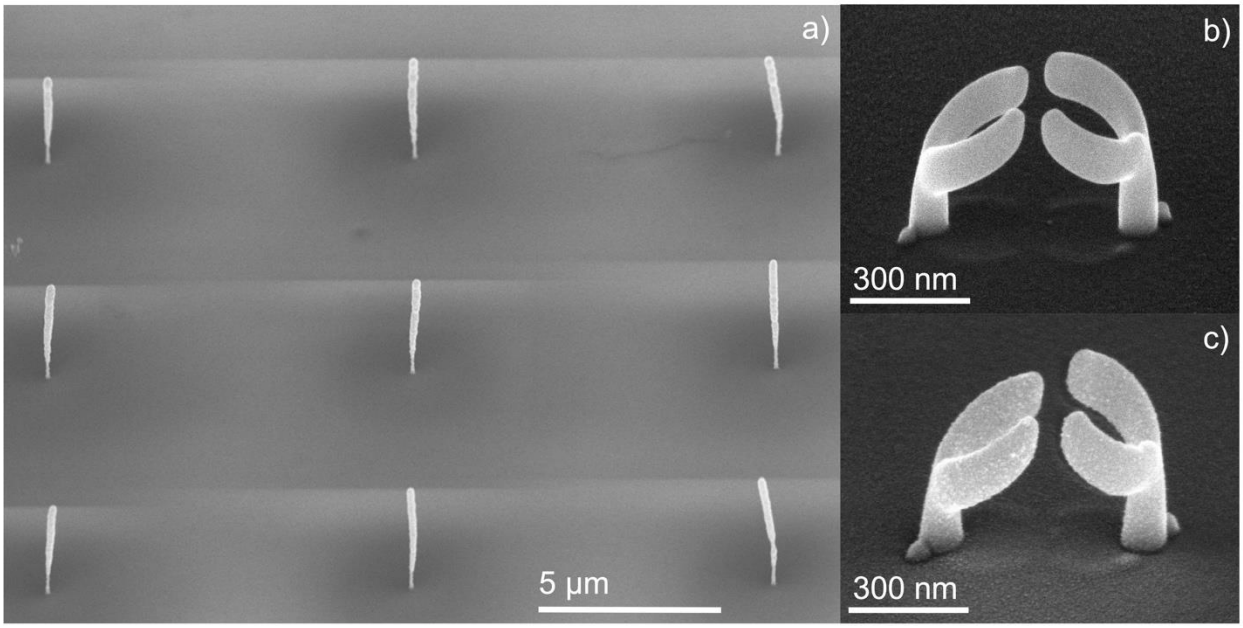

Figure 17. **a**) A 3x3 array of FEBID nanorods grown by FEBID depositions and coated in parallel via the selected area laser processing. Head-to-head comparison of a 3D coupled split ring resonator as FEBID grown **b**) and subsequently deposited with the selected area CVD **c**).

of 5kV, 98pA growth conditions, in-focus depositions result in nanopillar diameters on the order of 50 nm.

Following FEBID nanostructure growth, the GIS is closed, retracted, and the stage is tilted to 52°. At this point, the GIS is reinserted, gas flow re-established, and laser irradiation is initiated with the desired wavelength, power, pulse duration, and repetition rate for the specified duration of the laser CVD process. We have demonstrated little variation in the laser CVD process as a function of incidence angle, so 52° is chosen as a matter of convenience as it allows for SEM imaging of the growing nanostructure during laser irradiation. This enables us to collect time-series data and monitor the growth kinetics of the process. It is important to note that while we are imaging with the SEM during laser CVD, we are continually decomposing the precursor over the field of view via FEBID. At sufficiently high laser duty cycles (product of the pulse width and pulse frequency), where the laser induced growth rates are high, the FEBID contributions are minimal, but as shown in Supporting Information S6, lower laser duty cycle (slower laser growth) can lead to discernible FEBID contributions.

Measurement of the evolving nanostructures through the hundreds of time-series images is accomplished via an automated computer vision and image processing algorithm. Details of this method are discussed in Supporting information S2.

Conclusions

We have demonstrated an *in-situ* selected area photothermal CVD process that can be used to controllably deposit onto complex 3D nanoarchitectures in parallel due to their unique thermal transport properties. The 3D nanostructures were grown via FEBID and subsequently

photothermally deposited using the $MeCpPt^{IV}Me_3$ precursor. Again, it is anticipated that nanostructures grown via other techniques can also be selectively deposited and the laser CVD process should be ubiquitous to other precursors that do not photolytically decompose, thus, by judicious choice of precursor, the laser CVD process can be used to selectively coat the 3D nanostructures and thus functionalize them with a targeted property. Various initial nanopillar geometries were grown and simulations reveal that the unique thermal transport properties of the nanostructures enable the selected area growth. By tuning the thermal conductivity simulations were initially tuned with a fixed geometry to the known precursor decomposition temperature. Subsequent experiments of various nanopillar geometries, laser frequency and pulse widths reveal excellent agreement in the simulated growth temperatures. The experiments suggest the growth mechanism is due to the decomposition of the flux of precursor gas molecules that strike the nanostructure when the nanostructure exceeds the decomposition temperature. Thus, the diameter growth rate is proportional to the cumulative laser on-time, thus higher laser frequency and higher pulse widths lead to faster growth.

Supporting Information

Additional information showing deposition on a variety of substrates, computer-vision details, geometry and parameter effects on thermal modeling, steady-state heating pulse width effects then corresponding 1μs experimental data. SEM videos of Figure 13 deposition; liquid, molten material flow.

Acknowledgments

This research was supported by the Center for Nanophase Materials Sciences, which is a U.S. Department of Energy Office of Science user facility at Oak Ridge National Laboratory (ORNL) Support for SJR was partially provided through Strategic Hire funding through the Laboratory Directed Research and Development Program of Oak Ridge National Laboratory, managed by UT-Battelle, LLC, for the U. S. Department of Energy.

APPENDIX

Supporting Information

S1. Substrate Dependence

The primary driving force for laser-induced growth is the thermal resistance of the nanostructure and thus the substrate properties only weakly affect the growth. We have been able to grow on a variety of substrates with different optical absorption and thermal transport properties. We verified growth on metals, insulators, semiconductors, thin dielectric membranes, nanocrystalline diamond films and observed very little variation in the growth at similar laser conditions. Figure 18 is a illustrates SEM images of various nanopillars that were grown on different substrates. Table 2 provides a summary of original pillar geometry and the laser conditions for the observed growth in Figure 18.

To demonstrate the effects of substrate thermal properties on the peak nanopillar tip temperature, we have performed a series of simulations with common nanopillar geometries, laser conditions, and various substrates on which we have observed the ability to initiate selective deposition. Two nanopillar geometries (diameter = 75 and 300 nm, height = 1300 nm) were simulated on twelve substrate combinations while monitoring the nanopillar tip (hottest point) temperature at steady-state. In all cases, the simulated laser power is 2.7 W and 10 μs pulse, the base substrate is silicon, and the isothermal boundary conditions are placed 10 μm from the nanopillar, which is far enough so that the boundary condition does not alter the solution. For each substrate coating of gold, ultrananocrystalline diamond (UNCD), and silicon dioxide four film thicknesses (10, 100, 500, 1000 nm) were simulated with the PtC_x nanopillar placed on top of these film/silicon wafer stacks. While the substrate thermal properties impact the peak temperature at

the nanopillar tip (Figure 19), their effect is substantially reduced on smaller nanopillar geometries, consistent with our experimental observations that for nearly similar laser conditions we could initiate localized CVD on all of these substrates.

While we have not experimentally verified the larger pillar diameter experiments on multiple substrates, we anticipate that that higher power would be required on higher thermal conductivity substrates. The combination of our experimental results and the various substrate simulations support the conclusion that nanopillar geometry and limitations of thermal transport in confined nanostructures dominate the ability to selectively deposit on the nanostructures. As nanostructure height decreases and diameter increases, a bulk transport regime is approached resulting in a higher degree of substrate dependence. It should be noted that the model ignores laser energy deposited into the substrate, which will slightly alter the thermal profile and substrate dependence. However, we experimentally do not observe delocalized deposition, which indicates the substrate temperature is less than the thermal decomposition temperature. In reality, the absorbed laser energy in the surrounding substrate should result in higher tip temperatures as the thermal gradient would be lower and subsequently reduce heat flux from the nanopillar. In this regard, we are likely underestimating the absolute value of peak nanopillar temperatures, yet the modeled results support our experimental observation. Table 3 contains the physical constants used in these simulations.

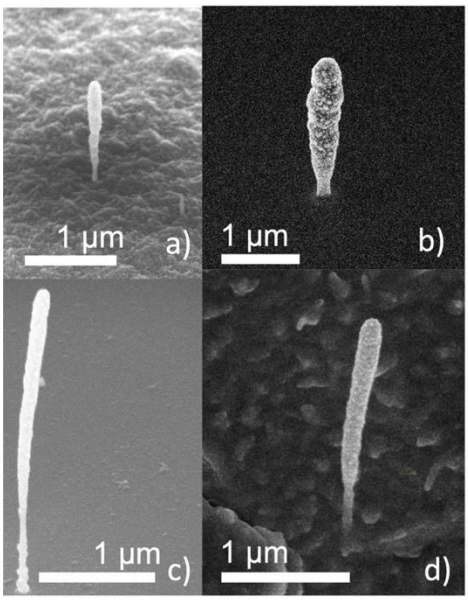

Figure 18. Imaging of selected area deposition at 52° stage tilt on (a) ultrananocrystalline diamond on silicon, (b) 100 nm thermal oxide on silicon, (c) 15 nm thermal nitride membrane and (d) molybdenum TEM half-grids.

Table 2. A summary of laser parameters from Figure 18.

Label	EBID	Laser Power	Laser Duty Cycle	Laser Exposure
a	5 kV, 98 pA 30s	2.7 W	1 kHz, 10 μs (1%)	30s
b	5 kV, 98 pA 60s	2.7 W	1 kHz, 10 μs (1%)	60s
c	5 kV, 98 pA 60s	2.7 W	1 kHz, 10 μs (1%)	20s
d	5 kV, 98 pA 45 s	2.7 W	1 kHz, 10 μs (1%)	30s

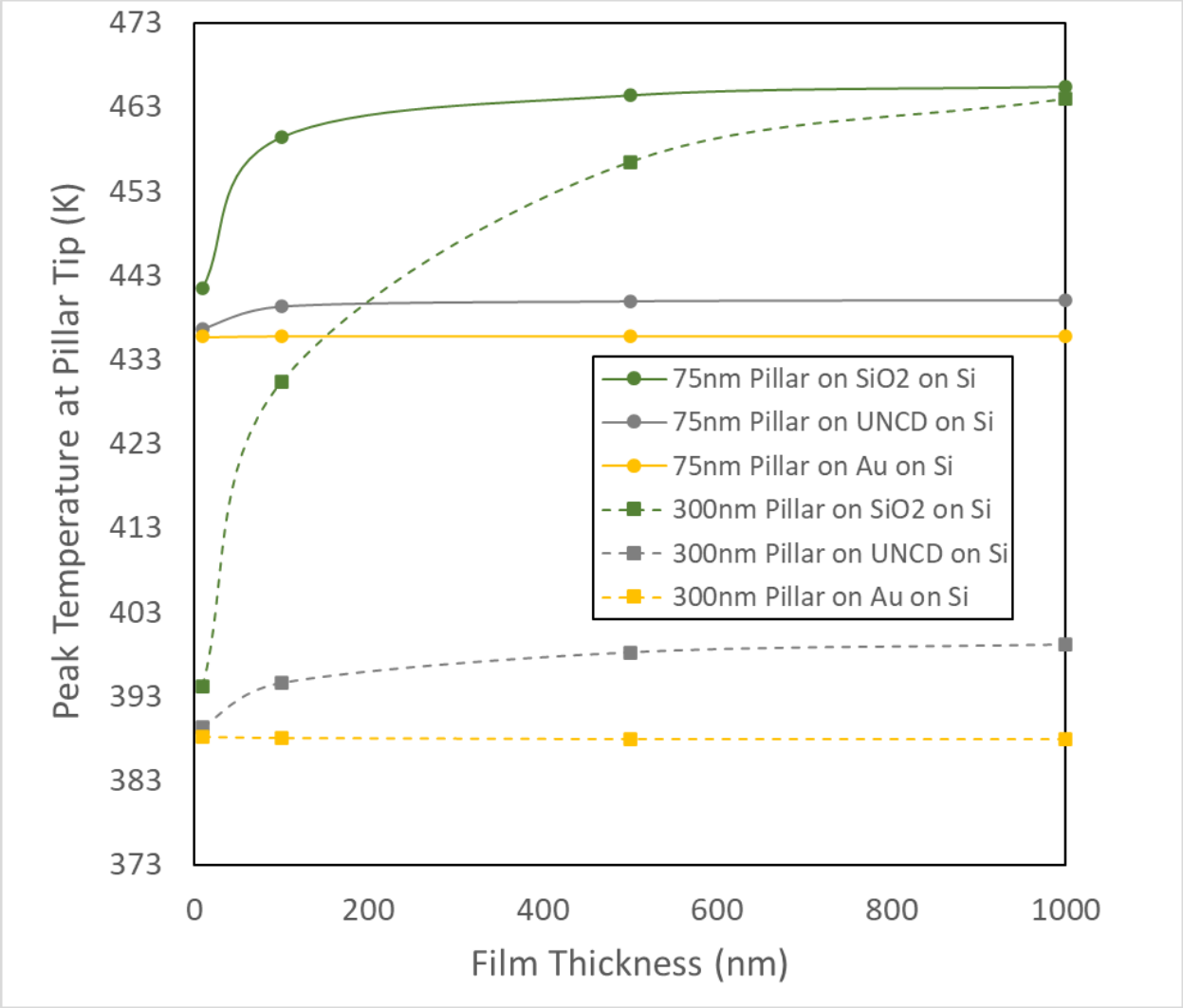

Figure 19. COMSOL modeling results of two nanopillar geometries on four different films on a silicon substrate to illustrate the effect that substrate has on the photothermally induced heating of the nanostructures. Plot of the modeled peak temperature versus film thickness (SiO_2, ultrananocrystalline diamond (UNCD), and Au) for a 75 nm diameter and 300 nm diameter and 1300 nm tall PtC_x nanopillar.

S2. Computer-vision data extraction

The data extraction code is python, using OpenCV as the object recognition backend[148]. Optical character recognition (OCR) on the scale is performed by Google/Hewlett-Packards C/C++ based Tesseract OCR engine.[149] First, in Figure 20 the frame is segmented into 3 parts; the scale, the bar, and the image. The scale undergoes OCR as shown in Figure 21, with most of the processing going towards resolution upscaling and pixelation reduction as Tesseract focuses on natural text recognition and expects a high dpi picture, which is problematic for the course pixelation of the blue extracted region in Figure 20. A small amount of hardcoded error checking is done, such as replacing "S" with "5". The OCR process is shown in Figure 21. In the edge padding step, black pixels are simply added as a border but in subsequent steps the image is magnified to the text region for schematic purposes. Next, the pixels per micrometer is determined by the pixel length of the scalebar and the micrometer measure from OCR. As shown in Figure 21 (Right) the bars of the scalebar are identified by area similarity and the identified shapes measured in pixels, and pixels per micrometer is then simply $\frac{pixels}{scalebar\ \mu m} = \frac{364}{3} = 121.33 \frac{pixels}{\mu m}$. Finally, object identification in the SEM image is performed in Figure 22. The 'grayscale' step is RGB color conversion to a value in [0, 1]. Multiple blurring steps are performed to reduce both natural SEM point noise and induced systematic noise from coincident laser processing. Edges are detected, dilation and erosion are performed to close gaps, and then objects are identified. Diagnostic videos are created by overlaying the original SEM frames with annotations and the filled objects that were identified. Annotation data is generated from the pixel-per-micrometer measure previously determined, and height is measured as the vertical measure of the objects

Table 3. Material properties for substrate dependence simulations

Substrate	Thermal Conductivity W/(m-K)	Cp J/(kg-K)	Density kg/m^3
SiO_2	1.4	730	2200
UNCD	10	690	2900
Au	317	129	19300
Si	131	700	2329
PtC_x	8.6	700	1250

Figure 20. An initial video frame highlighted with the segmented parts – yellow is the image, red the scalebar and blue the scale.

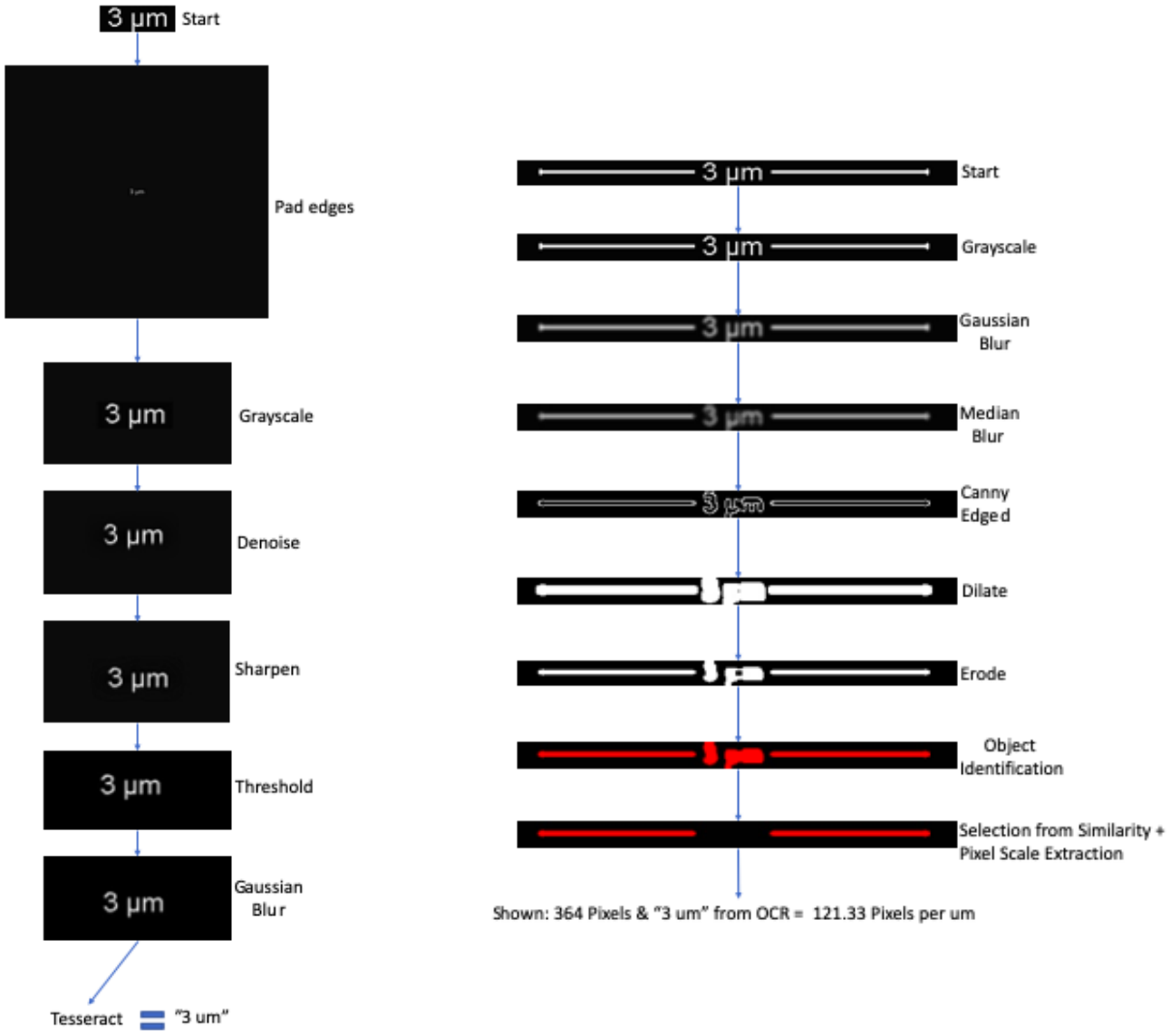

Figure 21. (Left) The scale extraction process, (Right) scalebar pixel distance determination.

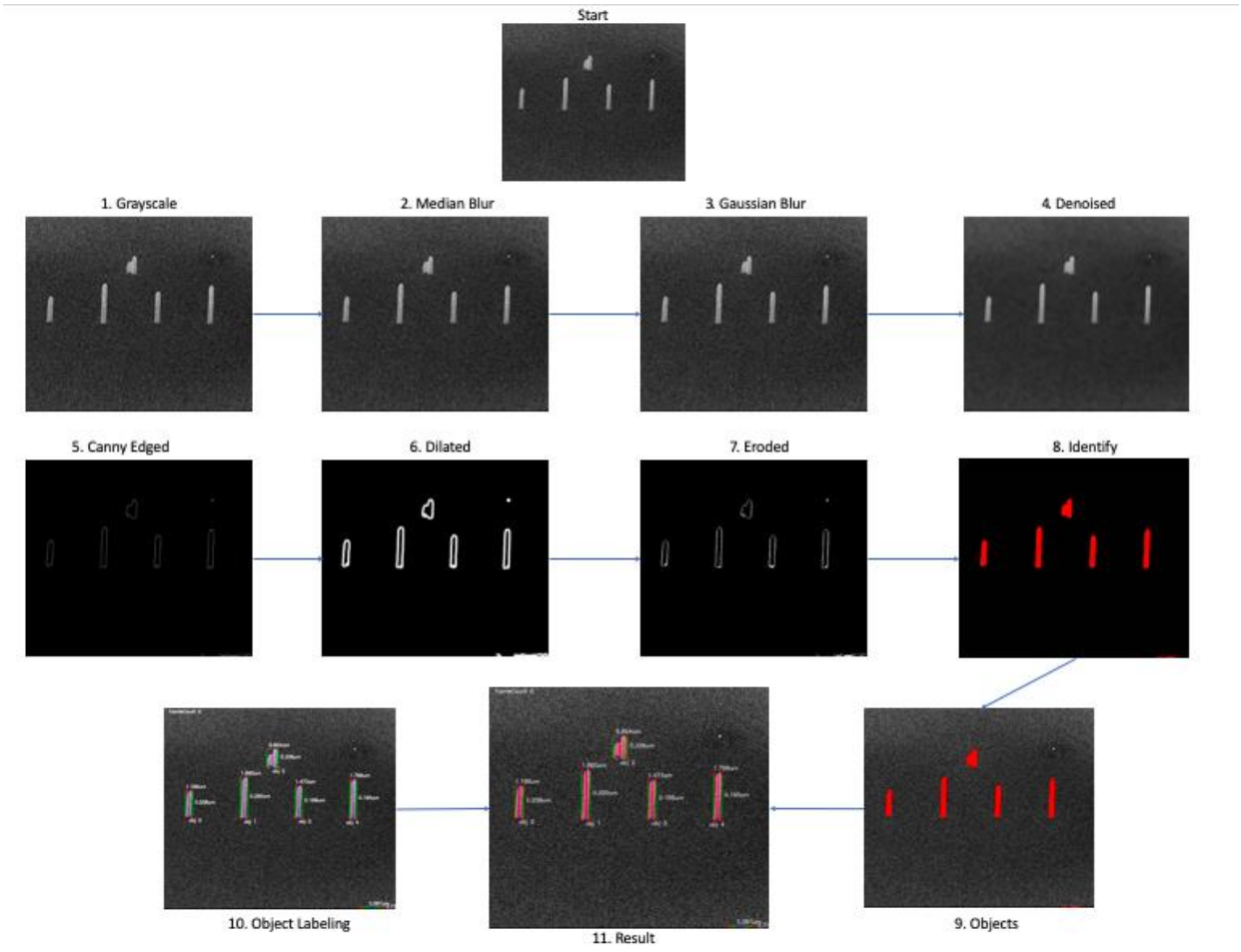

Figure 22. The video labeling process, where identified object dimensions are overlaid on the original video.

bounding box and the diameter is measured as the average diameter of the central 60% of the identified pillar object, excluding the top and bottom 20%.

S3. Thermal Simulation Parameter Sensitivity Analysis

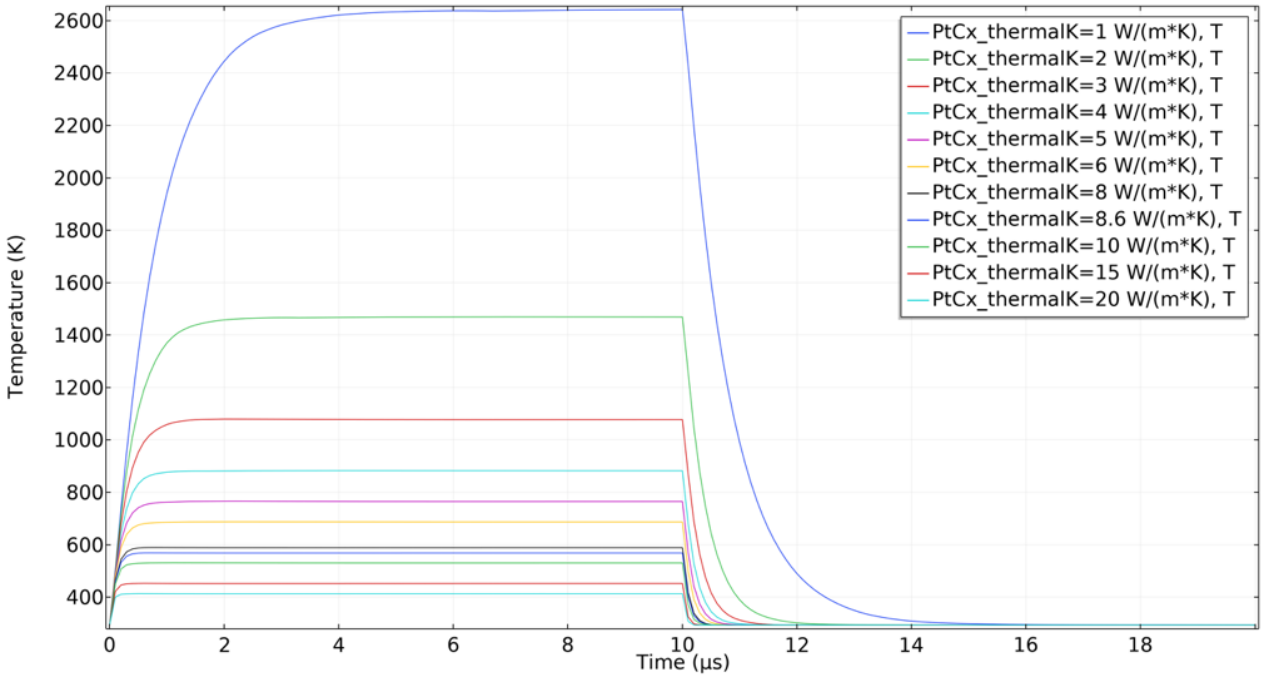

Figure 23. The rise and maximum temperatures reached as estimated using the heat flow finite-element modeling COMSOL approach as described in the main text, at a variety of pillar thermal conductivity values. The modeling domain was a 1.5 µm tall by 200 nm diameter PtC_x pillar on a 4-inch, 500 um Si wafer with 293 K boundary conditions at the bottom and outer radius of the wafer. The incident laser was 5 W ($r_{laser} = 50$ µm), 191 µJ was input as a heat source to the pillar by the ratio $Q_{in} = \frac{D_{pillar} * H_{pillar}}{\pi * r_{laser}^2}$ as schematically shown in Figure 27. Constant rate heat flow from the laser was provided to the pillar for the duration of the 10 µs pulse, and the model was ran for twice the pulse width. The other PtC_x material parameters were: density – 1250 kg/m^3, heat capacity at constant pressure -700 J/(kg*K), n - 1.87 and k – 0.31.

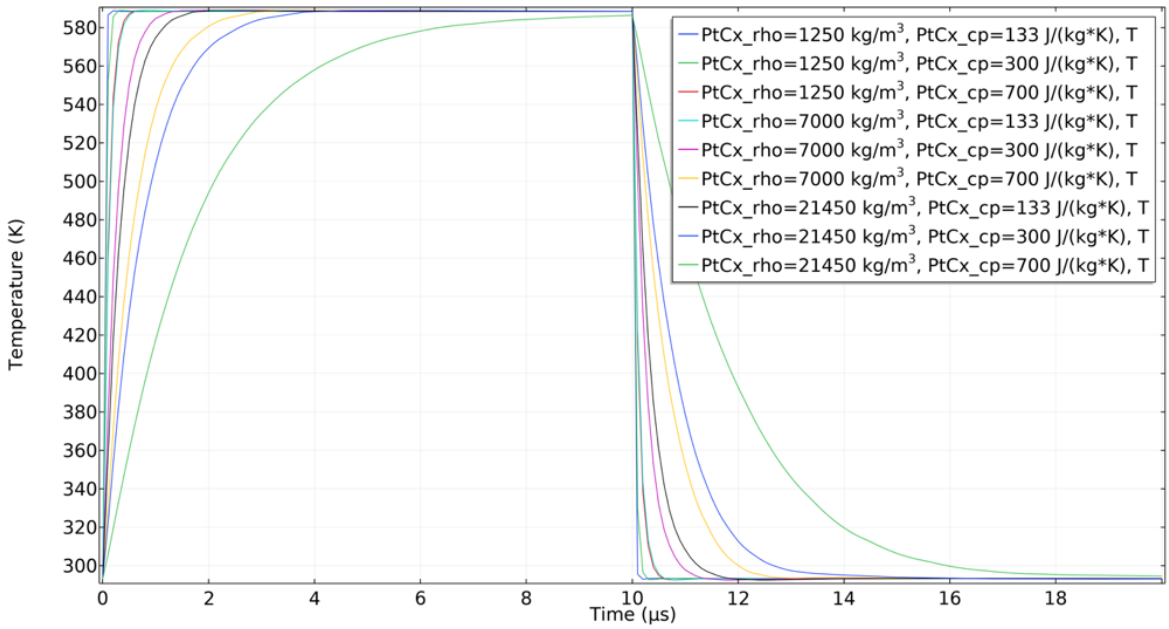

Figure 24. The rise and maximum temperatures reached as estimated using the heat flow finite-element modeling COMSOL approach as described in the main text, at many different combinations of density and heat capacity at a common pressure. The modeling domain was a 1.5 µm tall by 200 nm diameter PtC_x pillar on a 4-inch, 500 um Si wafer with 293 K boundary conditions at the bottom and outer radius of the wafer. The incident laser was 5 W ($r_{laser} = 50$ µm), 191 µJ was input as a heat source to the pillar by the ratio $Q_{in} = \frac{D_{pillar} * H_{pillar}}{\pi * r_{laser}^2}$ as schematically shown in Figure 27. Constant rate heat flow from the laser was provided to the pillar for the duration of the 10 µs pulse, and the model was ran for twice the pulse width. The other PtC_x material parameters were: thermal conductivity – 8 W/(m*K), n - 1.87 and k – 0.31.

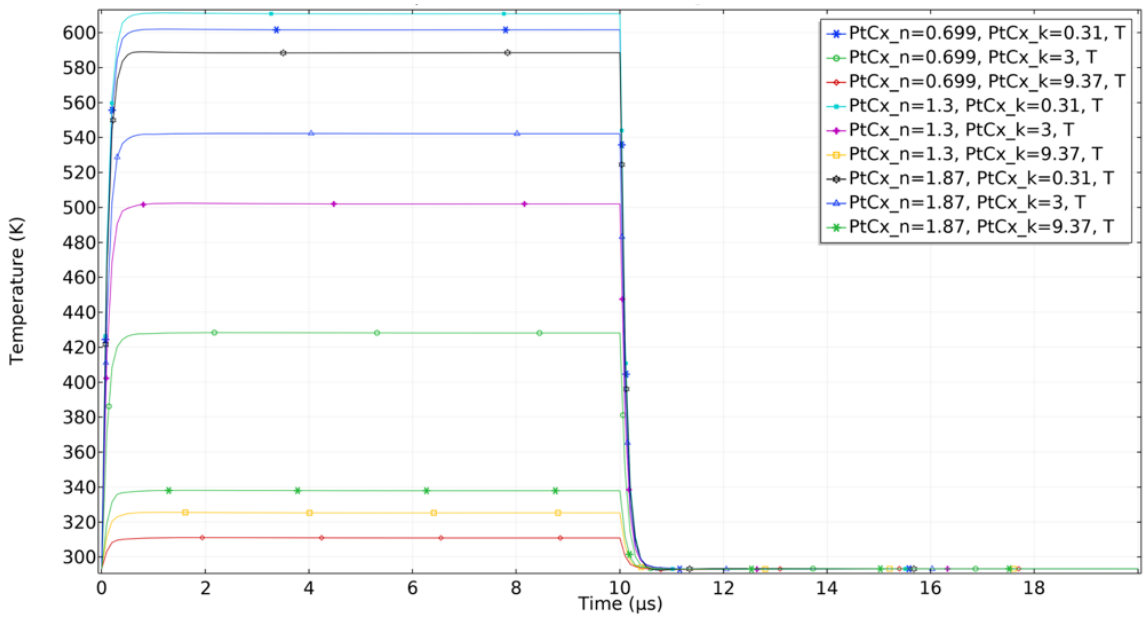

Figure 25. The rise and maximum temperatures reached as estimated using the heat flow finite-element modeling COMSOL approach as described in the main text, with many different combinations of optical parameters ranging from amorphous carbon to pure platinum. The modeling domain was a 1.5 µm tall by 200 nm diameter PtC_x pillar on a 4-inch, 500 um Si wafer with 293 K boundary conditions at the bottom and outer radius of the wafer. The incident laser was 5 W (r_{laser} = 50 µm), 191 µJ was input as a heat source to the pillar by the ratio $Q_{in} = \frac{D_{pillar} * H_{pillar}}{\pi * r_{laser}^2}$ as schematically shown in Figure 27. Constant rate heat flow from the laser was provided to the pillar for the duration of the 10 µs pulse, and the model was ran for twice the pulse width. The other PtC_x material parameters were: thermal conductivity - 8 W/(m*K), density – 1250 kg/m^3, heat capacity at constant pressure -700 J/(kg*K).

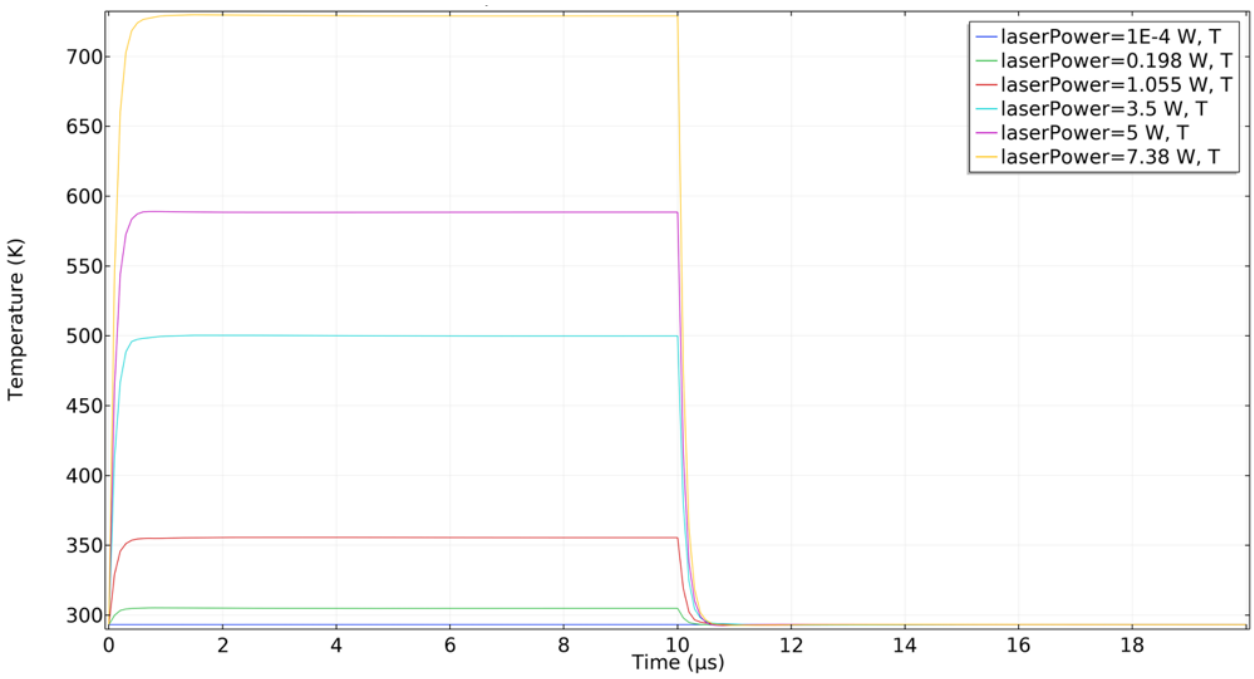

Figure 26. The rise and maximum temperatures reached as estimated using the heat flow finite-element modeling COMSOL approach as described in the main text, at a variety of incident laser powers. The modeling domain was a 1.5 µm tall by 200 nm diameter PtC_x pillar on a 4-inch, 500 um Si wafer with 293 K boundary conditions at the bottom and outer radius of the wafer. The radius of the laser was $r_{laser} = 50$ µm, and the wattage was input as a heat source to the pillar by the ratio $Q_{in} = \frac{D_{pillar} * H_{pillar}}{\pi * r_{laser}^2}$ as schematically shown in Figure 27. Constant rate heat flow from the laser was provided to the pillar for the duration of the 10 µs pulse, and the model was ran for twice the pulse width. The other PtC_x material parameters were: thermal conductivity - 8 W/(m*K), density – 1250 kg/m^3, heat capacity at constant pressure -700 J/(kg*K), n - 1.87 and k – 0.31.

S4. Geometry of Thermal Modeling

Figure 27 is a visual illustration of the general model implementation showing boundary conditions, pillar geometry, and fractional heat source term applied to the nanopillar. The laser radiation absorbed by the substrate is ignored in this case and only the fraction of laser light incident on the nanopillar is included in the heat source term. The lower plane and outer cylindrical wall of the substrate are isothermal boundary conditions while all other surfaces are considered insulating boundaries *($\nabla T=0$)*.

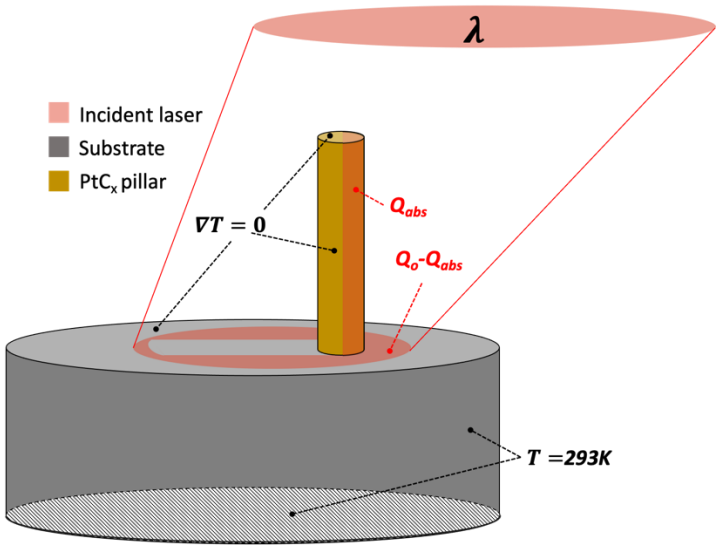

Figure 27. A visualization of the geometry of the simulations and the fraction of laser power absorbed by the nanopillar.

S5. Pulse Width Length Dependence

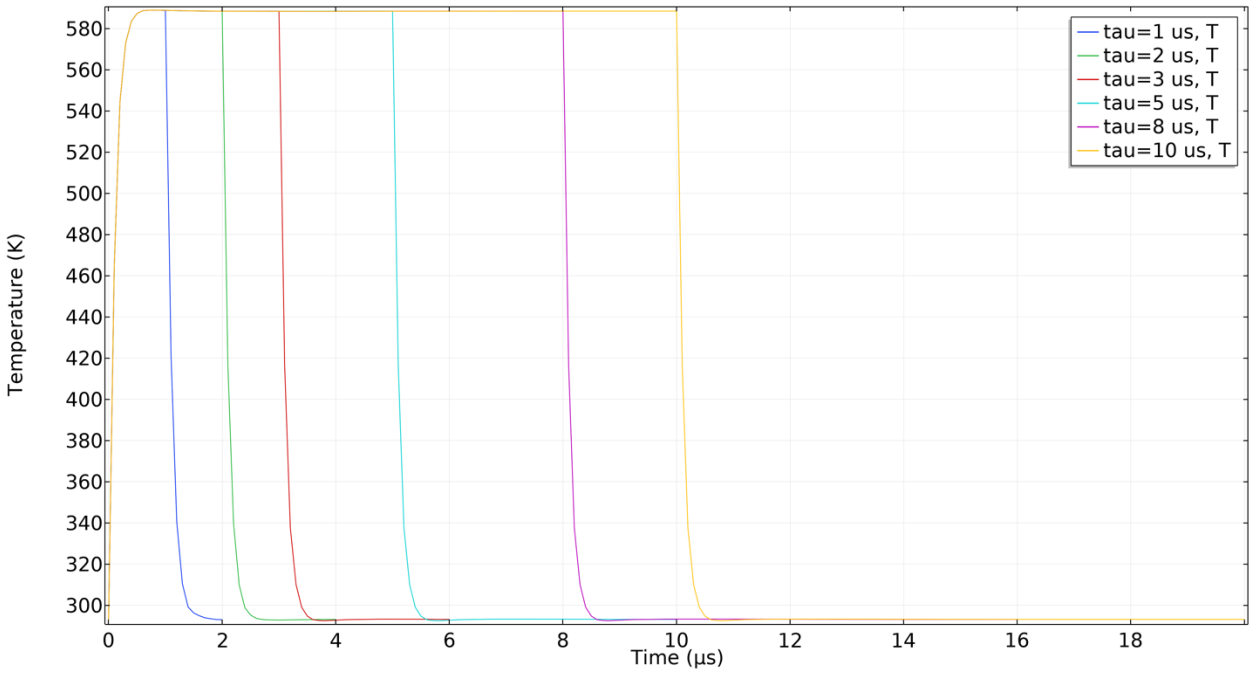

Figure 28. The rise and maximum temperatures reached as estimated using the heat flow finite-element modeling COMSOL approach as described in the main text, at a variety of pulse widths. The modeling domain was a 1.5 µm tall by 200 nm diameter PtC_x pillar on a 4-inch, 500 um Si wafer with 293 K boundary conditions at the bottom and outer radius of the wafer. The incident laser was 5 W ($r_{laser} = 50$ µm), 191 µJ was input as a heat source to the pillar by the ratio $Q_{in} = \frac{D_{pillar} * H_{pillar}}{\pi * r_{laser}^2}$ as schematically shown in Figure 27. Constant rate heat flow from the laser was provided to the pillar for the duration of the pulse, and the model was ran for twice the pulse width. The other PtC_x material parameters were: thermal conductivity - 8 W/(m*K), density – 1250 kg/m^3, heat capacity at constant pressure -700 J/(kg*K), n - 1.87 and k – 0.31.

S6. 1μs Laser Pulse Width Data

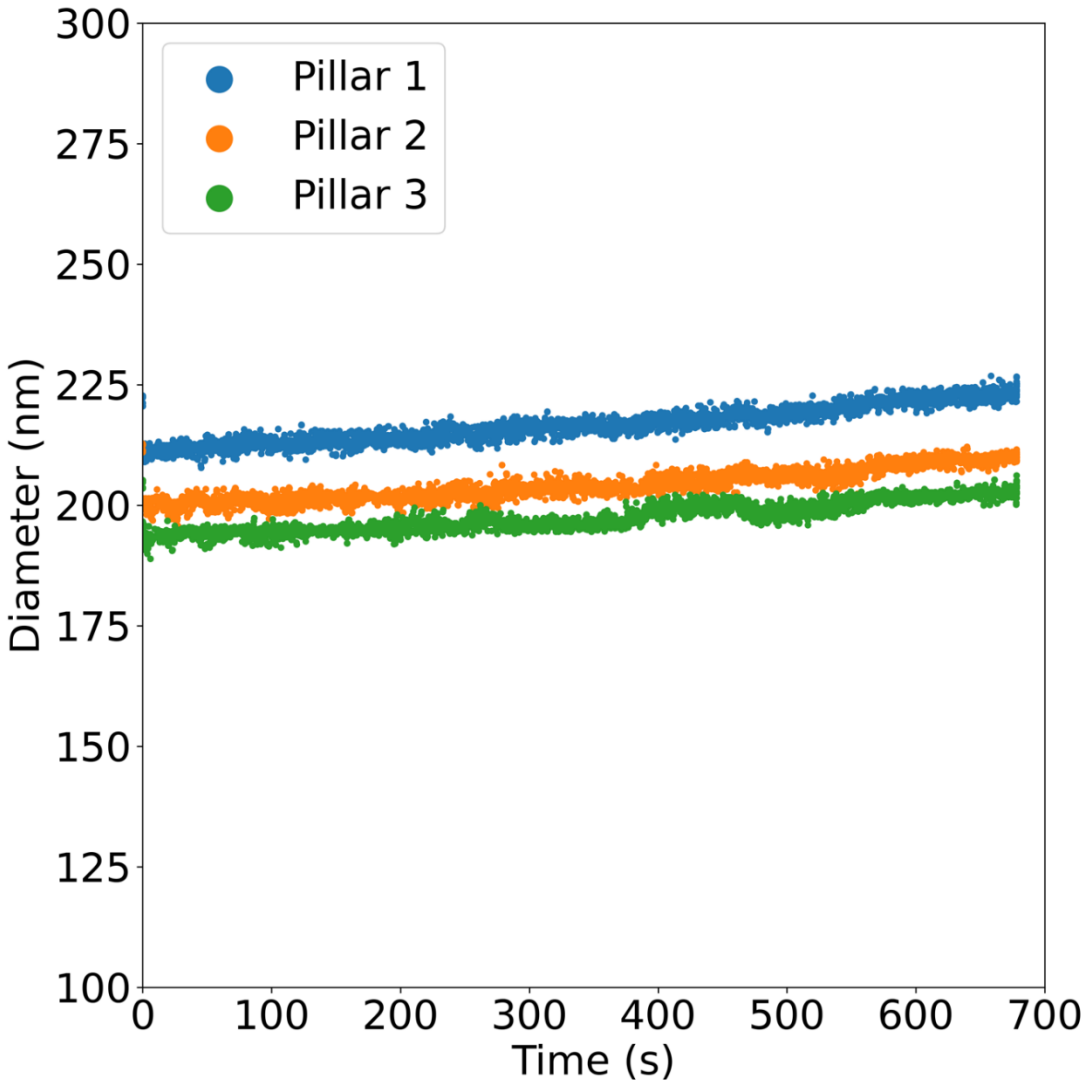

Figure 29. 1 µs pulse width tests show EBID contributions at long scanning times and supports the idea that the nanopillar does not reach precursor decomposition temperature within a 1 µs pulse.

CHAPTER II

Selected Area Deposition of High Purity Gold for Functional 3D Architectures

John Lasseter[1], Philip D. Rack[1] and Steven J. Randolph[2,*]

[1.] Department of Materials Science and Engineering, University of Tennessee, Knoxville, Tennessee 37996, United States

[2.] Center for Nanophase Materials Sciences, Oak Ridge National Laboratory, Oak Ridge, Tennessee 37831, United States

*Corresponding author email: randolphsj@ornl.gov.

Author Contributions

This work was published in MDPI Nanomaterials[150]. John Lasseter performed the depositions, imaging, computer vision processing, and energy dispersive x-ray spectroscopy (EDX/EDS) and led the finite-element modeling. Finite-element modeling was assisted by Steven Randolph. Dale Hensley grew the carbon nanofiber sample. John Lasseter wrote the first draft and Steven Randolph and Philip D. Rack edited the manuscript. Philip D. Rack and Steven Randolph conceptualized the experimental plan.

Abstract

Selected area deposition of high purity gold films onto nanoscale 3D architectures is highly desirable as gold is conductive, inert, plasmonically active, and can be functionalized with thiol chemistries which are useful in many biological applications. Here we show that high purity gold coatings can be selectively grown with the $Me_2Au(acac)$ precursor onto nanoscale 3D architectures via a pulsed laser pyrolytic chemical vapor deposition process. The

selected area deposition is achieved due to the high thermal resistance of the nanoscale geometries. Focused electron beam induced deposits (FEBID) and carbon nanofibers are functionalized with gold coatings and we demonstrate the effects that laser irradiance, pulse width, and precursor pressure have on the growth rate. Furthermore, we demonstrate selected area deposition with a feature targeting resolution of ~ 100 and 5 μm, using diode lasers coupled to a multimode (915 nm) and single mode (785 nm) fiber optic, respectively. The experimental results are rationalized via finite element thermal modeling.

Keywords: selected area deposition, chemical vapor deposition, laser heating, 3-dimensional nanostructures

Introduction

Three-dimensional printing of functional nanoscale materials and architectures is very challenging. To date, focused electron and ion beam induced deposition is capable of high-fidelity and complex geometries, but the deposited material is typically contaminated by residual precursor by-products. While a significant amount of research has been invested in developing new precursors[18,151–155] and purification strategies[156–163], functional and pure 3D deposits remain a significant challenge. While research and applications of 3D printing of mesoscale and macroscale objects have surged in recent years, pushing sub-mm 3D printing has been more limited. As recently reviewed by Hirt et al[164] only several techniques have been developed such as direct ink writing, electrohydrodynamic printing or laser-assisted electrophoretic deposition, meniscus-confined electroplating, and laser induced photoreduction. While each technique has relative strengths and weaknesses, most only approach the mm scale. Scanning electron and ion beam induced deposition techniques

however have recently been shown to be capable of 10s of nm scale resolution with high-fidelity 3D printing (see Winkler, et. al. [7]) for recent review. Two photon lithography is capable of three dimensional nanoprinting below the optical diffraction limit[165] but limited photoresist availability limits the materials that can be accessed.

We recently demonstrated selected area deposition of PtC_x coatings on FEBID PtC_x deposits via a pulsed laser chemical vapor deposition (CVD) process.[121] The selected area deposition is a result of the constrained thermal transport that occurs in the pseudo 1-dimensional nanoscale architectures and thus deposits specifically on the FEBID structures with negligible growth on the substrate. The process was shown to be consistent with a pyrolytic CVD process where the precursor decomposition temperature is reached by controlling the laser power density and pulse width as well as the dimensions and thermophysical properties of the 3D FEBID template. The total growth is a function of the time that the nanostructure exceeds the dissociation temperature and the precursor flux on the nanostructure surface during the exceeded temperature. While the concept was demonstrated using the well-known $MeCpPt^{IV}Me_3$ precursor, consistent with thermal CVD results[143], residual carbon remains in the selected area coatings.

Given the limited functionality of the PtC_x material presented in our previous work, here we explored the dimethyl(acetylacetonate)gold(III) ($Me_2Au(acac)$) precursor as gold is conductive, resistant to oxidation, exhibits low plasmonic losses, is biocompatible, and its surfaces can be chemically modified through processes such as thiolation. While nanoscale 3D applications are a bit limited due to the FEBID purity described above, several example applications have emerged. For instance, magnetic 3D structures[166–168], vibrating sensors[169],

chiral[170–177] and split ring resonator[178,179] and other[8,180] plasmonic devices, scanning probe tips[181–183], and some nanomechanical applications[184,185] have all been demonstrated.

Selected area pyrolytic laser CVD of gold has been thoroughly studied by Baum et al for circuit repair applications in the 1980s.[186] They showed pure pyrolytic CVD could be achieved with the $Me_2Au(acac)$ precursor when the laser induced temperature rise from a focused laser exceeded the ~ 450 K decomposition temperature.[187] CVD studies with the $Me_2Au(acac)$ precursor are in good agreement with this decomposition temperature[188] however, with O_2 and ozone co-reactants have demonstrated precursor decomposition as low as 363 K[189] Here we show selected area deposition can be achieved using the $Me_2Au(acac)$ precursor and be extended to three dimensions with sub-diffraction limit resolution (pillar diameter << laser wavelength), while yielding high purity functional gold coatings of a variety of nanostructures.

For instance, we demonstrate selected area growth on 3D FEBID structures and carbon nanofibers via localized pyrolytic decomposition of the $Me_2Au(acac)$ precursor. In this work, various experimental geometries and materials, laser conditions (power density, pulse width, duty cycle, and laser wavelength) as well as precursor pressure are explored to rationalize the selected area deposition process. We also demonstrate the use of both multimode fiber optic delivery (λ=915 nm and 100 μm beam diameter) and single mode fiber optic delivery (λ=785 nm, ~ 5 μm beam diameter). COMSOL finite element thermal modeling is also performed to validate some of the experimental findings. We investigate deposition rate is proportional to the temperature and flux of precursor gas molecules that impinges on the nanostructures when the laser heated nanostructure exceeds the decomposition threshold. Because we employ a pulsed laser system, the deposition rate can also be controlled by the laser duty cycle (product

of the pulse width and the frequency). Chemical analysis confirms that high purity functional coatings (>95 at.%) can be achieved that far exceeds what FEBID alone can accomplish. We show that not only can we selectively control the growth on the 3D geometry, but also tune the growth in the z-dimension through control of the deposited laser energy.

Methods

FEBID nanopillars are grown in an FEI Nova 600 dual beam microscope using the typical Scanning Electron Microscopy (SEM) conditions of 5 keV, 98 pA using a stationary beam to grow the vertical pillars. Dimethyl(acetylacetonate)gold(III), also known as $(CH_3)_2Au(C_5H_7O_2)$, was purchased from STREM (CAS 14951-50-9). Table 4 overviews the growth times and precursors pertinent for each figure. Carbon nanofibers were grown via a plasma enhanced CVD process using either a patterned nickel catalyst or dewetted nickel film [see Melechko, et. al.[190] for overview]. To selectively coat the FEBID and carbon nanofibers, we used a WAVIKS Inc. optical delivery system mounted onto the FEI Nova 600 for in situ selected area growth directly onto the FEBID nanostructures. Two laser sources are used: 1) a 16 W (externally measured optical power) 915 nm wavelength laser diode that is coupled to a multimode fiber optic and a 100 μm diameter spot size and thus a maximum irradiance of ~ 2.1 GW/m2; 2) a 220 mW (externally measured optical power) 785 nm wavelength laser diode coupled to a single mode fiber with approximately 10 μm diameter spot size and thus a maximum irradiance of ~ 2.8 GW/m2. The lasers are modulated with a pulse width generator capable of ~ 10 ns-CW pulse widths and up to 2.5 MHz frequency. In-situ scanning electron microscopy (SEM) was performed during the selected area growth. Energy Dispersive X-ray

Table 4. Deposition Parameters

Figure	Precursor Temperature (°C)	Template Material	Template Precursor	Laser Irradiance $\left(\frac{MW}{m^2}\right)$	Laser Wavelength (nm)	Laser On-Time (s)
Figure 30	30	PtC_x	$MeCpPt^{IV}Me_3$	140	915	0.2
Figure 31	30	AuC_x	$Me_2Au(acac)$	13.4-58.5	915	4.3
Figure 32	30	PtC_x	$MeCpPt^{IV}Me_3$	140-1164	915	5.5
Figure 33	30	PtC_x	$MeCpPt^{IV}Me_3$	127	915	0.2-10
Figure 34	25, 30, 35	AuC_x	$Me_2Au(acac)$	140	915	0.3
Figure 35	30	VACNF	$C_2H_2 + NH_3$	598, 140-548	785, 915	0.3-1.2

Spectroscopy (EDS, EDX) measurements were performed in a Zeiss Merlin scanning electron microscope. EDS Measurements were taken at 5kV, 205 pA with P/B-ZAF corrections. Point spectra were 60 second collections with 3% dead time, the map was a 5 minute collection with drift correction and 6.6 nm pixel spacing. In our EDS quantification, we observe measurable Ga from the focused ion beam milling and Si from the scattered electron interacting with the substrate; thus we ignore these contributions in the Au/C quantification. Table 5 presents a range of physical parameters used in this study.

As illustrated in Figure 30, the CVD process is a pulsed process due to the pulsed laser source that selectively heats the nanostructures. Pyrolytic CVD occurs for the duration in which the nanostructure temperature exceeds the dissociation temperature of the precursor. For sufficiently long pulse widths relative to the heating rise time, the growth rate is proportional to the laser on-time (product of the laser duty cycle and processing time) and the flux of the precursor molecules. We focus here on low duty cycle pulsed growth as, for instance, high irradiance continuous wave laser exposures can lead to overheating and failure in our optical delivery system. The low duty cycle ensures adequate cooling of the system during operation, and allows us to perform the in situ imaging to discern the growth kinetics. Furthermore, we are able to control the growth at sub-monolayer per pulse growth rates for superior control. While some nanostructure/substrate systems would in theory permit for continuous wave growth, some combinations could lead to substrate heating at longer time constants and thus eliminate the selected area affect.

Table 5. System Physical Parameters

Parameter	Value
Laser	785 nm (single mode, $r = 5\ \mu m$), 915 nm (multi mode, $r = 50\ \mu m$)
Laser Intensity	13.4-1164 $\left(\frac{MW}{m^2}\right)$
Laser Pulse Width	500 ns – 50 μs
Laser Repetition Rate	200 Hz – 1 MHz
FEBID SEM Voltage	5 kV
FEBID SEM Current	98 pA
Typical SEM Base Pressure	5 $\mu Torr$
SEM Room Temperature	25 °C
Typical Precursor Temperature	30 °C

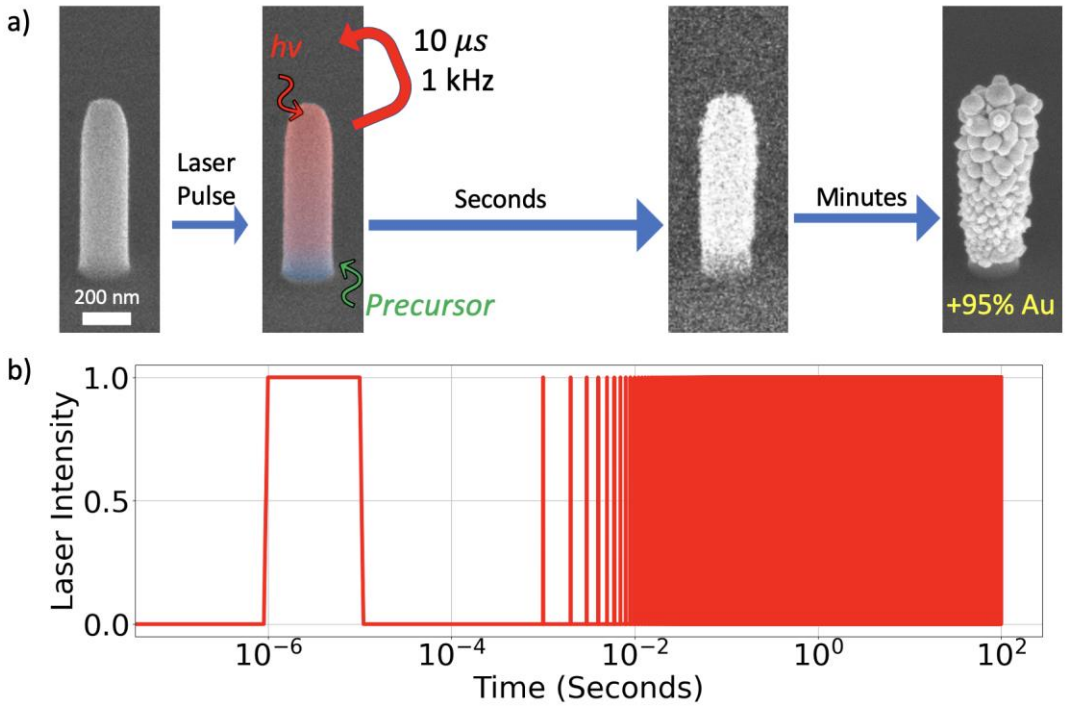

Figure 30. Schematic illustrating the temporal evolution during the selected area deposition process. a) SEM images of an as-deposited FEBID nanopillar and subsequent images during the deposition process, where one is artificially colored to visualize the thermal effect of the laser. b) A log time versus irradiance plot illustrating the various time scales that are operative where for instance the pulse width 10 μs, the repetition rate is a ms and the total processing time 200s (with a 0.1% duty cycle and thus total laser on time of 0.2 s).

Finite-element modeling through the commercial COMSOL package was used to investigate the onset temperatures. The radiative beam is governed by the Beer-Lambert law equation:

$$\frac{\boldsymbol{e_i}}{[\![\boldsymbol{e_i}]\!]} * \boldsymbol{\nabla I_i} = -\boldsymbol{\kappa I_i}$$

where $\boldsymbol{I}$ is the radiative intensity, $\boldsymbol{e_i}$ is the orientation of the $\boldsymbol{i^{th}}$ beam, and $\boldsymbol{\kappa}$ is the absorption coefficient. This model has three key assumptions: 1) the radiative beam in the absorbing medium is collimated and each beam propagates always in the same direction, 2) the light experiences no refraction, reflection, or scattering within the material itself and 3) There is no significant emission of the material in the wavelength range of the incident light. The radiative heat source $\boldsymbol{Q_r}$ corresponding to the energy deposited by the radiative beam is:

$$\boldsymbol{Q_r} = \sum_{\boldsymbol{i}} \boldsymbol{\kappa I_i}$$

The heat transfer in solids is modeled by the heat balance equation:

$$\boldsymbol{\rho C_p}\left(\frac{\boldsymbol{\partial T}}{\boldsymbol{\partial t}}\right) + \boldsymbol{\nabla} * (\boldsymbol{q} + \boldsymbol{q_r}) = \boldsymbol{Q}$$

where $\boldsymbol{\rho}$ is the density, $\boldsymbol{C_p}$ is the specific heat capacity at constant stress, $\boldsymbol{T}$ is the absolute temperature, $\boldsymbol{q}$ is the heat flux by conduction, $\boldsymbol{q_r}$ is the heat flux by radiation, and $\boldsymbol{Q}$ contains additional heat sources.

COMSOL default silicon parameters were used; a specific heat (C_p) of 700 $\frac{\boldsymbol{J}}{\boldsymbol{kg*K}}$, a density ($\boldsymbol{\rho}$) of 2329 $\frac{\boldsymbol{kg}}{\boldsymbol{m^3}}$, and a thermal conductivity ($\boldsymbol{k}$) of 131 $\frac{\boldsymbol{W}}{\boldsymbol{m*K}}$. An absorption coefficient of 25600 m^{-1} at 915 nm was used for silicon[191].

Previous literature values for PtC_5 FEBID deposits[121] were used as starting points, and the nanostructure thermal conductivity was tuned until the pillar temperature reached the thermal CVD temperature of the $Me_2Au(acac)$, ~450 K. The optical parameters used at 915 nm for the nanopillars were index of refraction of n=1.87, and an extinction coefficient of k=0.31[141]. The laser was modeled as a flat top beam with a direction vector of $\begin{bmatrix} \mathbf{0.419} \\ \mathbf{0.0588} \\ \mathbf{-0.906} \end{bmatrix}$ to mimic the laser angle during deposition. The nanopillar thermal parameters were: a specific heat (C_p) of 700 $\frac{\boldsymbol{J}}{\boldsymbol{kg*K}}$[142], a density ($\boldsymbol{\rho}$) of 1250 $\frac{\boldsymbol{kg}}{\boldsymbol{m^3}}$[142], and a thermal conductivity ($\boldsymbol{k}$) tuned to 1.05 $\frac{\boldsymbol{W}}{\boldsymbol{m*K}}$.

Carbon nanofibers were modeled as cones with experimentally determined height, base and tip widths using COMSOL's radiative beam in absorbing materials and heat transfer in solids as previously described. A single tip was used for modeling, but experimental geometries often have complex multi-tips. Graphite optical parameters used at 915 nm were an index of refraction of n=2.2, and an extinction coefficient of k=1.3[192]. The nanopillar thermal parameters were a specific heat (C_p) of 1000 $\frac{\boldsymbol{J}}{\boldsymbol{kg*K}}$[193], a density ($\boldsymbol{\rho}$) of 2200 $\frac{\boldsymbol{kg}}{\boldsymbol{m^3}}$[194], and a thermal conductivity ($\boldsymbol{k}$) tuned to 190 $\frac{\boldsymbol{W}}{\boldsymbol{m*K}}$. A tetrahedral mesh with a minimum element size of 10nm was used on the nanopillars, and the nanofiber tetrahedral mesh minimum element size was 40nm. Higher-resolution meshes were tested, but the same peak temperatures were reached and smoother gradients were the only effect.

Results and Discussion

Figure 31 a) is a scanning electron micrograph of the four as-deposited AuC_x (where x=9) FEBID nanopillars grown from the $Me_2Au(acac)$ precursor that have comparable original diameters and various height [see SEM movie capture in the supplemental information SI-1]. Figure 31 d) is a plot of the nanopillar diameter versus the laser on-time (product of the processing time and duty cycle) and total processing time, where the laser power is incrementally increased over time from 105 to 459 mW (or 13.4-58.5 MW/m^2). The laser is pulsed at constant 1 kHz frequency with 10 μs pulse width and an image processing routine described in[121] is used to measure the average diameter of the top 67% of each nanopillar. Figure 31 b) is a scanning electron micrograph of the resultant gold coated nanopillars after the experiment. To rationalize the onset temperature, we performed COMSOL finite element modeling of the peak temperature of the various nanopillar geometries and laser power for growth onset [see SI-2 for details] where the relevant properties used in the finite element model are listed. As illustrated in Figure 31 c), all the onset temperatures exceed the thermal decomposition temperature of the $Me_2Au(acac)$ of ~ 450 K. The inset in Figure 31 d) is a table listing the pillar diameter and height at the onset of growth, the modeled onset temperature and gold growth rate (normalized to the laser on-time) for each pillar (note short black line on each plot denoting where the growth rate was taken). As expected, the laser power/irradiance that initiates growth is proportional to the FEBID nanopillar height; the taller pillars have higher thermal resistance and thus the pillars exceed the $Me_2Au(acac)$ dissociation temperature at lower laser power. As illustrated in Figure 31 c) the substrate heating is negligible whereas significant heating is realized in the nanopillars thus the realization of the selected area growth.

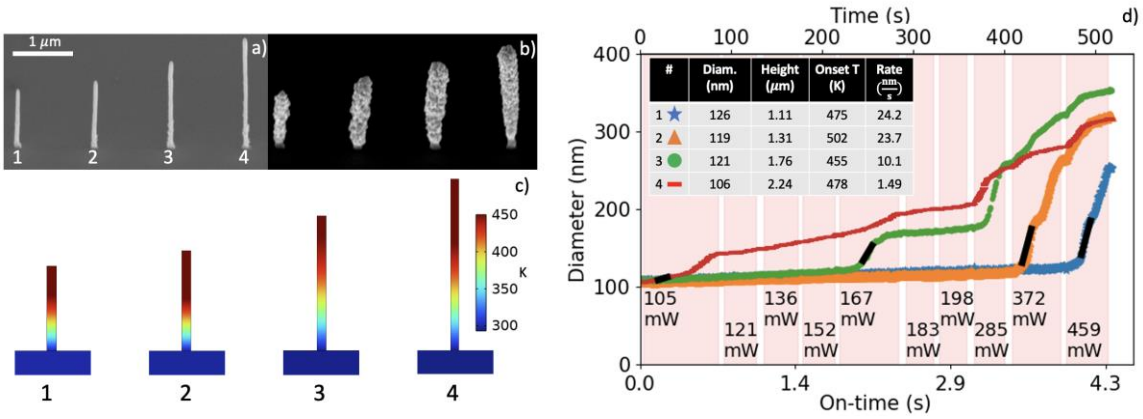

Figure 31. SEM images of the a) as-deposited AuCx nanopillars and b) after the cumulative gold deposition realized during the laser power study. c) Results from finite element modeling of the temperature profile at the end of the laser pulse width for the various nanopillars at the associated laser onset powers. d) Plot of nanopillar diameter versus laser on-time (bottom x-axis) and processing time (top x-axis) with increasing laser power noted; the highlighted red regions correspond to the labeled laser powers. Inset table of nanopillar diameter, height, modeled onset temperature, and onset growth rate.

As expected, the tips are the hottest and the scanning electron micrographs after growth reveal a slightly tapered growth consistent with the thermal profile. Note that the high growth rate changes in the final three power intervals are due to larger increases in power. The slight increase in the pillar diameter with time before the photothermal decomposition is attributed to electron beam induced deposition caused by the in situ secondary electron imaging.

Interestingly, once the gold layer is initiated, the optical and thermal properties change to a composite structure where the growing gold layer is optically in series with the AuCx core material relative to the laser flux and is thermally in parallel relative to the substrate heat sink. While a concentric bi-layer model using gold surrounding an AuC_x core was explored, the optical absorption below ~ 50 nm is very sensitive to the surface roughness[195], which significantly enhances the optical absorption. Using standard gold properties has the effect of significantly reducing the structure temperature below the decomposition temperature primarily due to significant reflectance, but also due to the enhanced thermal conduction (see SI-3 for example and model details). Because we observe continued growth, we expect the observed surface roughness enhances the optical absorption and thus growth is sustained at lower-than-expected optical powers. As shown in Figure 31 d), the growth rates during a constant power interval can vary, which suggests temperature changes attributed to the evolving optical and thermal properties of the composite structure.

While EDS on individually grown nanopillars were attempted, inevitable scattering into the original PtC_x or AuC_x nanopillars made it difficult to distinguish the Au and C atomic composition of the laser grown gold coatings. Figure 32 a), illustrates a series of 4 PtC_5 nanopillars that were grown in close proximity and subsequently exposed to a pulsed laser at

10 μs pulse width, 1k Hz frequency where the laser power was progressively ramped from 1.1 to 9.14 W (140-1164 MW/m^2) over 10 minutes for the selected area growth (b) and c)) until all pillars had merged into a continuous wall. The nanopillar was Ga+ focused ion beam milled into a thin lamella as illustrated in Figure 32 d) to measure the composition via energy dispersive x-ray spectroscopy (EDS). Several point spectra are shown in Figure 32 e) and inset is the associated Au EDS map of the entire lamella. By subtracting out the substrate Si and O peaks, points 1 and 2 reveal gold compositions of > 95 at. %. Some variation in the carbon content as revealed in position 3 is evident (see C and Si maps in supplemental information SI-4); penetration of the electron beam and possible interaction with the FEBID core is suspected. Overall, the selected area pulsed laser chemical vapor deposition from the $Me_2Au(acac)$ produces high purity Au nanostructure coatings.

To interrogate the $Me_2Au(acac)$ growth process in more detail we performed a selected area growth study using PtC_5 nanopillars grown via FEBID using the trimethyl(methylcyclopentadienyl)platinum(IV) precursor and varied the laser pulse duration and frequency at a constant irradiance (127 MW/m^2). Pillars 1-5 are all grown at a constant duty cycle of 1%, pillar 5 is 10% and pillar 6 is 50%. Figure 33 a) illustrates the average nanopillar diameter versus cumulative laser on-time for various laser pulse widths/frequencies and b) is a plot of the modeled temperature versus time plot for each laser pulse width. Figure 33 c)-i) are SEM images of the gold-coated nanopillars after selected area growth. At pulse widths 5 μs and above, the growth rate is fairly consistent except for the 20 μs, 500 Hz growth, which has comparable early growth rates, but tapers off at ~ 6x10-2 seconds. Pillars 1-4 all have fairly uniform coatings that extend to the base of the nanopillars. The 2 μs pulse width

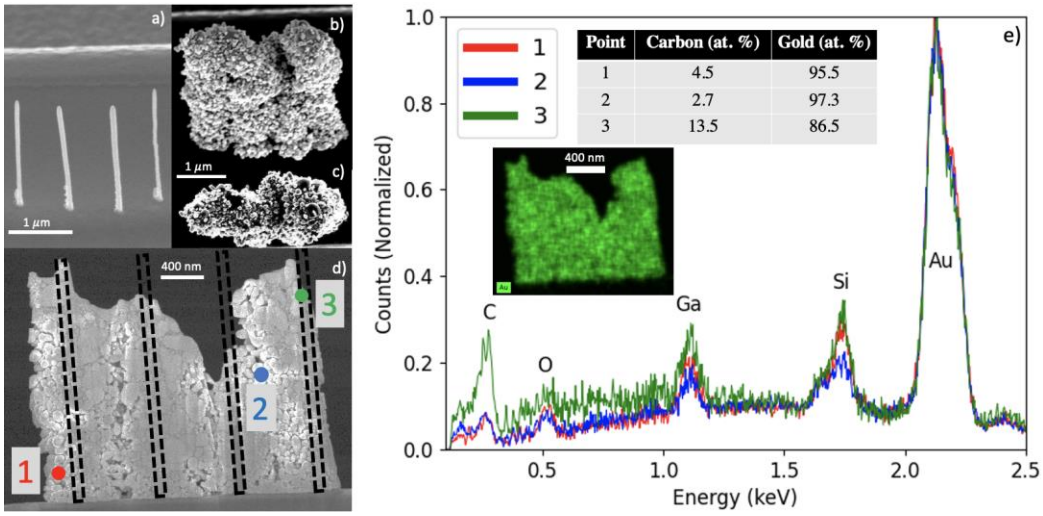

Figure 32. a) A 52° tilted SEM image of the as-deposited PtC5 nanopillars. b) A 52° tilted SEM of image of the nanopillars after gold selected area deposition. c) Top-down SEM image of b). d) The Ga+ FIB thinned lamella and EDS measurement locations; the black dashed boxes estimate the positions of the original FEBID nanopillars. e) The corresponding EDS spectra, taken at 5 keV 205 pA. The inset in e) is the Au EDS map of the image in d).

gold thickness (~50 nm) is noticeably lower and the coating only extends ~2/3 from the tip of the nanopillar. Finally, the 1 and 0.5 μs growths are indiscernible at 2x10-1 s, but do exhibit growth at 1 and 2 orders of magnitude longer laser on-times, respectively. As shown, these nanopillars exhibit a rise and decay time of ~2 μs. Of course, this time constant is related to the product of the thermal resistance and capacitance and is given by $\frac{\rho C_p V}{kA}$ where ρ is the density, C_p is the heat capacity at constant pressure, V is the volume, k is the thermal conductivity and A is the surface area. As the pulse width is decreased, the rise time becomes a significant fraction of the pulse width, thus the time above the dissociation temperature (for illustration see line drawn at 450 K) is a smaller fraction of the total laser on-time. At pulse widths lower than the rise time, the integrated time above the dissociation temperature diminishes and thus, much longer laser on-times are required for observable growth. Furthermore, the temperature evolution at short pulse widths limits the heating at the base of the nanopillars. Figure 33 j-p) illustrate the temperature profile of the nanopillars at the end of each pulse width, where the peak temperature is listed above the image. Interestingly, at the optimized 1 W/m-K thermal conductivity, the 5-50 μs pulse widths all have similar temperature profiles where a majority of the nanopillar exceeds the dissociation temperature. However, the 2, 1, and 0.5 μs pulse widths exhibit a progressively shorter region of the nanopillar tip region that exceeds the decomposition temperature. Thus, the growth rates and position sensitive deposition as a function of pulse width, self-consistently suggest the tuned thermal conductivity value is correct. One interesting feature that is also observed is that the grain structure in general becomes coarser with increasing pulse width.

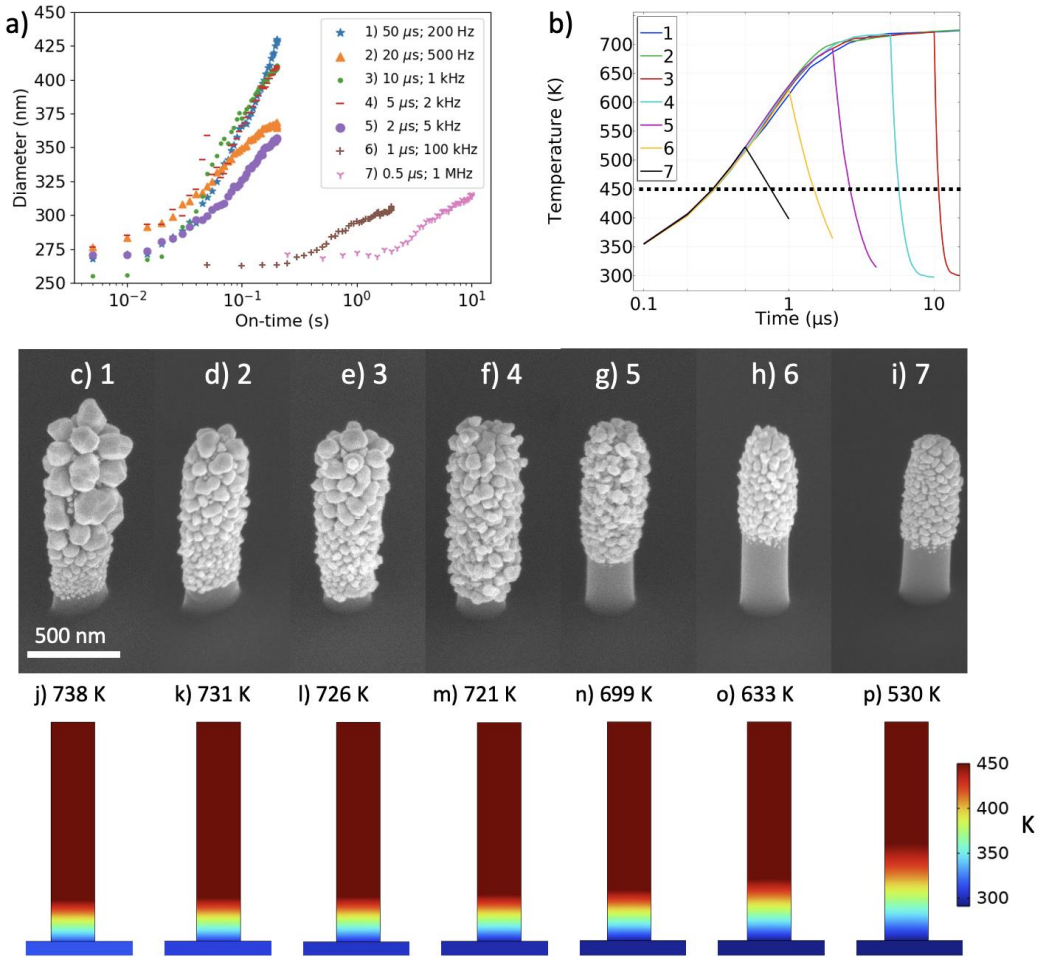

Figure 33. a) A plot of the nanopillar diameters as a function of laser on-time at different pulse widths. b) The simulated time versus temperature focused on 0.5, 1, 2, 5 and 10 μs pulse widths, as longer pulse widths have similar profiles to 10 μs. c-i) SEM images of the nanopillar after processing at different pulse widths. j-p) Modeled temperature profiles of the nanopillars at the end of the specified laser pulse width and peak temperature listed above the nanopillar.

Next we explored the effect of precursor pressure on the growth rate by comparing the growth on similar geometry AuC_x FEBID nanopillars and varying the precursor crucible temperature (25, 30 and 35 ^oC) to raise the $Me_2Au(acac)$ vapor pressure/precursor flux during selected area deposition. For each crucible temperature the same laser conditions of 10 μs, 1 kHz and 140 MW/m^2 irradiance was used. Figure 34 a) compares a plot of the average nanopillar diameter as a function of laser on-time for the various crucible temperatures, which clearly shows that the higher crucible temperature yields higher growth rates. Figure 34 b)-d) are SEM images of the gold-coated AuC_x FEBID nanopillars grown at 25, 30 and 35 ^oC crucible temperatures, respectively; note that coarsening of the gold grains occurs at higher crucible temperatures. The average growth rates over the 0.3 s laser on-time are 92, 125 and 210 nm/s for the 25, 30 and 35 °C crucible temperatures, respectively. This agrees with our previous hypothesis[121] that the growth rate is controlled by the precursor flux and the time that the object's temperature is greater than the precursor dissociation temperature.

Finally, to test that the selected area deposition is a more generalized phenomenon that is compatible with structures other than FEBID grown materials, we investigated functionalizing carbon nanofibers (CNF).[196] The CNFs were grown via a plasma enhanced chemical vapor deposition process using lithographically patterned nickel catalyst.[197,198] Figure 35 shows an array of CNFs a) prior to laser irradiation and b) subsequent to a 20 second selected area gold deposition (343 MW/m^2, 1kHz, 10 μs) and c) is a lower magnification image illustrating the approximate 100 μm laser spot size. To demonstrate z-axis selected area deposition control, Figure 35 d) shows an individual as-grown CNF, and post-growth images after a series of 30 s (300 ms laser on-time) selected area growths with 10 μs pulse width and 1 kHz frequency and

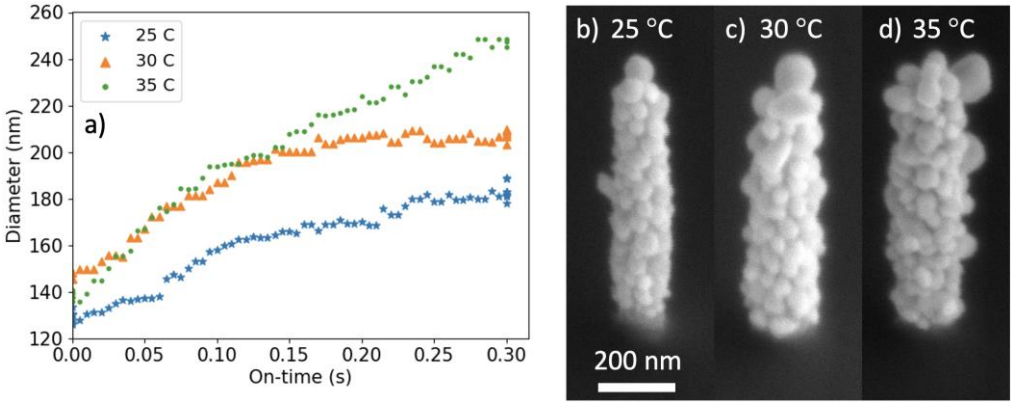

Figure 34. a) A plot of the nanopillar diameters as a function of laser on-time at different crucible temperatures. b-d) SEM images of the nanopillar after processing at b) 25 °C, c) 30 °C, and d) 35 °C.

e) 140, f) 242, g) 343 and h) 548 MW/m^2 irradiance. Note in Figure 35 d-h, that the nanofiber has a secondary branch associated with the initial CNF. This is due to a stochastic splitting in the catalyst nanoparticle during the CNF plasma enhanced chemical vapor deposition process and not associated with the selected area deposition process which conformally coats the entire exposed fiber. Figure 35 i), illustrates that the length from the tip that is functionalized increases as a function of increasing power and as expected the gold thickness increases on the previously grown areas. We modeled this CNF geometry using optical and thermal parameters of graphite as described in the methods section and note that the inset temperature maps of the nanofibers at each power show that the location along the CNF where the temperature exceeds the 450 K dissociation agrees well with the region of the selected area growth (for illustrative purposes the temperature color is set to a maximum of 450 K -- see supplemental information SI-5 for results where color scale is set to the maximum temperature located at the CNF tip).

While we did not perform continuous wave exposures to protect the optical delivery system, we performed a continuous wave simulation on the CNF system under the same 915 nm wavelength, 548 MW/m^2 laser conditions. At these conditions the substrate heating exceeds the precursor dissociation temperature, thus we lose the desired site selectivity. See supplemental information SI-5 for modeling results of the temperature profile at the 0.3 s continuous wave total laser-on time.

To illustrate higher resolution selected area growth, we also tested a 785 nm wavelength laser diode coupled to a single mode optical fiber, which can yield comparable irradiance values at a spot size on the order of 5 μm.[199] The pulse width and frequency were 10 μs and 1kHz, respectively, and the average laser irradiance was 598 MW/m^2. Figure 35 j) illustrates that we

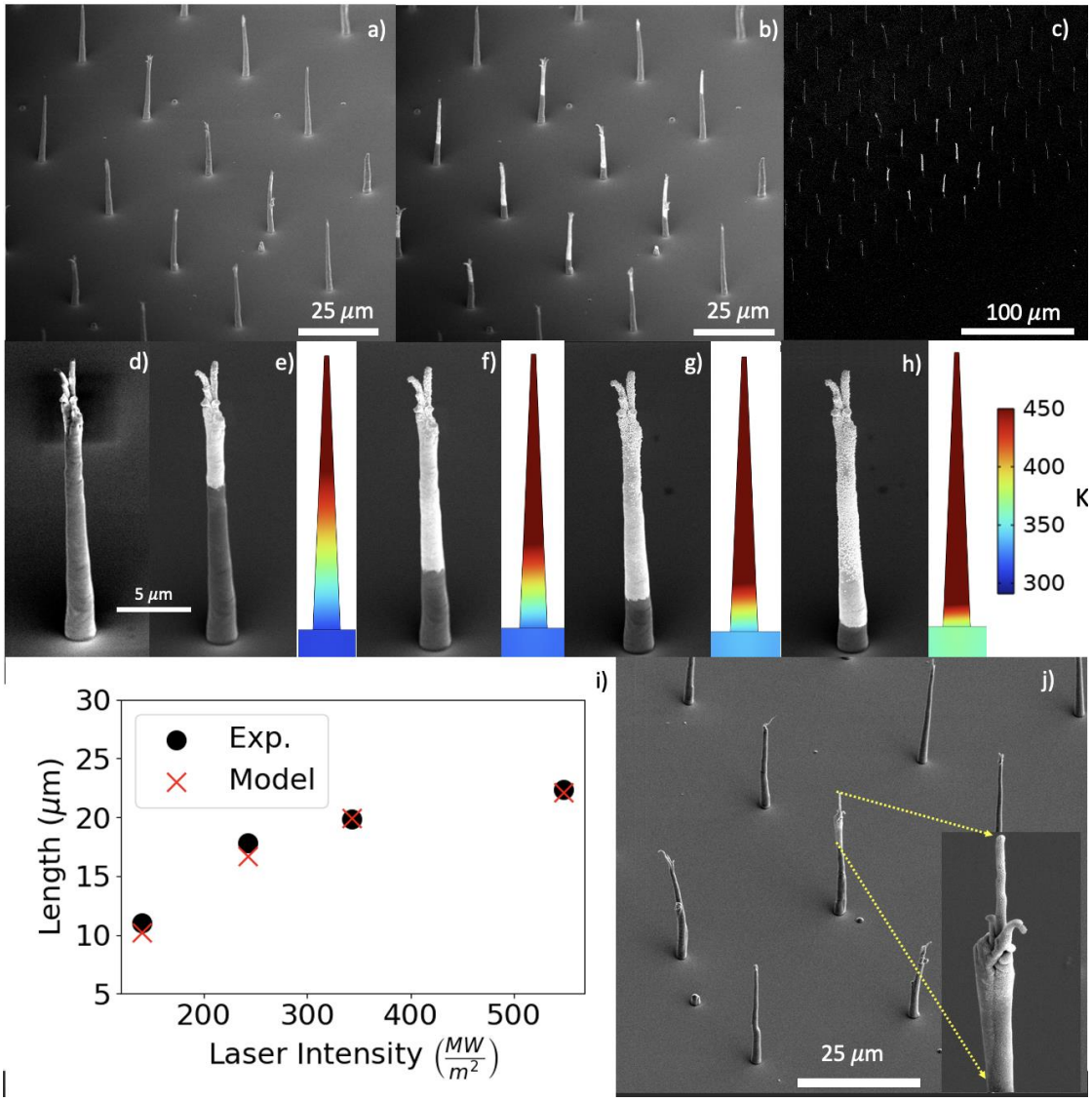

Figure 35. a) SEM image of a VACNF array before processing. b) SEM image of array after laser processing. c) The laser processed array at lower magnification, showing the area selectivity. d-h) SEM images of a different CNF on the same sample, showing the spatial selectivity of the process as a function of laser power by exposing one fiber repeatedly while stepping the laser power at 915 nm 10 μs, 1kHz; d) as grown e) 140, f) 242, g) 343 and h) 548 MW/m2 irradiance . Inset next to d)-h are temperature profiles of the carbon nanofiber exposed to the specific laser power illustrating the isothermal position extends farther down the CNF at higher laser power. i) A plot of the laser power vs measured vertical deposition length and modeled isothermal 450 K position. j) SEM image demonstrating higher resolution selected area deposition using a laser coupled single mode laser diode with a spot size of ~ 5 μm diameter.

are able to selectively target and functionalize a single CNF in this array with a more localization at the CNF tip.

Conclusion

Selected-area deposition of high-purity gold coatings on 3D nanostructures are demonstrated using the $Me_2Au(acac)$ precursor via a pulsed laser pyrolytic CVD process, which occurs due to the unique thermal properties of the nanoscale geometries. Good optical coupling and constrained thermal conduction allows selective heating of the nanostructures and negligible heating of the underlying substrates. Because the nanopillar geometry controls the thermal conduction, the irradiance required to induce growth is proportional to the aspect ratio of the nanostructure. Above the irradiance onset value, if the laser pulse width is sufficiently longer than the thermal rise time, then the growth rate is proportional to the laser on-time (i.e. the product of the duty cycle and processing time) and the flux of precursor gas that impinges on the surface during this time. For pulse widths shorter than the thermal rise time, the growth rate is decreased because the effective time that the nanostructure is greater than the precursor dissociation temperature is decreased. As the growth rate is proportional to the precursor flux and the time above the dissociation temperature, at constant laser parameters, we show that the growth rate is proportional to the localized precursor pressure. We additionally validated selected area deposition as a more generalized nanostructural phenomenon by demonstrating the process on carbon nanofibers, where z-dimension of gold functionalization is shown to be controllable via its proportionality to laser irradiance. In addition to the 915 nm wavelength laser diode coupled to a multimode fiber optic capable of 100 μm spatial resolution, we demonstrate 5 μm feature targeting resolution using a 785 nm wavelength laser diode coupled

to a single mode fiber optic. Finite element thermal simulations corroborate each of the experimental studies. Chemical analysis of the gold coatings indicate purity in excess of 95 at. % indicating the process is promising for producing functional gold coatings of nanostructured architectures.

Author Contributions

Conceptualization, J. L., P. R. and S. R.; Data curation, J. L.; Formal analysis, J. L., P. R. and S. R.; Funding acquisition, P. R. and S. R.; Investigation, J. L. and S. R.; Methodology, P. R. and S. R.; Project administration, P. R. and S. R.; Resources, S. R.; Software, J. L.; Supervision, P. R. and S. R.; Validation, P. R. and S. R.; Writing – original draft, J. L., P. R. and S. R.; Writing – review & editing, J. L., P. R. and S. R..

Acknowledgments

This research was supported by the Center for Nanophase Materials Sciences, which is a U.S. Department of Energy Office of Science user facility at Oak Ridge National Laboratory (ORNL). Support for S.J.R. was partially provided through Strategic Hire funding through the Laboratory Directed Research and Development Program of Oak Ridge National Laboratory managed by UT-Battelle, LLC, for the U.S. Department of Energy. Three UTK SMART program summer interns; Gabriel Watson, Bryson Hedrick, and Daniel Narcho assisted with data collection in Figure 2. We thank Dr. Dale Hensley for the CNF samples.

APPENDIX

Supporting Information

SI-1 Figure 31 SEM Video of $Me_2Au(acac)$ CVD on $Me_2Au(acac)$ FEBID Nanopillars

See attached files. A SEM video of selected area deposition on FEBID nanopillars via the laser-induced deposition process is shown (8x speed). This experiment is investigating the effect of laser irradiance, where all nanopillars are simultaneously exposed to the large 100 μm 915 nm laser spot. The irradiance starts at 13.4 MW/m^2 and is stepped up to 58.5 MW/m^2 over time. The video shows the selectivity of the deposition process, as irradiance increases different geometries are pushed to the pyrolytic CVD temperature and begin deposition.

SI-2 Figure 31 Finite-Element Modeling of $Me_2Au(acac)$ FEBID Nanopillars Deposition Onset

Previous literature values for PtC_5 FEBID deposits[121] were used as starting points, and the nanostructure thermal conductivity was tuned until the pillar temperature reached the thermal CVD temperature of the $Me_2Au(acac)$, ~450 K, shown in Figure 36. The optical parameters used at 915 nm for the nanopillars were index of refraction of n=1.87, and an extinction coefficient of k=0.31. The laser was modeled as a flat top beam with a direction vector of $\begin{bmatrix} 0.419 \\ 0.0588 \\ -0.906 \end{bmatrix}$ to mimic the laser angle during deposition. The nanopillar thermal parameters were: a specific heat (C_p) of 700 $\frac{J}{kg*K}$, a density (ρ) of 1250 $\frac{kg}{m^3}$, and a thermal conductivity (k) tuned to 1.05 $\frac{W}{m*K}$.

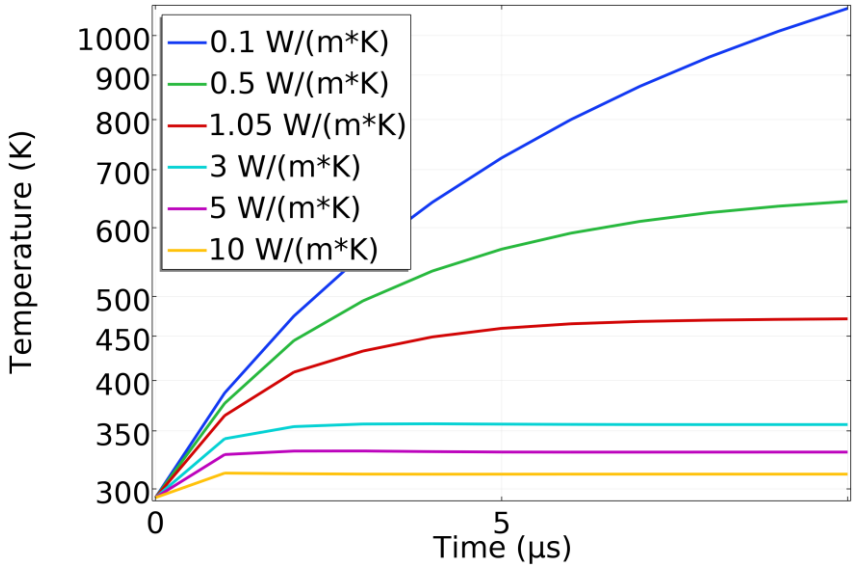

Figure 36. Plot of temperature versus time for finite-element modeling of different thermal conductivities for parameter tuning. The modeled pillar is pillar 4 from main text Figure 31, 106 nm wide and 2.24 um tall with a 106 mW (13.5 MW/m^2 irradiance) incident laser.

SI-3 Figure 31 Finite-Element Modeling of $Me_2Au(acac)$ FEBID Nanopillars with a Bilayer Au-FEBID Model

Given that EDX results indicate a high-purity gold coating, we attempted to model the FEBID as deposited pillar and the conformal gold coating as a bi-layer thermal model. The laser radiation model described above is not compatible with a material bi-layer, thus, we used COMSOL's heat transfer in solids and developed a bi-layer model based on power a modified heat source that we previously described[121]. In this model we use a simple series optical absorption model in which we have a vacuum/gold interface and a gold/PtC_x interface and reflection and absorption is determined at each interface and layer, respectively. For thin films below or close to the electron mean free path of 41 nm, the thermal conductivity is thickness dependent. The thickness dependent thermal conductivity equation was derived by fitting reference data[200] to a power function: $58.656 * D_{Au}^{0.2272}$, where D_{Au} is the gold thickness and is plotted in Figure 37. Furthermore, reflectivity is also thickness dependent if the layer is below the absorption depth. The thickness dependent Au reflectivity equation was $0.44 * (1 - e^{-15.5*D_{Au}})$. A 915 nm 10 μs laser pulse for 0 nm of gold is modeled in Figure 38, and 2, 5, 10, 30, 50 nm gold thicknesses are modeled in Figure 39. Material parameters are shown in the Table 6 below. The finite element model predicts that the pillar temperature quickly drops below deposition temperature due to high gold reflectivity, but experimentally the deposition process proceeds, indicating that the gold properties differ from bulk values.

Table 6. Simulation parameters used for finite element modeling methods comparison

PtCx Optical n	1.87
PtCx Optical k	0.31
PtCx Density	1250 $\frac{kg}{m^3}$
PtCx Thermal k	1 $\frac{W}{m*K}$
PtCx Specific Heat	700 $\frac{J}{kg*K}$
Au Optical n[201]	0.22
Au Optical k[201]	6.17
Au Density	19300 $\frac{kg}{m^3}$
Au Specific Heat	128 $\frac{J}{kg*K}$

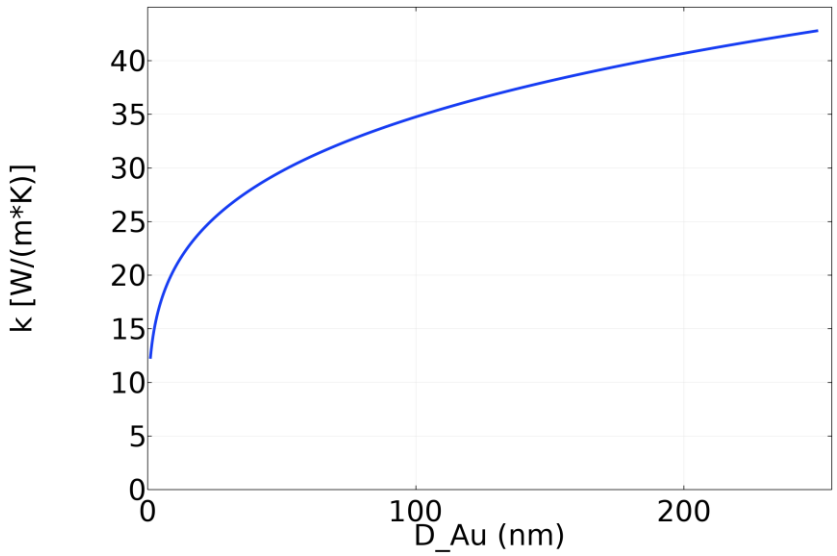

Figure 37. The fitted thickness dependent thermal conductivity for thin Au films, from 1-250 nm.

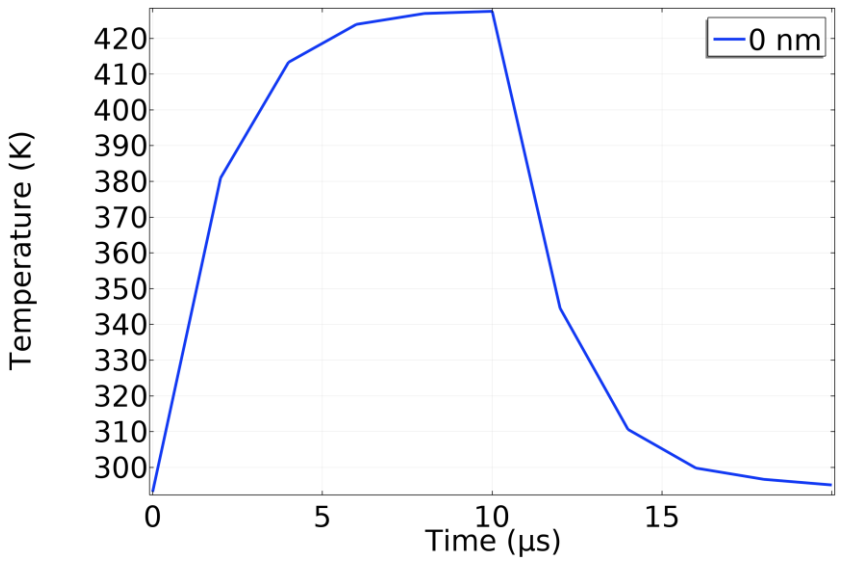

Figure 38. A time-temperature plot using the bilayer model with a gold thickness of 0 nm. Note that the maximum temperature here is slightly lower than is reported in maintext Figure 31, which is attributed to the usage of the simpler heat-dump model for the bilayer here vs. the radiative beam model used in maintext Figure 31 due to the heat module's better compatibility with multiple layers.

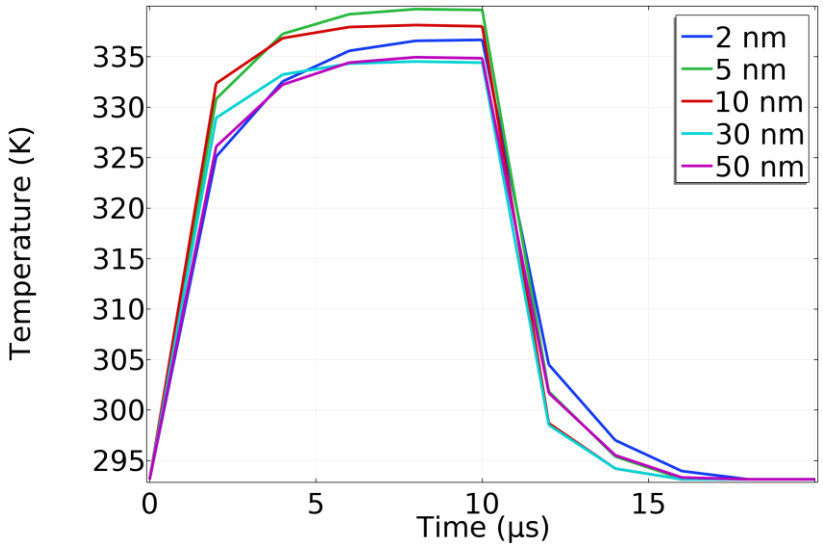

Figure 39. A time-temperature plot using the bilayer model with 2, 5, 10, 30, 50 nm gold. A large drop in temperature is predicted which suggests the deposition would be halted soon after the gold incubation. Experimentally we do not observe this, thus we attribute the enhanced absorption to the film roughness.

SI-4 Figure 3 Full EDX Maps

The full EDX maps of relevant species of the prepared sample in Figure 32. EDX maps of C (Figure 40) and Si (Figure 41).

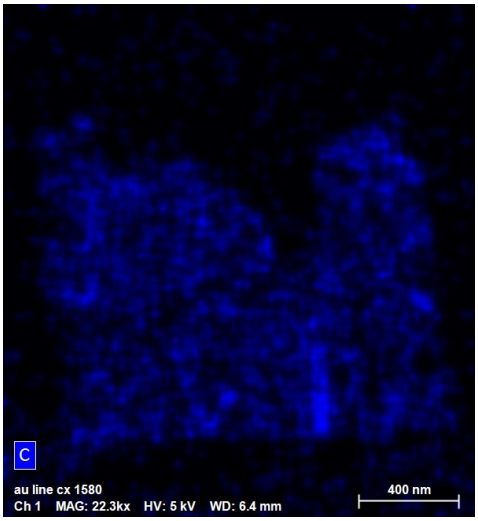

Figure 40. An EDX map showing carbon concentration, with the cross-sectioned core FEBID pillar clearly visible in the bottom right.

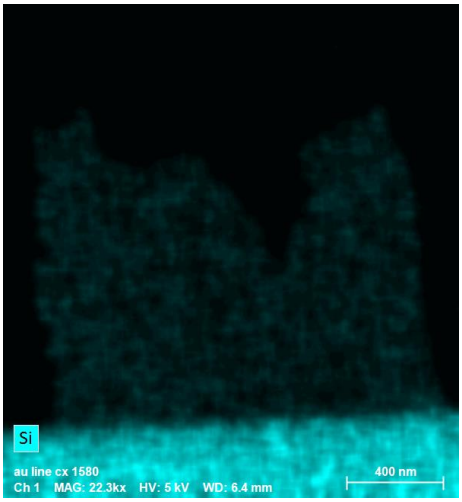

Figure 41. An EDX map showing silicon concentration, with the substrate showing high concentration and trace amounts on the pillar wall, likely from FIB cross-section re-deposition and beam scattering and interacting with the substrate.

SI-5 CNF Finite-Element Modeling Parameters

Carbon nanofibers were modeled as cones with experimentally determined height, base and tip widths using COMSOL's radiative beam in absorbing materials and heat transfer in solids as previously described. A single tip was used for modeling, but experimental geometries often have complex multi-tips. Graphite optical parameters used at 915 nm were an index of refraction of n=2.2, and an extinction coefficient of k=1.3. The nanopillar thermal parameters were a specific heat (C_p) of 1000 $\frac{J}{kg*K}$, a density (ρ) of 2200 $\frac{kg}{m^3}$, and a thermal conductivity (k) tuned to 190 $\frac{W}{m*K}$. Figure 42 shows a tuning plot of the temperature versus time for various CNF thermal conductivity values at the initial deposition power of 1.1 W (140 MW/m^2), where the lowest power onset depth is tracked (11um). Figure 43 shows the nanofiber temperature distributions without highlighting of the deposition temperature. Figure 44 is a continuous wave modeled heat profile of the 548 MW/m^2 0.3 s on-time exposure in maintext Figure 35, where the substrate itself can reach deposition temperature from CW exposures.

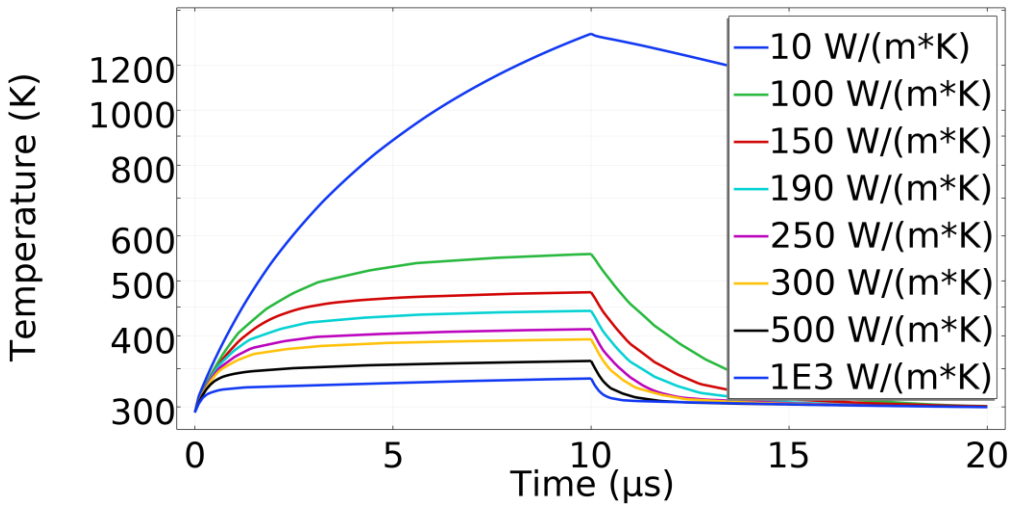

Figure 42. CNF thermal conductivity tuning, showing the temperature evolution over time at a given thermal conductivity value.

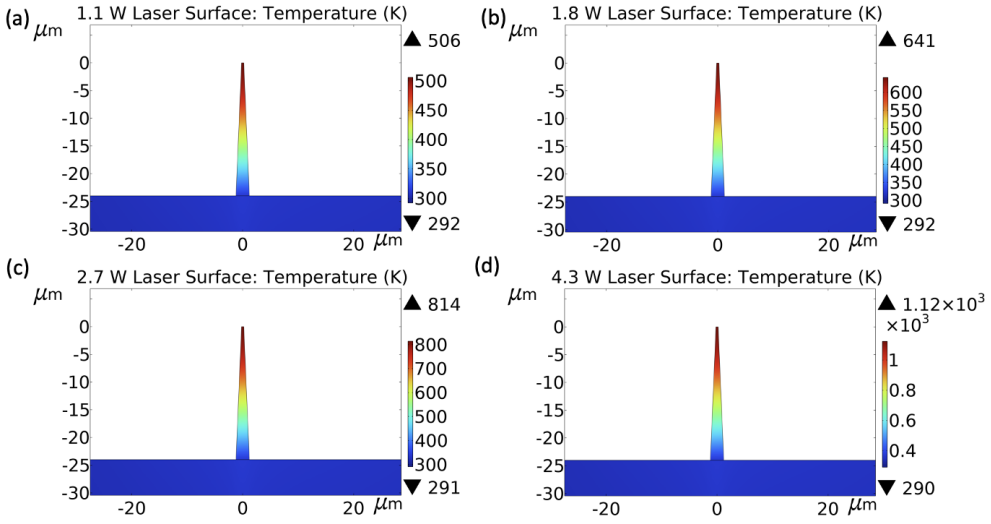

Figure 43. Carbon nanofiber temperature profiles for various experimental powers of (a) 1.1 W, (b) 1.8 W, (c) 2.7 W, (d) 4.3 W, where the color scale bar is based on the peak temperature at the end of the laser pulse width.

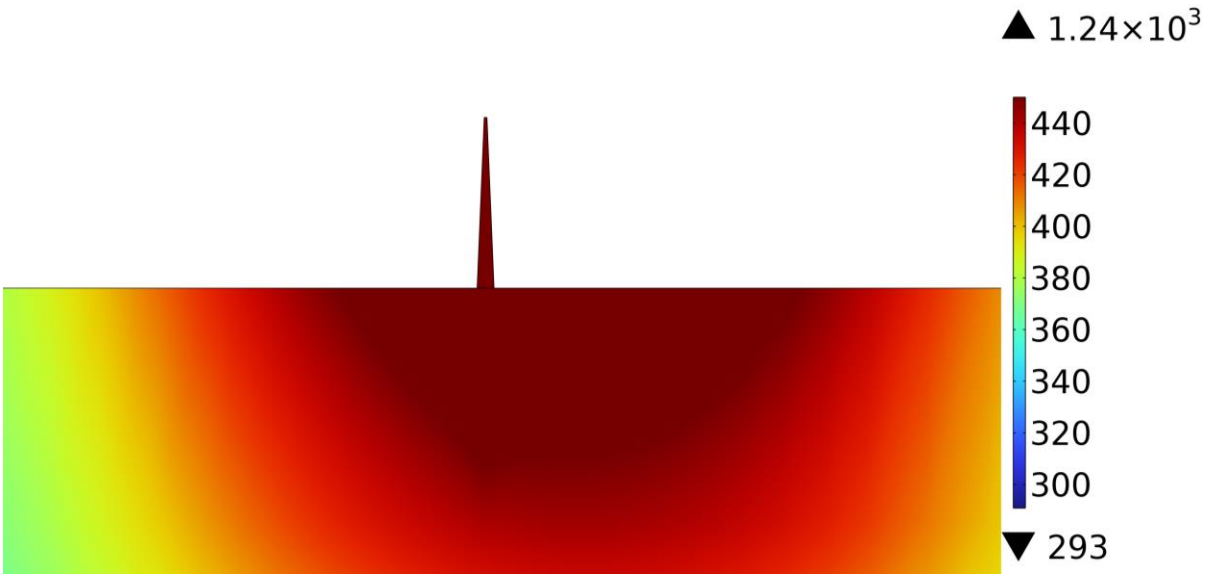

Figure 44. Modeled carbon nanofiber temperature profile of a 300 ms continuous-wave exposure, instead of the pulsed experiment and model in the maintext.

CHAPTER III

Selected Area Manipulation of MoS_2 via Focused Electron Beam Induced Etching for Nanoscale Device Editing

John Lasseter[1], Spencer Gellerup[1], Sujoy Ghosh[2], *Seok Joon* Yun[3], Rama Vasudevan[2], Raymond R. Unocic[2], Olugbenga Olunloyo[4], Scott T. Retterer[2], Kai Xiao[2], Steven J. Randolph[2,*], Philip D. Rack[1,*]

1. Department of Materials Science and Engineering, University of Tennessee, Knoxville, Tennessee 37996, United States

2. Center for Nanophase Materials Sciences, Oak Ridge National Laboratory, Oak Ridge, Tennessee 37831, United States

3. Department of Semiconductor, University of Ulsan, Ulsan, 44610, Republic of Korea

4. Department of Physics and Astronomy, University of Tennessee, Knoxville, Tennessee 37996, United States

[*]Corresponding author email: prack@utk.edu, randolphsj@ornl.gov

Author Contributions

Reprinted with permission from ACS Appl. Mater. Interfaces 2024, 16, 7, 9144–9154. John Lasseter performed the focused electron beam induced etching, SEM and AFM imaging. Seok Joon Yun synthesized the monolayer CVD samples, and Olugbenga Olunloyo helped prepare the monolayer STEM samples. Raman and photoluminescence spectroscopy was measured by Spencer Gellerup. Device synthesis and electronic measurements were taken by Sujoy Ghosh and John Lasseter. STEM imaging was done

by Raymond Unocic with guidance from John Lasseter, and STEM image segmentation was performed by Rama Vasudevan. John Lasseter wrote the first draft of the paper and Philip D. Rack and Steven Randolph assisted in revising the draft. All authors reviewed the manuscript. Philip D. Rack and Steven Randolph conceptualized the experimental plan.

Abstract

We demonstrate direct-write patterning of single and multi-layer MoS_2 via a focused electron-beam induced etching (FEBIE) process mediated with the XeF_2 precursor. MoS_2 etching is performed at various currents, areal doses, and on different substrates and characterized using scanning electron and atomic force microscopies, as well as Raman and Photoluminescence spectroscopy. Scanning transmission electron microscopy reveals a sub 40 nm etching resolution and the progression of point defects and lateral etching of the consequent unsaturated bonds. The results confirm that the electron beam induced etching process is minimally invasive to the underlying material in comparison to ion beam techniques, which damages the sub-surface material. Single layer MoS_2 field effect transistors are fabricated and device characteristics are compared for channels that are edited–via the selected area etching process. The source-drain current at constant gate and source-drain voltage scale linearly with the edited channel width. Moreover, the mobility of the narrowest channel width decreases, suggestive that backscattered and secondary electrons collaterally affect the periphery of the removed area. Focused electron beam doses on single layer transistors below the etching threshold were also explored as a means to modify/thin the channel layer. The FEBIE exposures showed demonstrative effects via the transistor transfer characteristics, photoluminescence and Raman spectroscopy. While strategies to minimize backscattered and secondary electron interactions outside of the scanned regions

require further investigation, here we show that FEBIE is a viable approach for selective nanoscale editing of MoS_2 devices.

Keywords: Nanofabrication, Two dimensional materials, Direct write, Electron beam-induced etching, patterning

Introduction

Two-dimensional transition metal dichalcogenides (TMDs) have intriguing optoelectronic properties and thus are actively researched for their potential in next-generation devices[203–207]. To advance the state of the art in layered TMD materials, advanced synthesis and fabrication methods are being developed to controllably grow high quality and large area TMD's[208,209], stack single layers to make hybrid 3D devices[210,211], and etch with high selectivity and atomic layer control[212,213]. Recently resist-less fabrication has been explored to improve device performance, including direct[214] and indirect[215] patterning of MoS_2 with ice assisted electron-beam lithography, μm-resolution wafer-scale scratching lithography on MoS_2 [216], and scanning probe electrochemical etching methods[217]. Furthermore, many advanced functionalization methods have been developed: covalent patterning of 2D MoS_2[218], light-modulated charge density control of MoS_2 superlattices[219], and MoS_2 biosensors[220] to highlight a few.

While wafer-scale processes with nanometer resolution are ultimately needed for chip manufacturing, selected area nanoscale processing methods are convenient to rapidly prototype different device architectures and selectively tune device structure. To this end, various photon[221], ion[222,223] and electron beam[211] induced processes have been developed to edit devices at the micro- and nanoscale. Both additive and subtractive techniques exist. These processes typically involve

a vapor or gas phase precursor assist. For selective deposition, a precursor is injected that undergoes a photon, electron or ion beam induced reaction resulting in decomposition on the substrate. In selective etching processes, the photon, electron or ion beam induces a reaction whereby the byproducts react with the substrate and form a new volatile byproduct, which subsequently desorbs from the surface.

Focused ion beam (FIB) processing is probably the most ubiquitous direct-write technique for selected area nanoscale material removal including gas-assisted processes to accelerate etching[224–228], and, more commonly, physical sputter removal. While this method is efficient in removing material in the micro- to nano-scale, the energetic ions can damage the sub-surface material. In the past decade, the He^+ gas field ion microscope (HIM) was commercialized as a higher resolution variant to the more common Ga^+ liquid metal ion source based FIB. Helium has a much lower mass and thus lower nuclear stopping power, so gas-assisted processes are critical to balance sufficient material removal and sub-surface damage accumulation[229,230]. Focused helium ion beam modification of multilayer and single layer WSe_2 revealed the ability to selectively tune the transport properties via preferential chalcogen sputtering.[225] A comparison of direct helium sputtering and XeF_2 chemically assisted etching of WSe_2 revealed enhanced etching and less damage associated with the chemical assist, but a damage region extending laterally 120 nm was still observed.

Focused electron beam induced etching (FEBIE) in a scanning electron microscope (SEM) is at the other end of the spectrum relative to Ga^+ beams[224,231–234]. The electron mass at tens of keV energy is insufficient for knock-on sputtering, thus requiring gas mediation to induce reasonable etching beyond electron stimulated desorption processes. Consequently, electron beam

induced etching is typically characterized by lower etching rates (compared to FIB), but a key advantage is reduced sub-surface and peripheral damage that primary and recoiled ions may produce. The prominent commercial application that has emerged for focused electron beam induced processing is lithography mask repair[45,235,236], as ion beam damage during the nanoscale editing deleteriously affects the very stringent optical properties. To accelerate the electron beam etching rate (and purify electron beam induced deposits[141]) a pulsed photon beam assisted process has been developed where an intermittent photon beam locally heats the substrate to facilitate the electron stimulated reaction and stimulates byproduct desorption which can rate limit the process[237]. Regarding transition metal dichalcogenide materials, recently Granados et al[238], demonstrated direct electron beam induced nanopatterning of MoS_2 utilizing an XeF_2 precursor. While the specific etch rate is not reported, device editing was demonstrated and a peculiar shift in the n-type conduction was observed. Figure 45 Provides a representative schematic of the gas-assisted electron-beam induced etching process.

Spontaneous XeF_2 vapor etching of 2D TMD's has also been explored for layer thinning[239] and device fabrication when combined with nanolithography[240,241]. Conveniently, graphene is not spontaneously etched in XeF_2, so it is an adequate etch stop for MoS_2. Interestingly, fluorination of graphene causes sp^3 type defects as evidenced in the Raman D peak increase, which reduces the conductivity, whereas fully fluorine-passivated graphene is insulating[241,242].

Here we systematically explore FEBIE of MoS_2 mediated by an XeF_2 precursor. As our local pressures are much lower than previous spontaneous etching studies, negligible spontaneous etching is observed in what is presented and we attribute the etching to synergistic electron-XeF_2 precursor interactions with the MoS_2. Initial studies are performed on exfoliated multilayer MoS_2

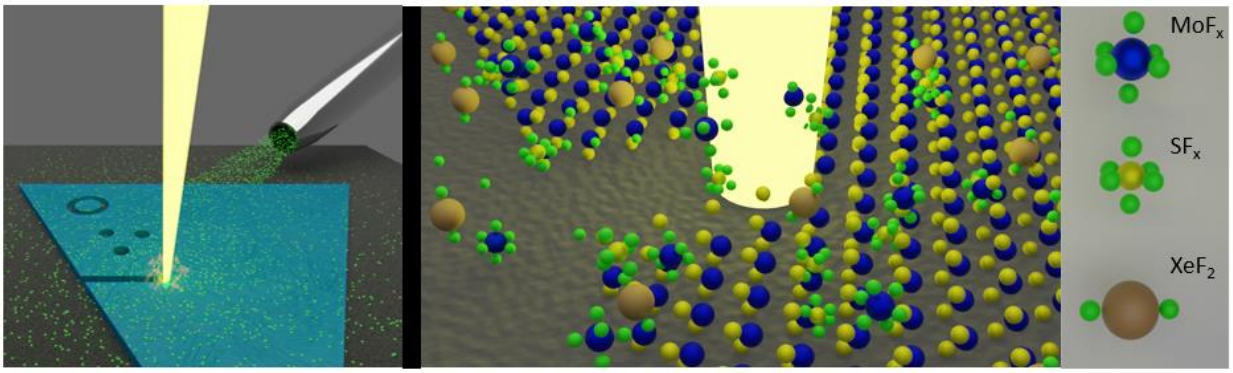

Figure 45. Schematic illustrating the focused electron beam induced etching process, where the electron beam forms volatile and reactive fluorine species from the XeF_2 precursor gas that cause the etching of the exposed material.

to establish the etching rate. Both gold and SiO_2 substrates are examined, and we subsequently investigate chemical vapor deposition (CVD) grown monolayer etching on gold and correlate the results with atomic force microscopy (AFM), Raman and photoluminescence (PL) spectroscopy. Additionally, we investigate the etching evolution via atomic resolution scanning transmission electron microscopy (STEM). Single layer MoS_2 field effect transistors are edited with the process to demonstrate the efficacy of controllably tuning the channel layer dimensions "on-demand" and to correlate the electrical properties to the measured optical and vibrational characteristics. Finally, single layer MoS_2 devices are exposed to electron beam induced etching areal doses well below the dose required to fully etch through the flake and the subsequent electrical, vibrational and optical characteristics are explored to help elucidate the FEBIE evolution.

Results and Discussion

Figure 46 illustrates a) optical and b) electron micrograph of an ~12 nm thick (~ 18 layers) exfoliated flake on a gold substrate that was etched via FEBIE with 1x1 mm boxes at various areal doses using a beam current of 0.4 nA. Figure 46 c) is a plot of the etch depth versus areal dose as determined via AFM (see SI-1 For 1.6 nA data). Initial tests were performed on SiO_2 substrates, however SiO_2 also etches via FEBIE in XeF_2 [224], which can make data interpretation difficult. Evidence suggested that the FEBIE generates a porous structure, which enables XeF_2 permeation and etching of the underlying SiO_2 (see SI-2). Gold, on the other hand, is not susceptible to the XeF_2 FEBIE, and thus a robust etch stop layer for the MoS_2. The results show that the etch efficiency is almost 2x higher at the higher current. This is inconsistent with many electron and ion beam induced deposition and etching processes, which decrease efficiency with increasing current due to precursor depletion which effectively leads to a more mass transport limited regime.

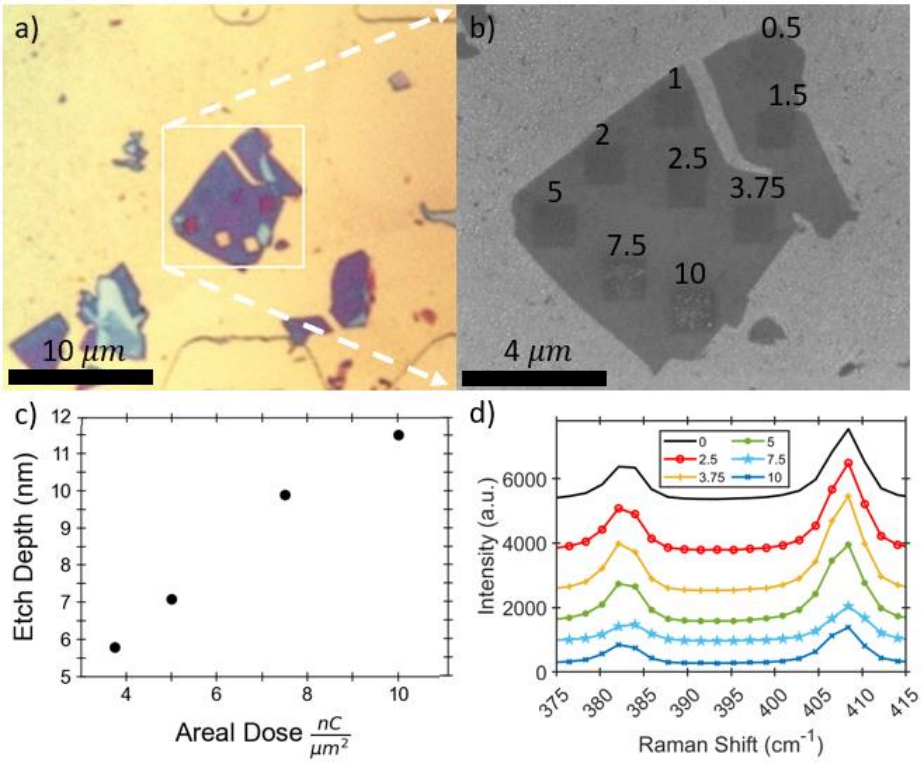

Figure 46. a) Optical and b) secondary electron images of an exfoliated flake, on a gold thin film etched with a 0.4 nA beam current; labels in b) are area doses in $\frac{nC}{\mu m^2}$. c) Plot of the etch depth versus areal dose of the etched boxes of the 4 highest doses shown in a) and b). d) A plot of the Raman spectra of the A_{1g} and E^1_{2g} peaks measured for various FEBIE areal doses. See SI-3 for a corresponding plot of the LA(M) mode.

Synergistic effects could be operable at higher current such as low volatility byproducts that are facilitated by an electron stimulated desorption process. While we attempt to position our gas injection system nozzle at the same position, we cannot rule out that this effect is due to variations in the gas injector positioning, which can easily increase the gas flux due to the sensitive nature of the GIS nozzle position on the etch rate[243,244].

To estimate the approximate regime, Table 7 lists the estimated XeF_2 flux[225], which results in a monolayer coverage time of ~8.4 ms (assuming a sticking coefficient of 1). This is much longer than the pixel dwell time, thus little gas is adsorbed during each 5 ms pixel exposure. Table 7 also illustrates the calculated areal electron dose per pixel dwell, the areal density of MoS_2, the ratio of the electron areal dose per pixel and the MoS_2 areal density, and the estimated experimental MoS_2 etch efficiency. The line and frame loop times are 250 ms and 12.5 ms, respectively, thus the MoS_2 is likely fully covered with XeF_2 after each full frame, but partial depletion could occur from the previous neighboring line scan. The data suggests that at 0.4 nA ~ 0.009-0.013 of a monolayer is etched per pass and at 1.6 nA ~ 0.08-0.09 of a mono layer is etched per pass. For comparison, at 0.4 nA this equates to a volumetric etch efficiency for MoS_2 between 1.9-2.6 x10^{-4} $\frac{nm^3}{e^-}$ and 4.2-4.6 x10^{-4} $\frac{nm^3}{e^-}$ at 1.6 nA. For comparison the WSe_2 He^+ etch efficiency mediated by XeF_2 was estimated 8.3x10^{-3} $\frac{nm^3}{He^+}$ [225].

While the specific etching by-products are not discernible via mass spectrometry due to the extremely small etch volumes, the simplest electron stimulated dissociation and subsequent reactions with Mo and S can be given by:

$$XeF_2 + e^- \rightarrow Xe + 2F + e^-$$

Table 7. Summary of the calculated etching parameters and etch efficiency.

	XeF_2 Flux ($\frac{XeF_2}{nm^2 s}$)	Areal dose per dwell ($\frac{e^-}{nm^2}$)	Areal density of MoS_2 ($\frac{MoS_2}{nm^2}$)	Electron areal dose/MoS_2 areal density ($\frac{e^-}{MoS_2}$)	MoS_2 etch efficiency ($\frac{nm^3}{e^-}$)
MoS_2 on Au 0.4 nA	$1.6x10^3$	31	14.8	2.1	$1.9\text{-}2.6\ x10^{-4}$
MoS_2 on Au 1.6 nA	$1.6x10^3$	125	14.8	8.4	$4.2\text{-}4.6\ x10^{-4}$
CVD single layer MoS2 on Au, 1.6 nA	$1.6x10^3$	125	14.8	8.4	$4.5\text{-}5.8\ x10^{-5}$ *ignoring anamolously low peak

$$xF + S \rightarrow SF_x$$

$$xF + Mo \rightarrow MoF_x$$

While x<6 products are possible, particularly if accompanied by an electron stimulated desorption mechanism, MoF_6 and SF_6 are both stable gases with high room temperature vapor pressures and MoF_6 has the highest vapor pressure of the MoF_x variants[245]. Patrito et al.[246] recently performed ab-initio molecular dynamics simulations on spontaneous reactions between MoS_2 and F_2 and reported a multi-step process beginning with adsorptive fluorination and volatilization of SF_3. Electron beam exposure of MoS_2 for instance has been shown to facilitate defect formation, which when annealed leads to oxidation and pore formation[247]. Previous work by Drndic *et al*[248] , also showed that 200 keV electron beam with a dose range of 1.6 – 8x10^2 ($\frac{nC}{\mu m^2}$) leads to sulfur monovacancy formation in MoS_2. Figure 46 d) is a plot of the averaged Raman spectrum taken from each exposure dose in Figure 46 a) and b). Interestingly, the Raman spectra does not change dramatically except that the absolute intensity of the E^1_{2g} and A_{1g} peaks decrease for the highest areal doses, consistent with the images illustrating nearly complete etching of the material. The LA(M) peak (see SI-3) remains in the noise, which is substantially different from He^+ exposures of WSe_2. He^+ doses as low as 1.6x10^{-3} $\frac{nC}{\mu m^2}$showed a dramatic increase in the LAM peak due to significant defect generation from the ion beam[249]. This suggests that the electron beam etching process is a "soft" process that minimally damages the underlying material during the etching process.

After the multilayer etching test, we also investigated etching of single layer CVD grown MoS_2. As described in the methods section, the CVD process utilizes a salt precursor and the

transfer process to the gold-coated substrate utilizes a polycarbonate layer. Thus, while the expected MoS_2 thickness should be 0.65 nm, the approximate single layer thickness was measured by AFM is ~2 nm due to the surface roughness of the underlying sputtered gold film (~root mean square roughness of 1.2 nm), residual salt precursor from the CVD growth, and/or polycarbonate transfer contamination. Figure 47 a) is a SEM image of the single layer with 2x2 mm etch boxes etched to various FEBIE doses, and as the image contrasts suggests, the etch appears to be completely through the flake at an areal dose of ~3.5 $\frac{nC}{\mu m^2}$ (see supporting information SI-4 for complementary AFM data). The complementary Raman spectra and A_{1g} intensity map in Figure 47 b), c), respectively, confirms that A_{1g} and E^1_{2g} peaks basically vanish at the 3.5 $\frac{nC}{\mu m^2}$ dose, which is more than an order of magnitude larger than the extrapolated 1.6 nA multilayer dose for a single layer etch depth (0.23 $\frac{nC}{\mu m^2}$). We attribute the difference to the transfer contamination and residual salt from the CVD process; namely the salt and polycarbonate contamination have much lower FEBIE rates with the XeF_2 chemistry. The Raman results show a systematic decrease in the intensity, consistent with the etching process resulting in less material being probed due to decreasing thickness through material loss. A slight increase in the LA(M) mode (see SI-3) is observed in the single layer etching at ~ 2 $\frac{nC}{\mu m^2}$, which we attribute to the growing pores and increased number of defects at pore perimeters as discussed below. In Figure 47 d), the photoluminescence is more sensitive to the electron beam induced etching process where the PL is shown to be quenched at the lowest areal dose of 1 $\frac{nC}{\mu m^2}$. The decrease in PL is attributed to mid-gap states generated in the MoS_2 that lead to competitive non-radiative decay pathways.

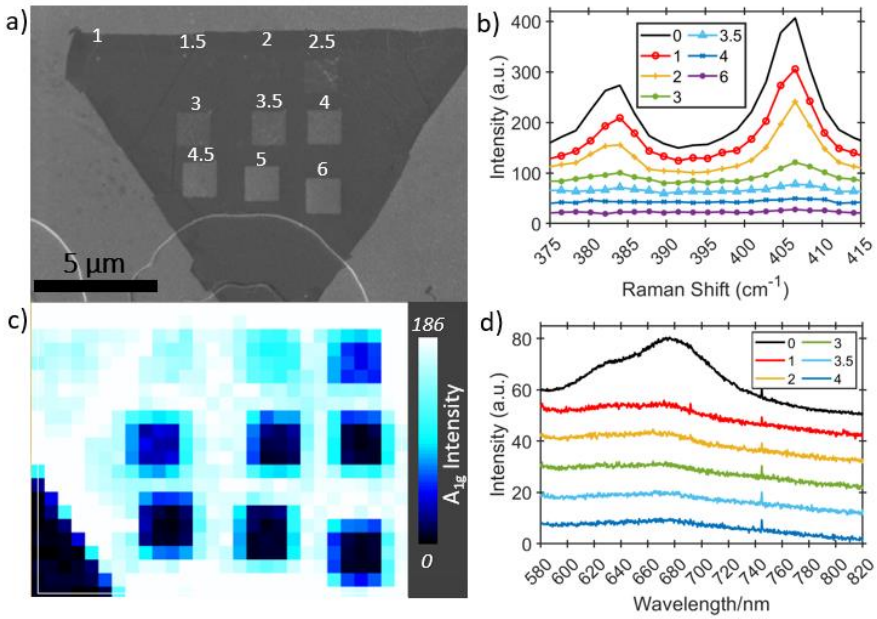

Figure 47. a) Secondary electron image of a monolayer flake etched with the 10 different doses specified by the labels (all dose units are $\frac{nC}{\mu m^2}$). b) Raman spectra and c) A_{1g} intensity map at different FEBIE doses. d) Photoluminescence spectra of the etched monolayer flake at different FEBIE doses, showing the sensitivity of photoluminescence to the etching process.

To better understand the progression of the single layer etching, MoS_2 single layers were transferred onto holey membranes and exposed to a series of lineal and areal exposure doses then imaged using an aberration corrected STEM. Figure 48 shows medium angle annular dark field (MAADF) STEM images for a series of line doses (0.32-0.8 $\frac{nC}{\mu m}$) that were exposed and illustrates ~40 nm linewidth is obtained as the dose approaches the dose required to through-etch.

Figure 49 is a collage of areal exposures and it is important to note that the etch rate for the suspended single layers appears to be slower than on the gold (and SiO_2) substrate. We attribute the significantly lower etch rate to the reduced electron interaction volume of the suspended single layer MoS_2, which reduces the secondary electron yield, which has been shown to be important to the deposition yield in focused electron beam induced deposition[11]. The larger field of view images reveal the progression of the of the porous network, where small few-nm holes emerge at 4 $\frac{nC}{\mu m^2}$ and larger ~10 nm holes are evident at 8 $\frac{nC}{\mu m^2}$ The high-resolution image series in Figure 49 i-l) confirms the soft, chemical nature of the electron beam induced etching process as the un-etched material quality remains high. Analysis of a series of 8x8 nm field of view images reveal the evolution of the defect density in the MoS_2. In Figure 50, we quantify the degree of defects induced by the radiation to the MoS_2 by an inverse Fourier method, first described by Lin, *et. al.*[250]. The workflow is shown in Figure 50 a). A 2D fast Fourier Transform (FFT) is applied (inset) to an unexposed MoS_2 image, and the peaks corresponding to the atomic lattice are masked for retention; the rest of the FFT image is nullified. The inverse Fourier transform recovers a 'clean' image, i.e. one where the lattice is reconstructed on the basis of the chosen peaks. With this Fourier filtered

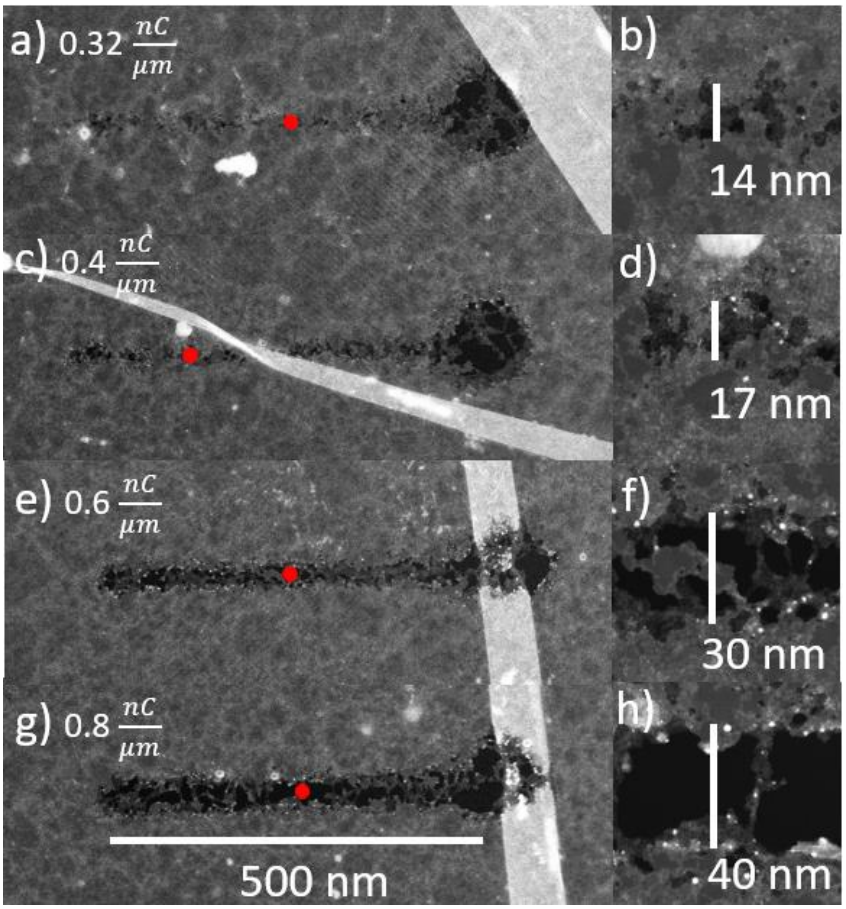

Figure 48. MAADF-STEM images of etched lines at various electron-beam line doses, where each row has a lower magnification view of the line and a higher magnification to estimate the linewidth; the high magnification image position noted by the red dot. Note the beam park position patterning artifact to the right of the line pattern. The line doses are a-b) 0.32, c-d) 0.4, e-f) 0.6 and g-h) 0.8 $\frac{nC}{\mu m}$.

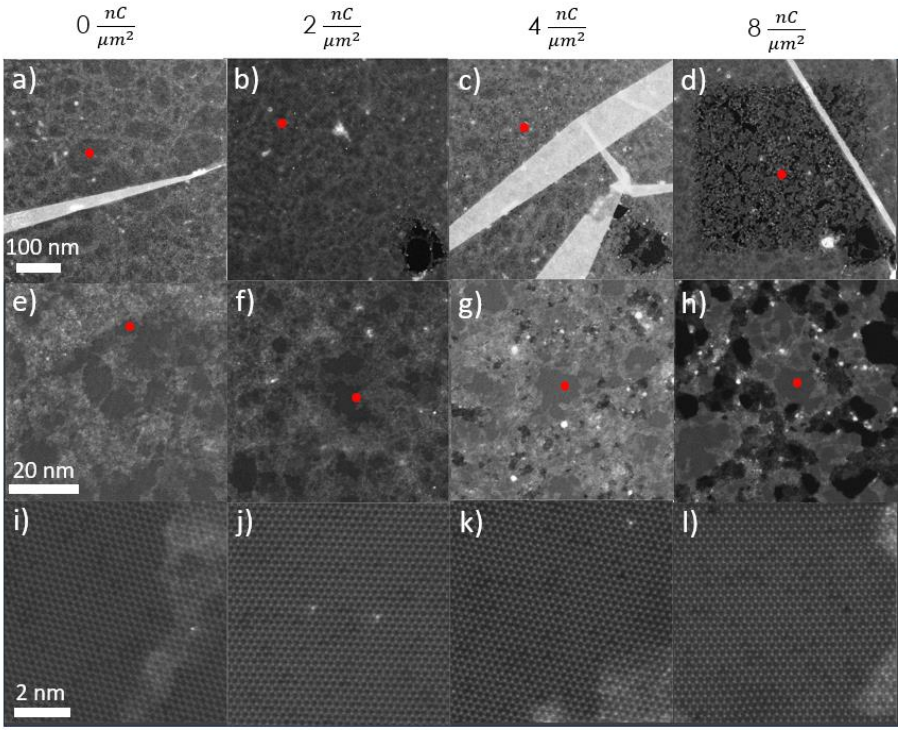

Figure 49. MAADF-STEM Images of etched regions at progressing electron-beam doses. Note the beam park position patterning artifact at the bottom right of exposed 500x500 nm regions. The field of views for each row is a-d) 512x512, e-h) 64x64, and i-l) 8x8 nm. The red dots in the images correspond to the location of the image in the subsequently smaller field of view e) and i), respectively, for each dose.

image, we then calculate the difference map between this image and the original STEM images taken for various FEBIE exposure doses. For a perfect lattice with no defects, the difference image should be close to zero. For defects that break the periodicity, these will appear as characteristic spots within the difference image. Note that contamination can also appear in the difference image. We then used a segmentation method, specifically using the Ilastik software[251], to train a segmentation model based on manual labeling of the defects in the difference image. The result of the segmentation model is shown in the last image, and for each of the STEM images in Figure 50 b). Note that we only consider the central portion of the image (about 60%) and neglect the edges/border as we found that the difference images can also show slight variations based on scan distortions and other artifacts that make segmentation more challenging. Full images are provided in the supporting information (SI-5). The areal fraction of the defects is shown in c) and clearly indicates the growing defect percentage with the increased irradiation. Thus, we hypothesize that atomic scale defects form and preferentially grow/coarsen as these defect sites have unsaturated bonds and are thus more reactive to fluorine radicals. This mechanism is consistent with spontaneous XeF_2 etching of MoS_2, where lateral growth at defect regions patterned by dry etching produced periodic arrays of MoS_2 hexagons[239]. Note that the spontaneous etching in XeF_2 is performed at much higher pressures and longer times than in our experiments and that we do not observe spontaneous etching during the several to tens of minute exposures experienced in our FEBIE experiments. Thus, we again note that the etching here is realized via synergetic e-beam/XeF_2 interactions consistent with FEBIE.

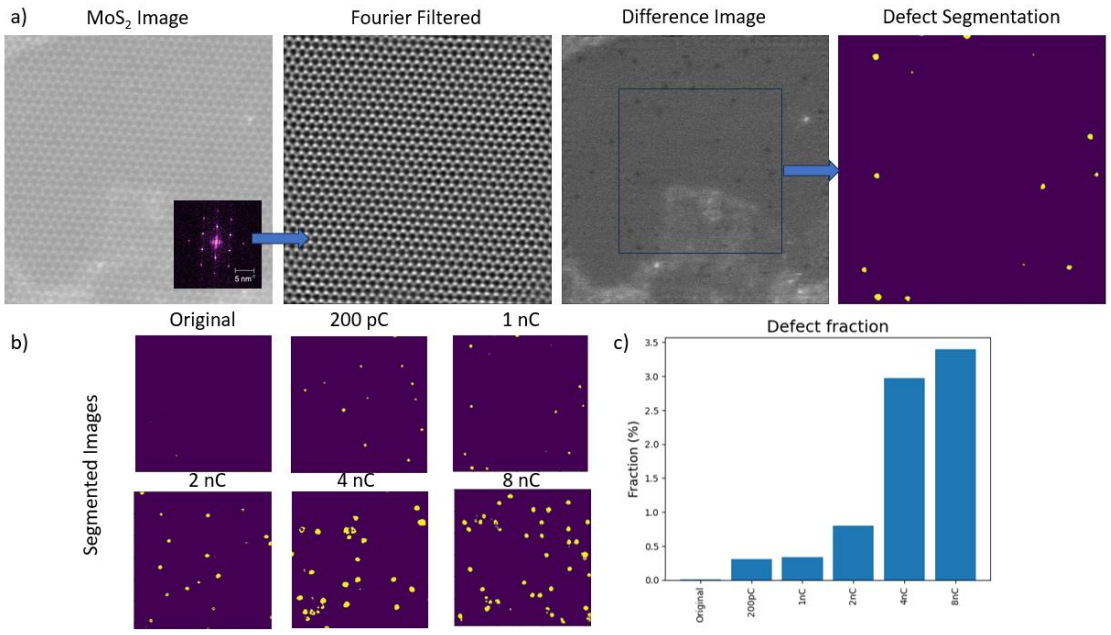

Figure 50. Defect quantification workflow. a) The STEM image is first Fourier Filtered (2D FFT is inset), and the filtered image is subtracted from the original image to yield the difference image. This difference image clearly highlights regions where the periodicity is broken by the presence of point defects. A segmentation model is used to semantically segment the defects. To avoid artifacts such as scan distortions which are more prevalent towards the edges, only the central portion of the image (blue square in the difference image) is used for this task. b) Semantically segmented difference images. c) The defect fractions from b) as a function of the radiation dose.

To test the efficacy of editing functional devices, we fabricated and tested a series of MoS_2 single layer field effect transistors. Figure 51 shows optical and scanning electron images a,b) before and c,d) after the channel layers were etched to narrow the channel. Figure 51 e) shows the transfer characteristics at 1 V_{SD} for each device with the as-fabricated and FEBIE etched channels shown. Figure 51 also shows device f) mobility, g) threshold voltage, h) subthreshold swing, and i) the on-current at 1 V_{SD} versus etched channel widths (note the before channel widths are listed in Figure 51e)). Not surprisingly, the device characteristics for the wider channels are not significantly affected except that the threshold voltage for the widest etched channel had the largest shift in the threshold voltage to a more negative value. The 0.5 and 1 mm channel layers show a decrease in mobility and the 0.5 mm device had an increase in the subthreshold swing and the only positive shift in the threshold voltage. This is likely due to backscattered electrons and their associated secondary electrons (type II -- SE_{II}) that contribute at these lateral dimensions. Future studies will explore the effect of beam energy on the peripheral damage as interesting and competing effects will occur at lower and higher beam energy: namely at lower beam energy the lateral extent of the backscattered and SE_{II} will decrease, however their areal intensity will increase, while the lateral extent of the backscattered and SE_{II} will increase at higher energy though their areal intensity will decrease. As illustrated in the insets in Figure 51 c),d) the Raman and photoluminescence spectroscopy maps of the channel layers are minimally affected by the FEBIE process and interestingly the PL intensity of the 500 nm and 1 mm channels nearly doubles relative to the original and other channel regions. This cause of the increased PL will be studied in the future, but is likely correlated to the backscattered/SE_{II} beam effects alluded to above (See SI-6 for Raman and PL spectra).

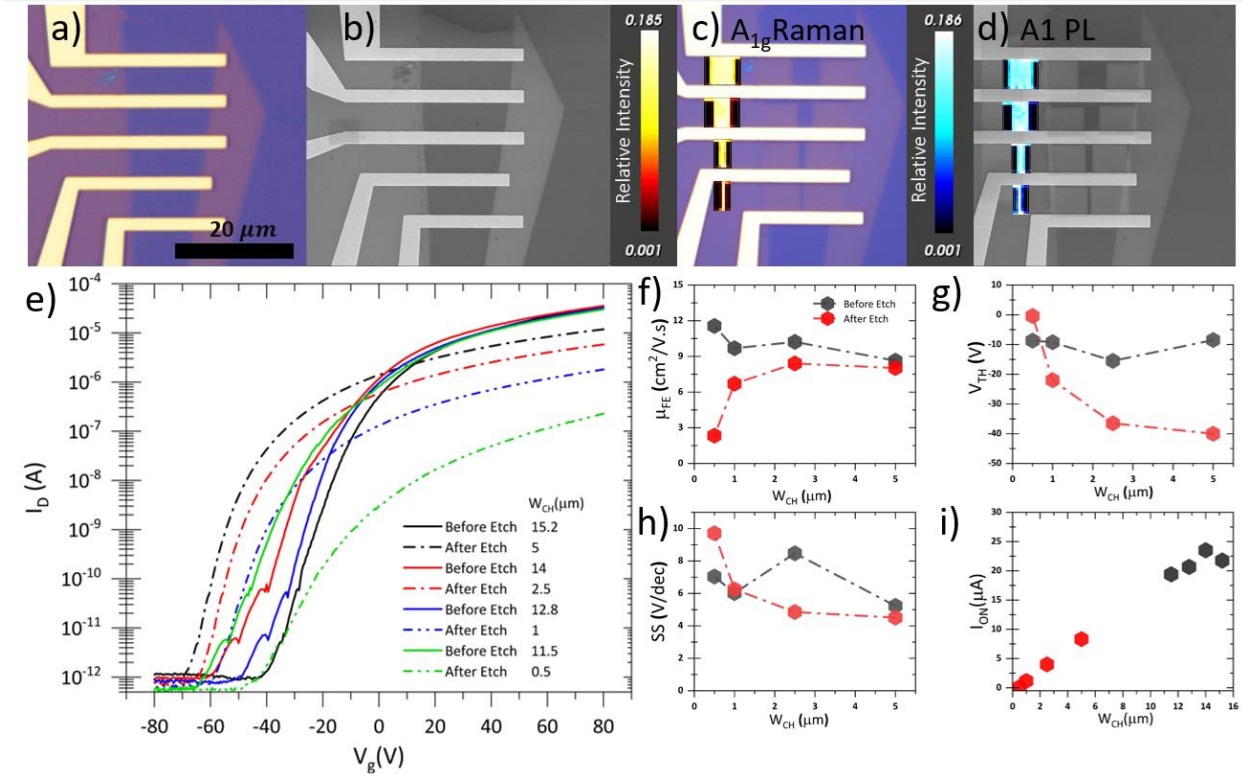

Figure 51. a,b) Before and c,d) after optical and SEM images of the etched nanoribbon devices with 5 μm channel length and variable width. The inset of c) shows the relative intensity of the A_{1g} Raman spectroscopy maps (at 405 cm^{-1}) of the channels, and the inset of d) shows the relative photoluminescence intensity of the A1 exiton mode (at 675 nm) of the edited channels. e) Is the transfer characteristics at 1 V_{SD}, before and after etching with the channel dimensions noted in the legend. f) Shows the electron mobility, g) the threshold voltage, h) the subthreshold swing and i) the drain current at V_G = 60 V all versus the channel width. Note that the before etch curves in f-i) have channel widths noted in e).

Finally, we also explored the effect that sub-monolayer MoS_2 etching has on single layer FET channels. In this case, a set of FET devices were fabricated, measured, and subsequently the full MoS_2 channel areas were exposed to areal doses ranging from $2x10^{-2}$-$5x10^{-1}$ $\frac{nC}{\mu m^2}$. Figure 52 shows a) optical and b) SEM images of the device after the FEBIE exposures and c) and d) show the resultant PL and Raman spectra, respectively. Figure 52 e) is a comparison of the as-fabricated and FEBIE exposed transfer characteristics (taken at 1 V V_{sd}), and f-h) show the summary of the before and after f) subthreshold swing, g) field effect mobility, and h) threshold voltage versus FEBIE dose. Note that one channel (3) was exposed twice; the initial channel exposure was $2x10^{-2}$ $\frac{nC}{\mu m^2}$. The electronic properties were measured, and the channel was then exposed to an additional dose of $8x10^{-2}$ $\frac{nC}{\mu m^2}$ (for a cumulative dose of $1x10^{-1}$ $\frac{nC}{\mu m^2}$) and measured again. Though trapped charge can be injected during the initial measurement, the second measurement was ~3 days after the initial measurement, thus we believe sufficient time transpired to minimize any trapped charge that could affect the second measurement. Raman and photoluminescence spectroscopy were then taken on the channels at doses of $1x10^{-1}$, $2x10^{-1}$, and $5x10^{-1}$ $\frac{nC}{\mu m^2}$.

At $2x10^{-2}$ $\frac{nC}{\mu m^2}$ the channel becomes more n-type, which is consistent with generating sulfur vacancies. Additionally, a higher subthreshold swing and mobility and a more negative threshold voltage are observed. At higher doses, $1x10^{-1}$ $\frac{nC}{\mu m^2}$ - $5x10^{-1}$ $\frac{nC}{\mu m^2}$, the I_{sd} decreases, which is consistent with the etch propagating and effectively reducing the area of the MoS_2 channel layer. There is a modest increase in the subthreshold swing, and progressively lower electron field effect mobility and positive shift in the threshold voltage. Figure 52 shows the progression of the

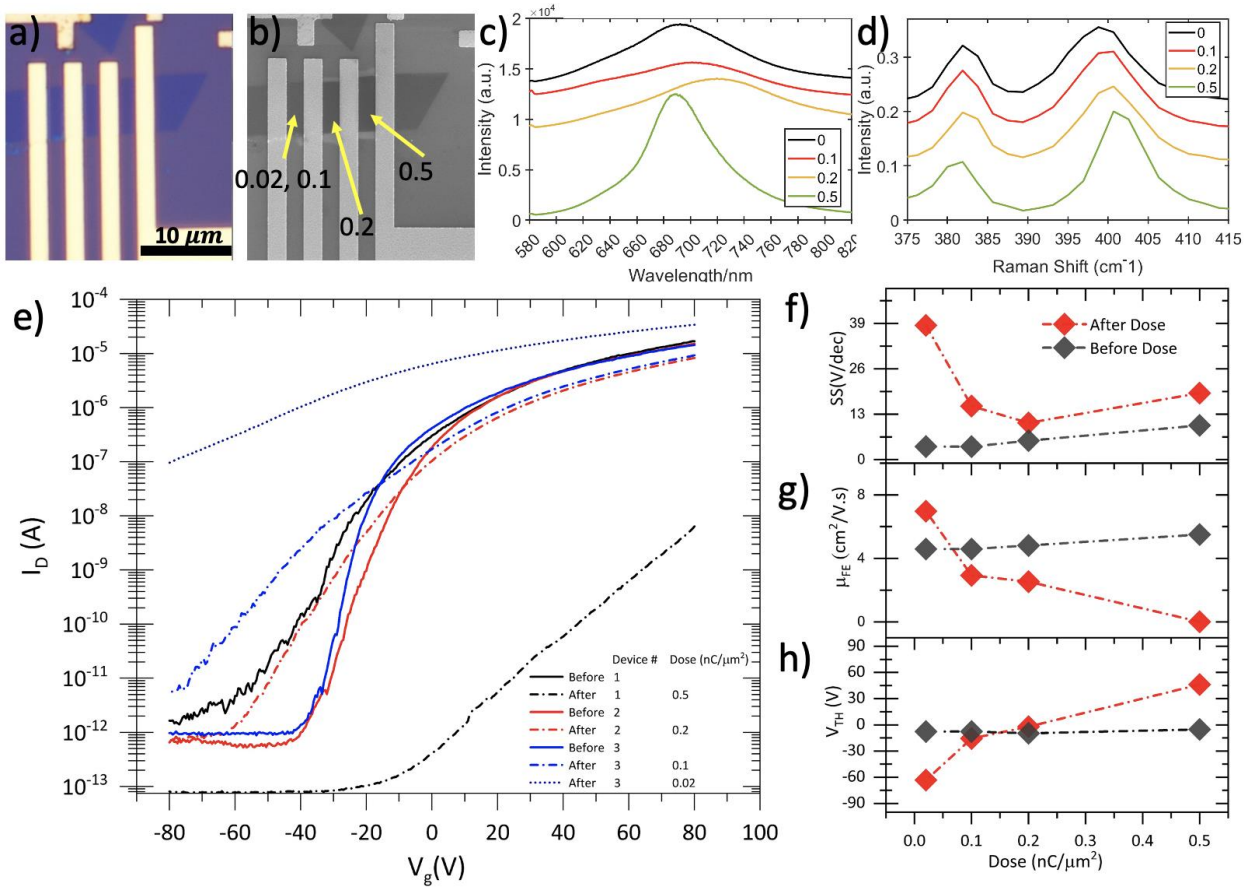

Figure 52. a) Optical and b) SEM images of the exposed 2 μm channels (areal doses are labeled and units are $\frac{nC}{\mu m^2}$. c) Photoluminescence and d) Raman spectra of the channel layers after the various FEBIE doses. e) Shows the transfer characteristics at $1V_{SD}$, before and after FEBIE exposures with the channel exposures noted in the legend. f) Shows the subthreshold swing g) the electron mobility, and h) the threshold voltage as a function of the FEBIE exposure dose. Note the before dose curves correspond to the channels that were exposed but were measured prior to the FEBIE so each has no exposure.

c) PL and d) Raman spectra of the exposed channels at $1x10^{-1}$ $\frac{nC}{\mu m^2}$ the PL peak initially red-shifts and at $5x10^{-1}$ $\frac{nC}{\mu m^2}$ the peak narrows and slightly blue shifts relative to the un-exposed regions (See SI-7 for maps).

The blue shift at higher dose is consistent with previous experiments by Chen et al. who studied the effects of heavy ion irradiation on MoS_2[252]. They reported a blue shift in the MoS_2 PL and suggested that subsequent oxygen adsorption at the generated defects was responsible. Similarly, 15 keV electron exposures at an areal dose of $2.8x10^{-3}$ $\frac{nC}{\mu m^2}$ was accompanied by a PL blue-shift attributed to a compressive strain of ~ 0.4%[253], consistent with sulfur vacancy generation. The Raman spectroscopy results reveal that the peak ratio of the A_{1g}/E^1_{2g} peaks <= $2x10^{-1}$ $\frac{nC}{\mu m^2}$ stays relatively constant, while there is a slight blue-shift in the A_{1g} peak with increasing areal dose. At the $5x10^{-1}$ $\frac{nC}{\mu m^2}$ areal dose, the A_{1g}/E^1_{2g} peak ratio increases and the LA(M) mode, indicative of defect generation, raises slightly above the noise. Data from heavy ion exposures of single layer MoS_2 also revealed a significant blue shift in the A_{1g} peak with increasing fluence. The E^1_{2g} peak initially slightly blue shifted and then red shifted at higher fluence. They attributed the blue shift to the creation of sulfur vacancies, which can induce compressive strain[253,254]. The increase in the A_{1g}/E^1_{2g} peak ratio is also consistent with the dissociation of the Mo-S bond, which can decrease the amplitude of the in-plane mode and enhance the restoring force (blue shift) and enhance the Mo vibration and increase the restoring force out-of-plane mode[248]. Additionally, oxygen adsorption to defect sites can p-dope transition metal chalcogenides, which can

preferentially blue-shift the A_{1g} peak of MoS_2[255–257]. Similarly, previous 15 keV electron exposures revealed a systematic blue shift in both the A_{1g} and E_{2g} peak.

Conclusions

We demonstrate that focused electron beam induced etching is a versatile direct write chemical patterning process for MoS_2. The etch rates are determined and rationalized by the estimated precursor and electron fluxes. The results suggest the process is much "softer" than comparable focused ion beam approaches as sub-surface material damage is mitigated by the very low mass of the electrons. Photoluminescence and Raman spectroscopy suggest the creation of sulfur vacancies, which successively etch laterally due to the high reactivity of the unsaturated bonds. STEM of line scans reveal an etching linewidth < 40 nm, and atomic resolution STEM shows that the etching process proceeds by the preferential formation of point and extended defects, with larger pores forming as the etch progresses. Focused electron beam induced editing of a series of field effect transistor channels was performed and confirmed the utility of the process to edit "on-demand" the MoS_2 active channel regions. Sub-monolayer etching of channel regions is also explored and at very low doses, enhanced n-type behavior is realized consistent with generating sulfur vacancies. Higher areal doses of the channel regions produced a systematic decrease in the I_{SD}, consistent with progressive etching of the channel region. Photoluminescence and Raman spectroscopy of the exposed channel regions suggest that the point and extended defects generated by the process can generate strain due to the sulfur vacancies or alternatively can be compensated by adsorbed O_2 molecules which leads to slight shifts in the spectra.

Materials and Methods

MoS_2 monolayers were grown by CVD using a liquid precursor: **the** liquid precursor was prepared by mixing three types of aqueous solutions (denoted as A, B, and C) into 2:6:1 where A, B, and C are (A) 0.1 g of ammonium molybdate tetrahydrate (Sigma-Aldrich, 431346] in 10 ml of deionized (DI) water, (B) 0.1 g of sodium hydroxide (Sigma-Aldrich, 306576) in 50 ml of DI water, and (C) 60% (w/v) solution of iodixanol in water (Sigma-Aldrich, D1556) (see Kim, *et. al.* for details)[258]. The liquid precursor was dropped onto the SiO_2 (300 nm)/Si substrate, followed by spin-coating at 3,000 rpm for 30 s. The monolayer MoS_2 flakes were synthesized by two-zone furnace CVD with a 2-inch chamber size. In each zone, 0.3 g of sulfur (Sigma-Aldrich, 344621) and the liquid precursor-coated SiO_2 (300 nm)/Si substrate were placed independently. The sulfur was heated to 210 °C for 8 min while the substrate zone was elevated to 720 °C for 8 min and the temperature is maintained for 10 min for the growth of MoS_2. During the growth process, 600 sccm of N_2 was flowing as a carrier gas.

MoS_2 monolayers were transferred onto gold quantifoil TEM grids by spin coating and drying a polycarbonate film on the as-grown substrate. The film was then removed from the as-grown substrate and washed with water and IPA before being transferred to the grid and heated at 100 ºC again to improve adhesion. The film was finally dissolved in chloroform, leaving the flakes on the TEM grid.

Focused electron beam induced etching experiments were conducted in an FEI Nova Nanolab 600 with a XeF_2 gas injection system positioned ~150 mm above the substrate and out of the field of view of the electron beam. The crucible was heated to 32 ºC. The system was typically

pumped to a base pressure of $5x10^{-7}$ Torr and when the XeF_2 GIS is opened the chamber pressure rises to $2x10^{-6}$ Torr. The localized pressure is significantly larger than the chamber pressure due to the localized flow through the nozzle, but still below the pressure of most XeF_2 spontaneous etching experiments (~1 Torr). The electron beam patterning conditions were 5 ms dwell time and 20 nm pixel spacing, a 5keV beam energy and the beam current was either 0.4 or 1.6 nA. The total areal electron dose was determined by the number of raster scanned passes, beam current and dwell time averaged over the patterned area.

Device fabrication was carried out by standard e-beam lithography processes. First, PMMA (495-A4) was spin coated on the $MoS_2/SiO_2/Si$ substrate at a spin speed of 3000 RPM to achieve a thickness of ~200 nm. Electrode patterns with 5 or 2 μm channel lengths and 2 μm wide electrodes were written with 40 nA current (JEOL-8100FS). The exposed patterns were then developed in MIBK/IPA (1:3) for ~1 min along with post IPA clean. Finally, Cr/Au (10nm/50nm) metal electrodes were deposited onto the exposed patterns via e-beam evaporation under high vacuum (10^{-6} Torr).

Three terminal FET measurements were carried out under high vacuum (~10^{-6} Torr) and at ambient temperature conditions using Kiethley 4200-SCS parameter analyzer. The I_D-V_g characteristics were measured by sweeping the back gate voltages (V_g) from -80 V to +80 V with constant drain bias V_d = 1 V. The field effect electron mobilities were calculated by using the equation $\mu_{FE} = \frac{1}{C_g} \cdot \frac{1}{V_D} \cdot \frac{L}{W} \cdot \frac{\delta I_D}{\delta V_g}$, where C_g =1.2x10^{-8} F/cm^2 is the gate capacitance of ~ 280 nm of SiO_2. L and W are the respective channel lengths and widths, V_D = 1 V is the constant drain voltage and $\frac{\delta I_D}{\delta V_g}$ is the slope extracted from the linear region of the I_D-V_g curves. The threshold voltages V_{th}

were extracted by linear extrapolation (LE) method by estimating the V_g axis intercept (i.e., I_D = 0) of the linear extrapolation of the I_D–V_g curve where the slopes are maximum.

AFM scans were performed on an Asylum MFP-3D Infinity atomic force microscope in air using tapping mode. Raman and Photoluminescence spectroscopy were performed by a Renishaw inVia Raman microscope using 1800 l/m and 300 l/m diffraction gratings, respectively. Spectral acquisitions with a 532 nm laser used 100% laser power and 1 ms exposure times for 1 accumulation per spot. Map spectra were acquired with the previous parameters with motorized stage movements of a 0.5 μm step size.

Scanning transmission electron microscopy imaging was performed using an aberration-corrected Nion UltraSTEM 100, operating at 60 keV. A nominal probe current of ~30 pA, convergence angle of 31mrad, and nominal collection angle between ~50 and 200 mrad for medium-angle annular dark-field STEM imaging. Prior to STEM experiments, the sample was baked at 160ºC under vacuum to reduce surface contamination.

Acknowledgments

All research was performed at the Center for Nanophase Materials Sciences, which is a U.S. Department of Energy Office of Science user facility at Oak Ridge National Laboratory (ORNL). Support for S.J.R. was partially provided through Laboratory Directed Research and Development Program funds of Oak Ridge National Laboratory, which is managed by UT-Battelle, LLC, for the U.S. Department of Energy. Two UTK SMART program summer interns; B. Hedrick and D. Narcho assisted in process development.

APPENDIX

Supporting Information

SI-1. Exfoliated Multilayer MoS_2 Etching on SiO_2 Substrates

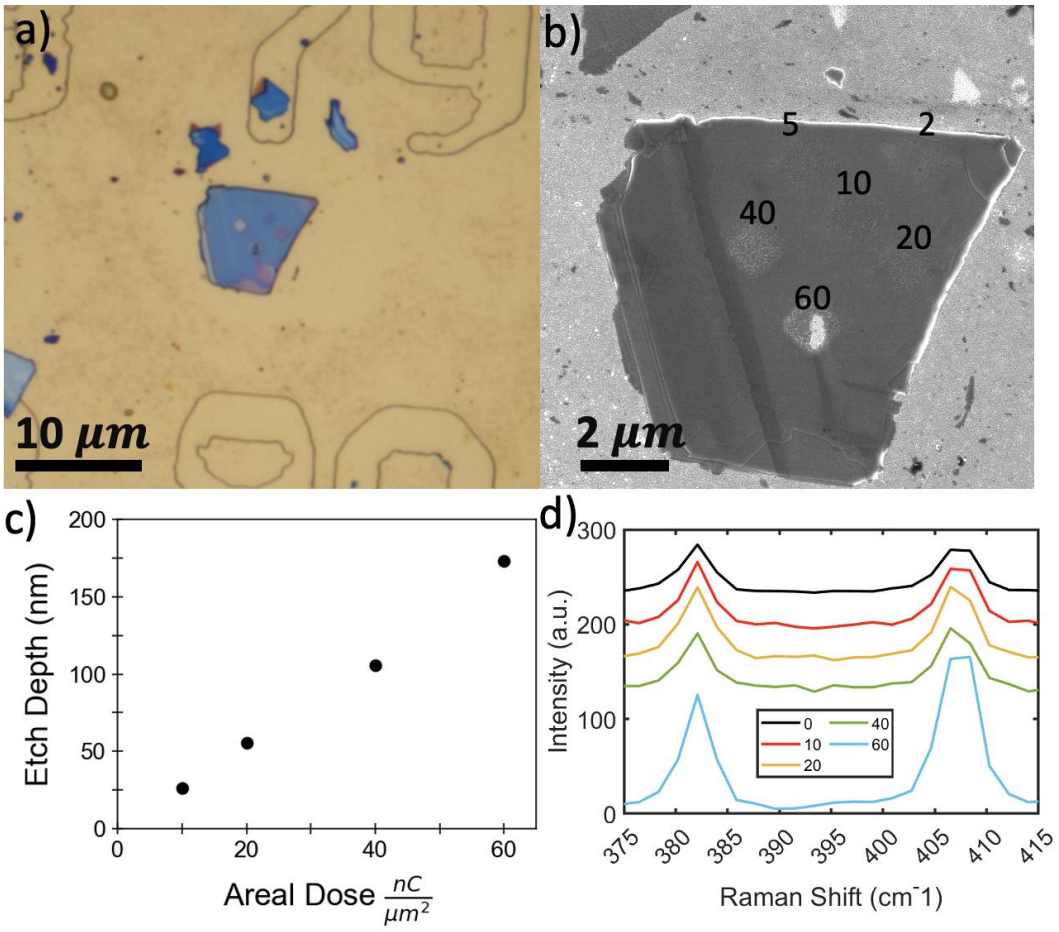

Figure 53. a) Optical and b) secondary electron images of an exfoliated 200nm thick flake, on a gold thin film etched with a 1.6 nA beam current; labels in b) are area doses in $\frac{nC}{\mu m^2}$. c) Plot of the etch depth versus areal dose of the etched boxes of the 4 highest doses shown in a) and b). d) A plot of the Raman spectra of the A_{1g} and E^1_{2g} peaks measured for various FEEBIE areal doses.

SI-2. Exfoliated Multilayer MoS_2 Etching on SiO_2 Substrates

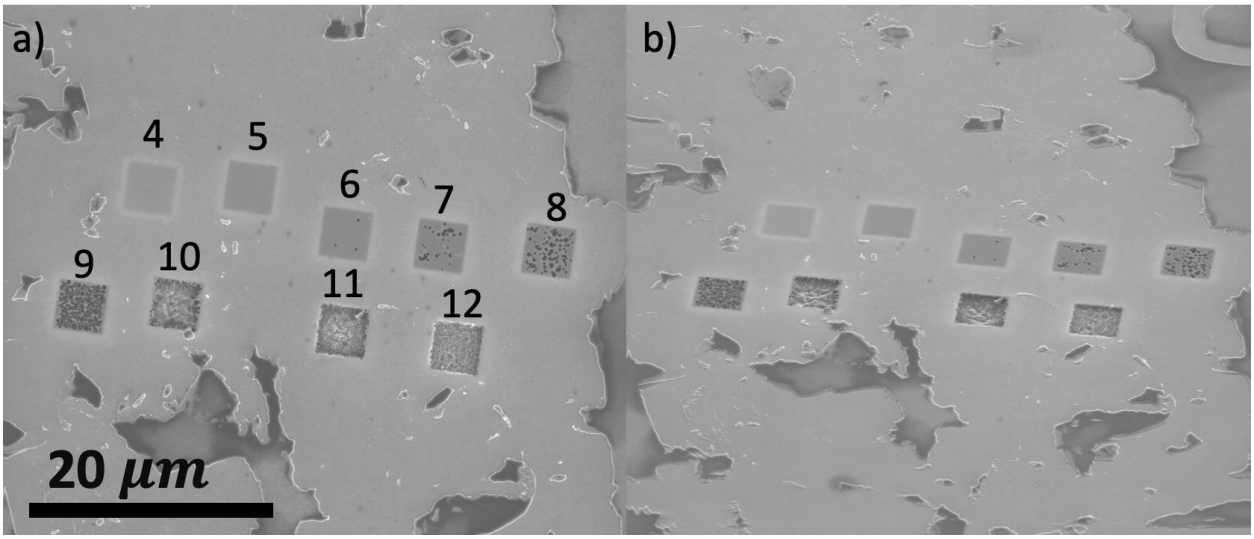

Figure 54. a) 0º and b) 52º tilt SEM Images showing the pore development and underlying SiO_2 EBIE, with exposure doses from 4-12 $\frac{nC}{\mu m^2}$.

SI-3. LA(M) Raman Mode of Etched Exfoliated Multilayer MoS_2 and Transferred Monolayer MoS_2

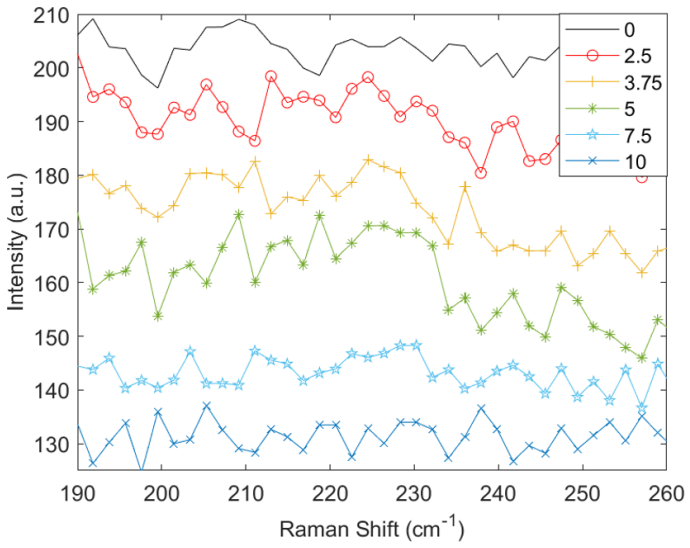

Figure 55. a) Raman spectroscopy of the LA(M) mode of exfoliated multilayer MoS_2 on gold, showing that no associated disorder emerges for during the FEBIE boxes etched with different doses in $\frac{nC}{\mu m^2}$.

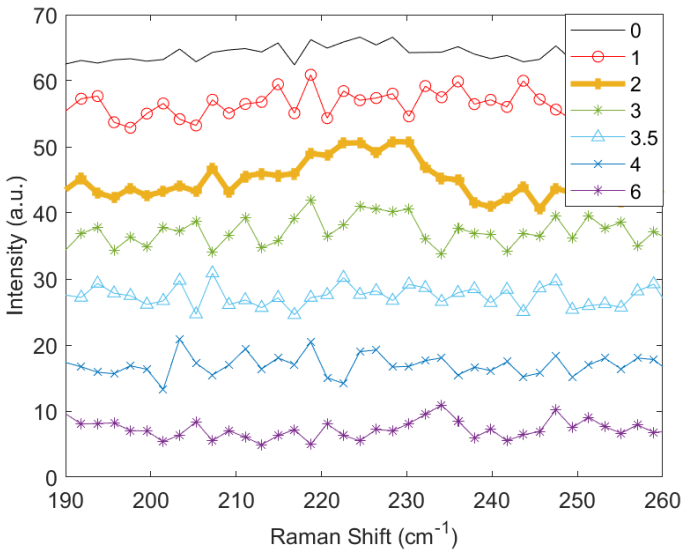

Figure 56. a) Raman spectroscopy of the LA(M) mode of monolayer MoS_2 on gold, showing boxes etched with different doses in $\frac{nC}{\mu m^2}$. A small LA(M) peak is observable at 2 $\frac{nC}{\mu m^2}$, which we attribute to a high density of line defects associated with the pores, before the flake etching completes around 3.5 $\frac{nC}{\mu m^2}$.

SI-4. AFM of Monolayer Etched MoS_2 Flakes

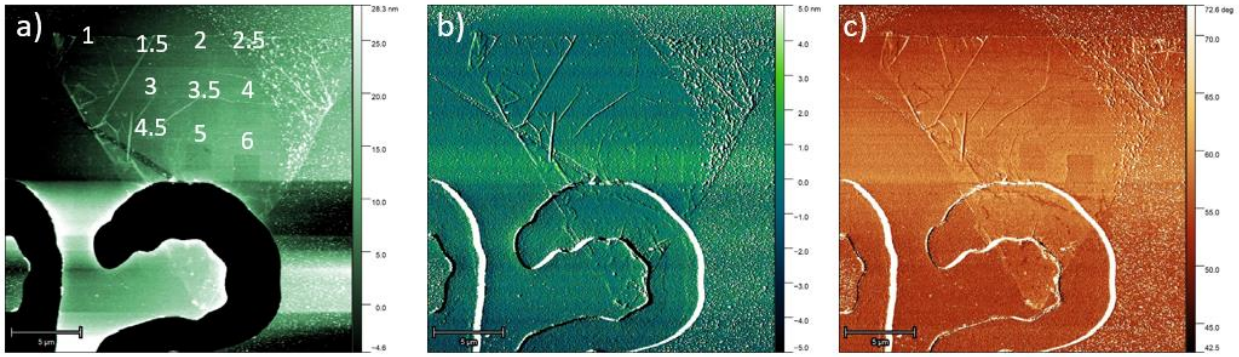

Figure 57. a) Height b) amplitude and c) phase AFM maps of the monolayer MoS_2 flakes, transferred on gold. The FEBIE dose in shown in a) in $\frac{nC}{\mu m^2}$. The roughness of the gold film is 1.8 nm and the roughness of the monolayer flake is 1.4 nm.

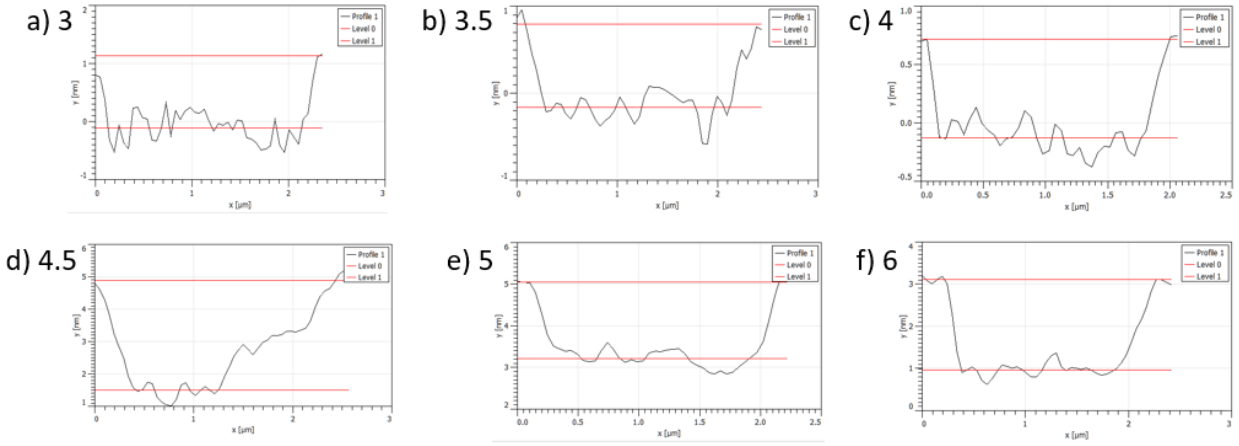

Figure 58. AFM line profile maps of the six FEBIE regions with noticeable etching. Etched boxes with exposures of 3 - 6 $\frac{nC}{\mu m^2}$ are shown where a pixel average of 38 pixels was used for each profile. Etch profiles are not shown for boxes 1 - 2.5 $\frac{nC}{\mu m^2}$ as AFM did not measure a clear change in film profile.

SI-5. Uncropped STEM Segmentation Difference Images

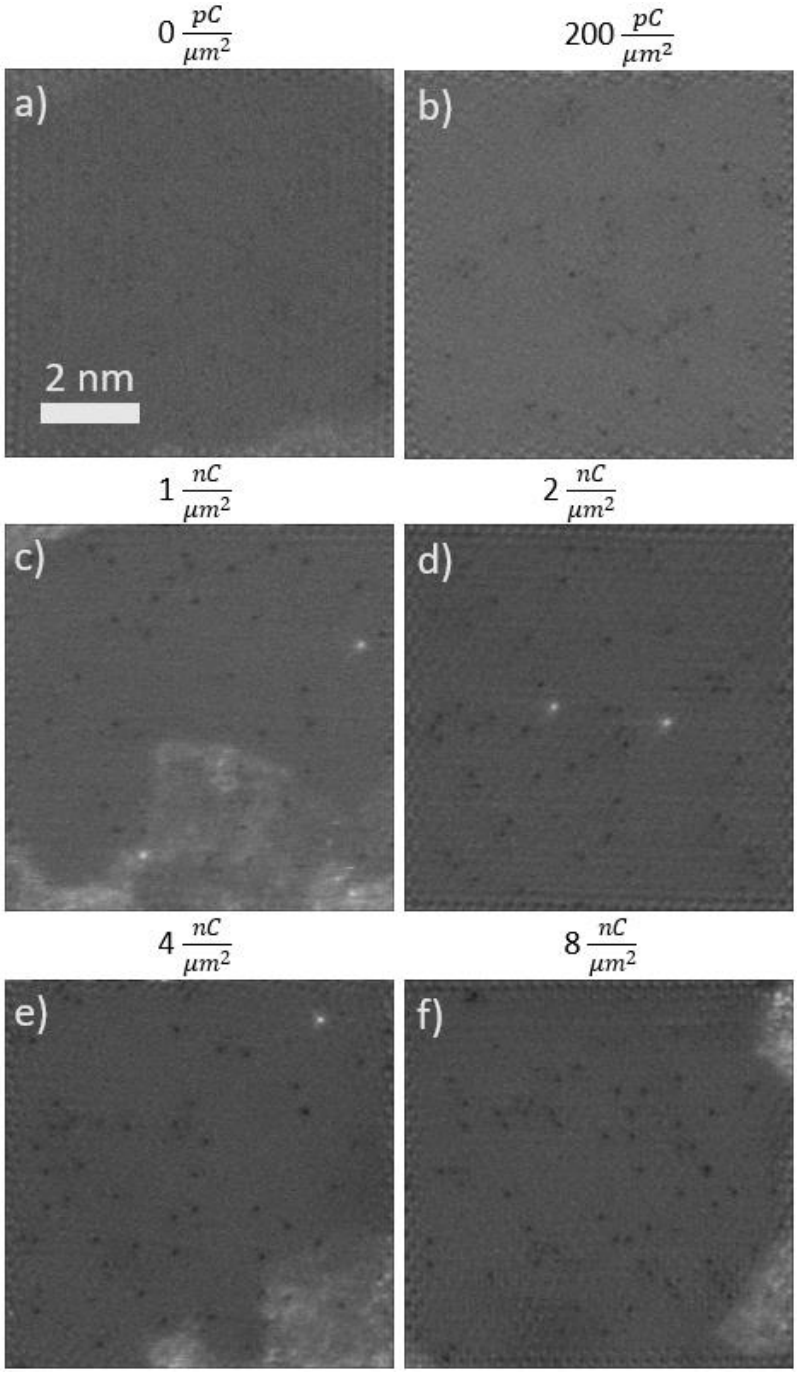

Figure 59. a-f) Uncropped FFT difference images of a series of MAADF-STEM images at progressively increasing electron-beam doses. All images are 8x8 nm FOV.

SI-6. Raman and Photoluminescence Spectroscopy of Nanoribbon Devices

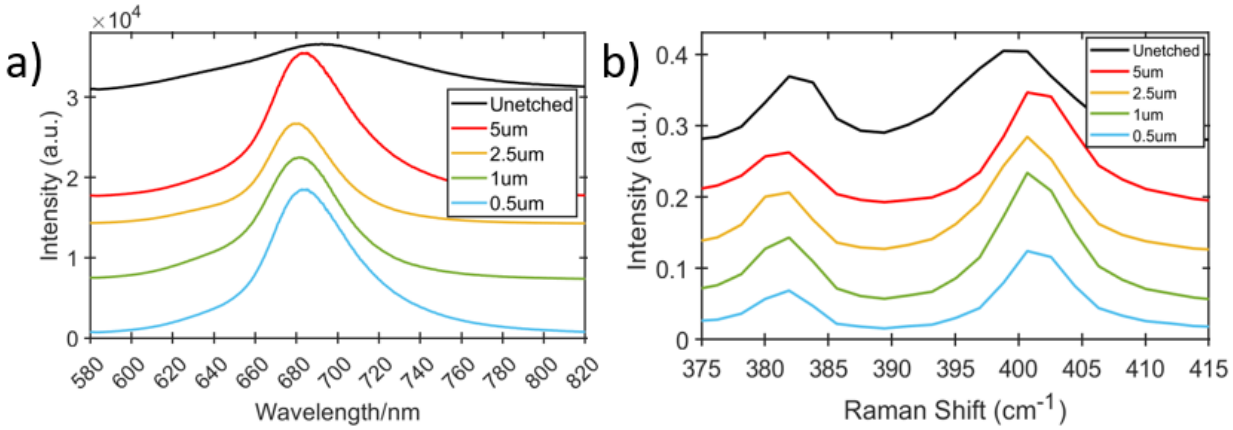

Figure 60. a) Photoluminescence and b) Raman spectra of the nanoribbon device etched to different channel widths.

SI-7. Raman and Photoluminescence Maps of Subthreshold Etching Devices

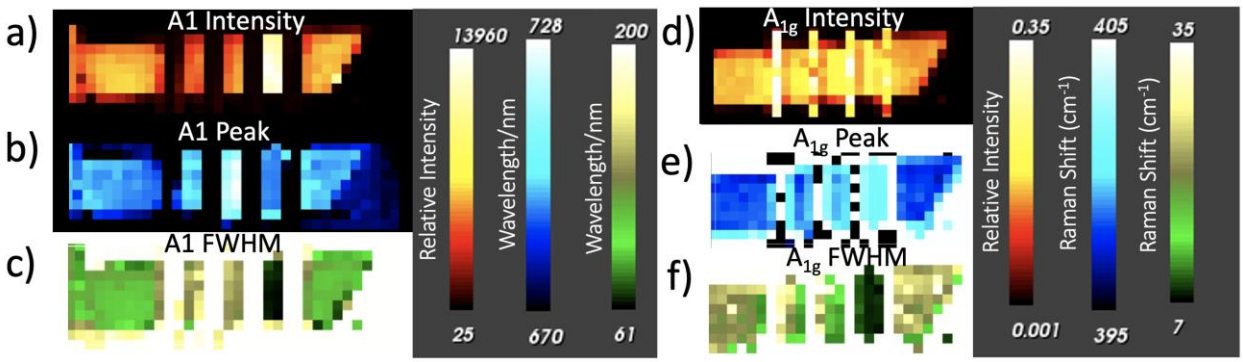

Figure 61. Photoluminescence maps of the subthreshold dose devices showing a) the A1 exiton mode relative intensity, b) the A1 peak position and c) the A1 FWHM. Raman maps of the A_{1g} peak showing d) the A_{1g} peak relative intensity, e) the A_{1g} peak position and f) the A_{1g} FWHM.

REFERENCES

(1) Zhang, Y.; Liu, C.; Whalley, D. Direct-Write Techniques for Maskless Production of Microelectronics: A Review of Current State-of-the-Art Technologies. In *2009 International Conference on Electronic Packaging Technology & High Density Packaging*; 2009; pp 497–503. https://doi.org/10.1109/ICEPT.2009.5270702.

(2) Zhang, B.; He, J.; Li, X.; Xu, F.; Li, D. Micro/Nanoscale Electrohydrodynamic Printing: From 2D to 3D. *Nanoscale* **2016**, *8* (34), 15376–15388. https://doi.org/10.1039/C6NR04106J.

(3) Kim, B. H.; Onses, M. S.; Lim, J. B.; Nam, S.; Oh, N.; Kim, H.; Yu, K. J.; Lee, J. W.; Kim, J.-H.; Kang, S.-K.; Lee, C. H.; Lee, J.; Shin, J. H.; Kim, N. H.; Leal, C.; Shim, M.; Rogers, J. A. High-Resolution Patterns of Quantum Dots Formed by Electrohydrodynamic Jet Printing for Light-Emitting Diodes. *Nano Lett.* **2015**, *15* (2), 969–973. https://doi.org/10.1021/nl503779e.

(4) Traub, M. C.; Longsine, W.; Truskett, V. N. Advances in Nanoimprint Lithography. *Annu. Rev. Chem. Biomol. Eng.* **2016**, *7* (1), 583–604. https://doi.org/10.1146/annurev-chembioeng-080615-034635.

(5) Jin, F.; Liu, J.; Zhao, Y.-Y.; Dong, X.-Z.; Zheng, M.-L.; Duan, X.-M. λ/30 Inorganic Features Achieved by Multi-Photon 3D Lithography. *Nat. Commun.* **2022**, *13* (1), 1357. https://doi.org/10.1038/s41467-022-29036-7.

(6) Fowlkes, J. D.; Winkler, R.; Lewis, B. B.; Stanford, M. G.; Plank, H.; Rack, P. D. Simulation-Guided 3D Nanomanufacturing via Focused Electron Beam Induced Deposition. *ACS Nano* **2016**, *10* (6), 6163–6172. https://doi.org/10.1021/acsnano.6b02108.

(7) Winkler, R.; Fowlkes, J. D.; Rack, P. D.; Plank, H. 3D Nanoprinting via Focused Electron Beams. *J. Appl. Phys.* **2019**, *125* (21), 210901. https://doi.org/10.1063/1.5092372.

(8) Winkler, R.; Schmidt, F.-P.; Haselmann, U.; Fowlkes, J. D.; Lewis, B. B.; Kothleitner, G.; Rack, P. D.; Plank, H. Direct-Write 3D Nanoprinting of Plasmonic Structures. *ACS Appl. Mater. Interfaces* **2017**, *9* (9), 8233–8240. https://doi.org/10.1021/acsami.6b13062.

(9) Smith, D. A.; Fowlkes, J. D.; Rack, P. D. A Nanoscale Three-Dimensional Monte Carlo Simulation of Electron-Beam-Induced Deposition with Gas Dynamics. *Nanotechnology* **2007**, *18* (26), 265308. https://doi.org/10.1088/0957-4484/18/26/265308.

(10) Smith, D. A.; Fowlkes, J. D.; Rack, P. D. Simulating the Effects of Surface Diffusion on Electron Beam Induced Deposition via a Three-Dimensional Monte Carlo Simulation. *Nanotechnology* **2008**, *19* (41), 415704. https://doi.org/10.1088/0957-4484/19/41/415704.

(11) Smith, D. A.; Fowlkes, J. D.; Rack, P. D. Understanding the Kinetics and Nanoscale Morphology of Electron-Beam-Induced Deposition via a Three-Dimensional Monte Carlo Simulation: The Effects of the Precursor Molecule and the Deposited Material. *Small* **2008**, *4* (9), 1382–1389. https://doi.org/10.1002/smll.200701133.

(12) Cullen, J.; Lobo, C. J.; Ford, M. J.; Toth, M. Electron-Beam-Induced Deposition as a Technique for Analysis of Precursor Molecule Diffusion Barriers and Prefactors. *ACS*

Appl. Mater. Interfaces **2015**, *7* (38), 21408–21415. https://doi.org/10.1021/acsami.5b06341.
(13) Salvat-Pujol, F.; Valentí, R.; Werner, W. S. Surface Excitations in the Modelling of Electron Transport for Electron-Beam-Induced Deposition Experiments. *Beilstein J. Nanotechnol.* **2015**, *6* (1), 1260–1267. https://doi.org/10.3762/bjnano.6.129.
(14) Fowlkes, J. D.; Winkler, R.; Mutunga, E.; Rack, P. D.; Plank, H. Simulation Informed CAD for 3D Nanoprinting. *Micromachines* **2020**, *11* (1), 8. https://doi.org/10.3390/mi11010008.
(15) Fowlkes, J. D.; Winkler, R.; Lewis, B. B.; Fernández-Pacheco, A.; Skoric, L.; Sanz-Hernández, D.; Stanford, M. G.; Mutunga, E.; Rack, P. D.; Plank, H. High-Fidelity 3D-Nanoprinting via Focused Electron Beams: Computer-Aided Design (3BID). *ACS Appl. Nano Mater.* **2018**, *1* (3), 1028–1041. https://doi.org/10.1021/acsanm.7b00342.
(16) Keller, L.; Huth, M. Pattern Generation for Direct-Write Three-Dimensional Nanoscale Structures via Focused Electron Beam Induced Deposition. *Beilstein J. Nanotechnol.* **2018**, *9*, 2581–2598. https://doi.org/10.3762/bjnano.9.240.
(17) Thorman, R. M.; Kumar T. P., R.; Fairbrother, D. H.; Ingólfsson, O. The Role of Low-Energy Electrons in Focused Electron Beam Induced Deposition: Four Case Studies of Representative Precursors. *Beilstein J. Nanotechnol.* **2015**, *6*, 1904–1926. https://doi.org/10.3762/bjnano.6.194.
(18) Barth, S.; Huth, M.; Jungwirth, F. Precursors for Direct-Write Nanofabrication with Electrons. *J. Mater. Chem. C* **2020**, *8* (45), 15884–15919. https://doi.org/10.1039/D0TC03689G.
(19) Makise, K.; Mitsuishi, K.; Shimojo, M.; Shinozaki, B. Microstructural Analysis and Transport Properties of MoO and MoC Nanostructures Prepared by Focused Electron Beam-Induced Deposition. *Sci. Rep.* **2014**, *4* (1), 5740. https://doi.org/10.1038/srep05740.
(20) Weber, M.; Koops, H. W. P.; Rudolph, M.; Kretz, J.; Schmidt, G. New Compound Quantum Dot Materials Produced by Electron-beam Induced Deposition. *J. Vac. Sci. Technol. B Microelectron. Nanometer Struct. Process. Meas. Phenom.* **1995**, *13* (3), 1364–1368. https://doi.org/10.1116/1.587854.
(21) Sengupta, S.; Li, C.; Baumier, C.; Kasumov, A.; Guéron, S.; Bouchiat, H.; Fortuna, F. Superconducting Nanowires by Electron-Beam-Induced Deposition. *Appl. Phys. Lett.* **2015**, *106* (4), 042601. https://doi.org/10.1063/1.4906269.
(22) Mulders, J. J. L.; Belova, L. M.; Riazanova, A. Electron Beam Induced Deposition at Elevated Temperatures: Compositional Changes and Purity Improvement. *Nanotechnology* **2010**, *22* (5), 055302. https://doi.org/10.1088/0957-4484/22/5/055302.
(23) Porrati, F.; Sachser, R.; Huth, M. The Transient Electrical Conductivity of W-Based Electron-Beam-Induced Deposits during Growth, Irradiation and Exposure to Air. *Nanotechnology* **2009**, *20* (19), 195301. https://doi.org/10.1088/0957-4484/20/19/195301.
(24) Gavagnin, M.; Wanzenboeck, H. D.; Belic, D.; Shawrav, M. M.; Persson, A.; Gunnarsson, K.; Svedlindh, P.; Bertagnolli, E. Magnetic Force Microscopy Study of Shape Engineered FEBID Iron Nanostructures. *Phys. Status Solidi A* **2014**, *211* (2), 368–374. https://doi.org/10.1002/pssa.201330114.
(25) Gavagnin, M.; Wanzenboeck, H. D.; Belić, D.; Bertagnolli, E. Synthesis of Individually Tuned Nanomagnets for Nanomagnet Logic by Direct Write Focused

Electron Beam Induced Deposition. *ACS Nano* **2013**, *7* (1), 777–784. https://doi.org/10.1021/nn305079a.
(26) Lukasczyk, T.; Schirmer, M.; Steinrück, H.-P.; Marbach, H. Electron-Beam-Induced Deposition in Ultrahigh Vacuum: Lithographic Fabrication of Clean Iron Nanostructures. *Small* **2008**, *4* (6), 841–846. https://doi.org/10.1002/smll.200701095.
(27) Córdoba, R.; Sharma, N.; Kölling, S.; Koenraad, P. M.; Koopmans, B. High-Purity 3D Nano-Objects Grown by Focused-Electron-Beam Induced Deposition. *Nanotechnology* **2016**, *27* (35), 355301. https://doi.org/10.1088/0957-4484/27/35/355301.
(28) Rodríguez, L. A.; Deen, L.; Córdoba, R.; Magén, C.; Snoeck, E.; Koopmans, B.; Teresa, J. M. D. Influence of the Shape and Surface Oxidation in the Magnetization Reversal of Thin Iron Nanowires Grown by Focused Electron Beam Induced Deposition. *Beilstein J. Nanotechnol.* **2015**, *6* (1), 1319–1331. https://doi.org/10.3762/bjnano.6.136.
(29) Utke, I.; Friedli, V.; Michler, J.; Bret, T.; Multone, X.; Hoffmann, P. Density Determination of Focused-Electron-Beam-Induced Deposits with Simple Cantilever-Based Method. *Appl. Phys. Lett.* **2006**, *88* (3), 031906. https://doi.org/10.1063/1.2158516.
(30) Utke, I.; Bret, T.; Laub, D.; Buffat, Ph.; Scandella, L.; Hoffmann, P. Thermal Effects during Focused Electron Beam Induced Deposition of Nanocomposite Magnetic-Cobalt-Containing Tips. *Microelectron. Eng.* **2004**, *73–74*, 553–558. https://doi.org/10.1016/j.mee.2004.02.084.
(31) Nikulina, E.; Idigoras, O.; Vavassori, P.; Chuvilin, A.; Berger, A. Magneto-Optical Magnetometry of Individual 30 Nm Cobalt Nanowires Grown by Electron Beam Induced Deposition. *Appl. Phys. Lett.* **2012**, *100* (14), 142401. https://doi.org/10.1063/1.3701153.
(32) Ehrichs, E. E.; Smith, W. F.; de Lozanne, A. L. Four-Probe Resistance Measurements of Nickel Wires Written with a Scanning Tunneling Microscope/Scanning Electron Microscope System. *Ultramicroscopy* **1992**, *42–44*, 1438–1442. https://doi.org/10.1016/0304-3991(92)90462-S.
(33) Pakeltis, G.; Hu, Z.; Nixon, A. G.; Mutunga, E.; Anyanwu, C. P.; West, C. A.; Idrobo, J. C.; Plank, H.; Masiello, D. J.; Fowlkes, J. D.; Rack, P. D. Focused Electron Beam Induced Deposition Synthesis of 3D Photonic and Magnetic Nanoresonators. *ACS Appl. Nano Mater.* **2019**, *2* (12), 8075–8082. https://doi.org/10.1021/acsanm.9b02182.
(34) Botman, A.; Mulders, J. J. L.; Weemaes, R.; Mentink, S. Purification of Platinum and Gold Structures after Electron-Beam-Induced Deposition. *Nanotechnology* **2006**, *17* (15), 3779–3785. https://doi.org/10.1088/0957-4484/17/15/028.
(35) Warneke, Z.; Rohdenburg, M.; Warneke, J.; Kopyra, J.; Swiderek, P. Electron-Driven and Thermal Chemistry during Water-Assisted Purification of Platinum Nanomaterials Generated by Electron Beam Induced Deposition. *Beilstein J. Nanotechnol.* **2018**, *9*, 77–90. https://doi.org/10.3762/bjnano.9.10.
(36) Wnuk, J. D.; Gorham, J. M.; Rosenberg, S. G.; van Dorp, W. F.; Madey, T. E.; Hagen, C. W.; Fairbrother, D. H. Electron Induced Surface Reactions of the Organometallic Precursor Trimethyl(Methylcyclopentadienyl)Platinum(IV). *J. Phys. Chem. C* **2009**, *113* (6), 2487–2496. https://doi.org/10.1021/jp807824c.
(37) Sachser, R.; Porrati, F.; Schwalb, C. H.; Huth, M. Universal Conductance Correction in a Tunable Strongly Coupled Nanogranular Metal. *Phys. Rev. Lett.* **2011**, *107* (20), 206803. https://doi.org/10.1103/PhysRevLett.107.206803.

(38) Porrati, F.; Sachser, R.; Schwalb, C. H.; Frangakis, A. S.; Huth, M. Tuning the Electrical Conductivity of Pt-Containing Granular Metals by Postgrowth Electron Irradiation. *J. Appl. Phys.* **2011**, *109* (6), 063715. https://doi.org/10.1063/1.3559773.
(39) Plank, H.; Noh, J. H.; Fowlkes, J. D.; Lester, K.; Lewis, B. B.; Rack, P. D. Electron-Beam-Assisted Oxygen Purification at Low Temperatures for Electron-Beam-Induced Pt Deposits: Towards Pure and High-Fidelity Nanostructures. *ACS Appl. Mater. Interfaces* **2014**, *6* (2), 1018–1024. https://doi.org/10.1021/am4045458.
(40) Belić, D.; Shawrav, M. M.; Gavagnin, M.; Stöger-Pollach, M.; Wanzenboeck, H. D.; Bertagnolli, E. Direct-Write Deposition and Focused-Electron-Beam-Induced Purification of Gold Nanostructures. *ACS Appl. Mater. Interfaces* **2015**, *7* (4), 2467–2479. https://doi.org/10.1021/am507327y.
(41) Botman, A.; Mulders, J. J. L.; Hagen, C. W. Creating Pure Nanostructures from Electron-Beam-Induced Deposition Using Purification Techniques: A Technology Perspective. *Nanotechnology* **2009**, *20* (37), 372001. https://doi.org/10.1088/0957-4484/20/37/372001.
(42) Lewis, B. B.; Stanford, M. G.; Fowlkes, J. D.; Lester, K.; Plank, H.; Rack, P. D. Electron-Stimulated Purification of Platinum Nanostructures Grown via Focused Electron Beam Induced Deposition. *Beilstein J. Nanotechnol.* **2015**, *6*. https://doi.org/10.3762/bjnano.6.94.
(43) Mehendale, S.; Mulders, J. J. L.; Trompenaars, P. H. F. A New Sequential EBID Process for the Creation of Pure Pt Structures from MeCpPtMe3. *Nanotechnology* **2013**, *24* (14), 145303. https://doi.org/10.1088/0957-4484/24/14/145303.
(44) Geier, B.; Gspan, C.; Winkler, R.; Schmied, R.; Fowlkes, J. D.; Fitzek, H.; Rauch, S.; Rattenberger, J.; Rack, P. D.; Plank, H. Rapid and Highly Compact Purification for Focused Electron Beam Induced Deposits: A Low Temperature Approach Using Electron Stimulated H2O Reactions. *J. Phys. Chem. C* **2014**, *118* (25), 14009–14016. https://doi.org/10.1021/jp503442b.
(45) Noh, J. H.; Stanford, M. G.; Lewis, B. B.; Fowlkes, J. D.; Plank, H.; Rack, P. D. Nanoscale Electron Beam-Induced Deposition and Purification of Ruthenium for Extreme Ultraviolet Lithography Mask Repair. *Appl. Phys. A* **2014**, *117* (4), 1705–1713. https://doi.org/10.1007/s00339-014-8745-0.
(46) Fowlkes, J. D.; Geier, B.; Lewis, B. B.; Rack, P. D.; Stanford, M. G.; Winkler, R.; Plank, H. Electron Nanoprobe Induced Oxidation: A Simulation of Direct-Write Purification. *Phys. Chem. Chem. Phys.* **2015**, *17* (28), 18294–18304. https://doi.org/10.1039/C5CP01196E.
(47) Botman, A.; Hesselberth, M.; Mulders, J. J. L. Improving the Conductivity of Platinum-Containing Nano-Structures Created by Electron-Beam-Induced Deposition. *Microelectron. Eng.* **2008**, *85* (5), 1139–1142. https://doi.org/10.1016/j.mee.2007.12.036.
(48) Fang, J.-Y.; Qin, S.-Q.; Zhang, X.-A.; Liu, D.-Q.; Chang, S.-L. Annealing Effect of Platinum-Incorporated Nanowires Created by Focused Ion/Electron-Beam-Induced Deposition. *Chin. Phys. B* **2014**, *23* (8), 088111. https://doi.org/10.1088/1674-1056/23/8/088111.
(49) Gopal, V.; Radmilovic, V. R.; Daraio, C.; Jin, S.; Yang, P.; Stach, E. A. Rapid Prototyping of Site-Specific Nanocontacts by Electron and Ion Beam Assisted Direct-

Write Nanolithography. *Nano Lett.* **2004**, *4* (11), 2059–2063. https://doi.org/10.1021/nl0492133.
(50) Langford, R. M.; Wang, T.-X.; Ozkaya, D. Reducing the Resistivity of Electron and Ion Beam Assisted Deposited Pt. *Microelectron. Eng.* **2007**, *84* (5), 784–788. https://doi.org/10.1016/j.mee.2007.01.055.
(51) Roberts, N. A.; Fowlkes, J. D.; Magel, G. A.; Rack, P. D. Enhanced Material Purity and Resolution via Synchronized Laser Assisted Electron Beam Induced Deposition of Platinum. *Nanoscale* **2012**, *5* (1), 408–415. https://doi.org/10.1039/C2NR33014H.
(52) Stanford, M. G.; Lewis, B. B.; Noh, J. H.; Fowlkes, J. D.; Rack, P. D. Inert Gas Enhanced Laser-Assisted Purification of Platinum Electron-Beam-Induced Deposits. *ACS Appl. Mater. Interfaces* **2015**, *7* (35), 19579–19588. https://doi.org/10.1021/acsami.5b02488.
(53) De Teresa, J. M.; Córdoba, R.; Fernández-Pacheco, A.; Montero, O.; Strichovanec, P.; Ibarra, M. R. Origin of the Difference in the Resistivity of As-Grown Focused-Ion- and Focused-Electron-Beam-Induced Pt Nanodeposits. *J. Nanomater.* **2009**, *2009*, 1–11. https://doi.org/10.1155/2009/936863.
(54) De Teresa, J. M.; Orús, P.; Córdoba, R.; Philipp, P. Comparison between Focused Electron/Ion Beam-Induced Deposition at Room Temperature and under Cryogenic Conditions. *Micromachines* **2019**, *10* (12), 799. https://doi.org/10.3390/mi10120799.
(55) Gruber, G.; Urgell, C.; Tavernarakis, A.; Stavrinadis, A.; Tepsic, S.; Magén, C.; Sangiao, S.; de Teresa, J. M.; Verlot, P.; Bachtold, A. Mass Sensing for the Advanced Fabrication of Nanomechanical Resonators. *Nano Lett.* **2019**, *19* (10), 6987–6992. https://doi.org/10.1021/acs.nanolett.9b02351.
(56) Lukashenko, S. Y.; Mukhin, I. S.; Komissarenko, F. E.; Gorbenko, O. M.; Sapozhnikov, I. D.; Felshtyn, M. L.; Uskov, A. V.; Golubok, A. O. Resonant Mass Detector Based on Carbon Nanowhiskers with Traps for Nanoobjects Weighing. *Phys. Status Solidi A* **2018**, *215* (21), 1800046. https://doi.org/10.1002/pssa.201800046.
(57) Plank, H.; Winkler, R.; Schwalb, C. H.; Hütner, J.; Fowlkes, J. D.; Rack, P. D.; Utke, I.; Huth, M. Focused Electron Beam-Based 3D Nanoprinting for Scanning Probe Microscopy: A Review. *Micromachines* **2020**, *11* (1), 48. https://doi.org/10.3390/mi11010048.
(58) Wu, W.; Pauly, M. Chiral Plasmonic Nanostructures: Recent Advances in Their Synthesis and Applications. *Mater. Adv.* **2022**, *3* (1), 186–215. https://doi.org/10.1039/D1MA00915J.
(59) Keller, L.; Al Mamoori, M. K. I.; Pieper, J.; Gspan, C.; Stockem, I.; Schröder, C.; Barth, S.; Winkler, R.; Plank, H.; Pohlit, M.; Müller, J.; Huth, M. Direct-Write of Free-Form Building Blocks for Artificial Magnetic 3D Lattices. *Sci. Rep.* **2018**, *8* (1), 6160. https://doi.org/10.1038/s41598-018-24431-x.
(60) Mayer, K. M.; Hafner, J. H. Localized Surface Plasmon Resonance Sensors. *Chem. Rev.* **2011**, *111* (6), 3828–3857. https://doi.org/10.1021/cr100313v.
(61) Lal, S.; Link, S.; Halas, N. J. Nano-Optics from Sensing to Waveguiding. *Nat. Photonics* **2007**, *1* (11), 641–648. https://doi.org/10.1038/nphoton.2007.223.

(62) Homola, J. Surface Plasmon Resonance Sensors for Detection of Chemical and Biological Species. *Chem. Rev.* **2008**, *108* (2), 462–493. https://doi.org/10.1021/cr068107d.
(63) Nam, J.-M.; Oh, J.-W.; Lee, H.; Suh, Y. D. Plasmonic Nanogap-Enhanced Raman Scattering with Nanoparticles. *Acc. Chem. Res.* **2016**, *49* (12), 2746–2755. https://doi.org/10.1021/acs.accounts.6b00409.
(64) Tsai, K.-T.; Wurtz, G. A.; Chu, J.-Y.; Cheng, T.-Y.; Wang, H.-H.; Krasavin, A. V.; He, J.-H.; Wells, B. M.; Podolskiy, V. A.; Wang, J.-K.; Wang, Y.-L.; Zayats, A. V. Looking into Meta-Atoms of Plasmonic Nanowire Metamaterial. *Nano Lett.* **2014**, *14* (9), 4971–4976. https://doi.org/10.1021/nl501283c.
(65) Chikkaraddy, R.; de Nijs, B.; Benz, F.; Barrow, S. J.; Scherman, O. A.; Rosta, E.; Demetriadou, A.; Fox, P.; Hess, O.; Baumberg, J. J. Single-Molecule Strong Coupling at Room Temperature in Plasmonic Nanocavities. *Nature* **2016**, *535* (7610), 127–130. https://doi.org/10.1038/nature17974.
(66) Mubeen, S.; Lee, J.; Singh, N.; Krämer, S.; Stucky, G. D.; Moskovits, M. An Autonomous Photosynthetic Device in Which All Charge Carriers Derive from Surface Plasmons. *Nat. Nanotechnol.* **2013**, *8* (4), 247–251. https://doi.org/10.1038/nnano.2013.18.
(67) Knight, M. W.; Sobhani, H.; Nordlander, P.; Halas, N. J. Photodetection with Active Optical Antennas. *Science* **2011**, *332* (6030), 702–704. https://doi.org/10.1126/science.1203056.
(68) Ozbay, E. Plasmonics: Merging Photonics and Electronics at Nanoscale Dimensions. *Science* **2006**, *311* (5758), 189–193. https://doi.org/10.1126/science.1114849.
(69) Sorger, V. J.; Oulton, R. F.; Ma, R.-M.; Zhang, X. Toward Integrated Plasmonic Circuits. *MRS Bull.* **2012**, *37* (8), 728–738. https://doi.org/10.1557/mrs.2012.170.
(70) Davis, T. J.; Gómez, D. E.; Roberts, A. Plasmonic Circuits for Manipulating Optical Information. *Nanophotonics* **2017**, *6* (3), 543–559. https://doi.org/10.1515/nanoph-2016-0131.
(71) Tuniz, A.; Bickerton, O.; Diaz, F. J.; Käsebier, T.; Kley, E.-B.; Kroker, S.; Palomba, S.; de Sterke, C. M. Modular Nonlinear Hybrid Plasmonic Circuit. *Nat. Commun.* **2020**, *11* (1), 2413. https://doi.org/10.1038/s41467-020-16190-z.
(72) Höflich, K.; Yang, R. B.; Berger, A.; Leuchs, G.; Christiansen, S. The Direct Writing of Plasmonic Gold Nanostructures by Electron-Beam-Induced Deposition. *Adv. Mater.* **2011**, *23* (22–23), 2657–2661. https://doi.org/10.1002/adma.201004114.
(73) Teresa, J. M. D.; Fernández-Pacheco, A.; Córdoba, R.; Serrano-Ramón, L.; Sangiao, S.; Ibarra, M. R. Review of Magnetic Nanostructures Grown by Focused Electron Beam Induced Deposition (FEBID). *J. Phys. Appl. Phys.* **2016**, *49* (24), 243003. https://doi.org/10.1088/0022-3727/49/24/243003.
(74) Utke, I.; Hoffmann, P.; Berger, R.; Scandella, L. High-Resolution Magnetic Co Supertips Grown by a Focused Electron Beam. *Appl. Phys. Lett.* **2002**, *80* (25), 4792–4794. https://doi.org/10.1063/1.1489097.
(75) Belova, L. M.; Hellwig, O.; Dobisz, E.; Dan Dahlberg, E. Rapid Preparation of Electron Beam Induced Deposition Co Magnetic Force Microscopy Tips with 10 Nm

Spatial Resolution. *Rev. Sci. Instrum.* **2012**, *83* (9), 093711. https://doi.org/10.1063/1.4752225.
(76) Perentes, A.; Sinicco, G.; Boero, G.; Dwir, B.; Hoffmann, P. Focused Electron Beam Induced Deposition of Nickel. *J. Vac. Sci. Technol. B Microelectron. Nanometer Struct. Process. Meas. Phenom.* **2007**, *25* (6), 2228–2232. https://doi.org/10.1116/1.2794071.
(77) Córdoba, R.; Barcones, B.; Roelfsema, E.; Verheijen, M. A.; Mulders, J. J. L.; Trompenaars, P. H. F.; Koopmans, B. Functional Nickel-Based Deposits Synthesized by Focused Beam Induced Processing. *Nanotechnology* **2016**, *27* (6), 065303. https://doi.org/10.1088/0957-4484/27/6/065303.
(78) Porrati, F.; Pohlit, M.; Müller, J.; Barth, S.; Biegger, F.; Gspan, C.; Plank, H.; Huth, M. Direct Writing of CoFe Alloy Nanostructures by Focused Electron Beam Induced Deposition from a Heteronuclear Precursor. *Nanotechnology* **2015**, *26* (47), 475701. https://doi.org/10.1088/0957-4484/26/47/475701.
(79) Lavrijsen, R.; Córdoba, R.; Schoenaker, F. J.; Ellis, T. H.; Barcones, B.; Kohlhepp, J. T.; Swagten, H. J. M.; Koopmans, B.; Teresa, J. M. D.; Magén, C.; Ibarra, M. R.; Trompenaars, P.; Mulders, J. J. L. Fe:O:C Grown by Focused-Electron-Beam-Induced Deposition: Magnetic and Electric Properties. *Nanotechnology* **2010**, *22* (2), 025302. https://doi.org/10.1088/0957-4484/22/2/025302.
(80) Córdoba, R.; Lavrijsen, R.; Fernández-Pacheco, A.; Ibarra, M. R.; Schoenaker, F.; Ellis, T.; Barcones-Campo, B.; Kohlhepp, J. T.; Swagten, H. J. M.; Koopmans, B.; Mulders, J. J. L.; Teresa, J. M. D. Giant Anomalous Hall Effect in Fe-Based Microwires Grown by Focused-Electron-Beam-Induced Deposition. *J. Phys. Appl. Phys.* **2011**, *45* (3), 035001. https://doi.org/10.1088/0022-3727/45/3/035001.
(81) Franken, J. H.; van der Heijden, M. A. J.; Ellis, T. H.; Lavrijsen, R.; Daniels, C.; McGrouther, D.; Swagten, H. J. M.; Koopmans, B. Beam-Induced Fe Nanopillars as Tunable Domain-Wall Pinning Sites. *Adv. Funct. Mater.* **2014**, *24* (23), 3508–3514. https://doi.org/10.1002/adfm.201303540.
(82) Takeguchi, M.; Shimojo, M.; Mitsuishi, K.; Tanaka, M.; Che, R.; Furuya, K. Fabrication of Nanostructures with Different Iron Concentration by Electron Beam Induced Deposition with a Mixture Gas of Iron Carbonyl and Ferrocene, and Their Magnetic Properties. *J. Mater. Sci.* **2006**, *41* (14), 4532–4536. https://doi.org/10.1007/s10853-006-0091-y.
(83) Xu, Q. Y.; Kageyama, Y.; Suzuki, T. Ion-Beam-Induced Chemical-Vapor Deposition of FePt and CoPt Particles. *J. Appl. Phys.* **2005**, *97* (10), 10K308. https://doi.org/10.1063/1.1851875.
(84) Pogoryelov, Y.; Suzuki, T. Fabrication of Alloy FeCoPt Particles by IBICVD and Their Characterization. *IEEE Trans. Magn.* **2007**, *43* (2), 888–890. https://doi.org/10.1109/TMAG.2006.888493.
(85) Bruk, M. A.; Zhikharev, E. N.; Grigor'ev, E. I.; Spirin, A. V.; Kal'nov, V. A.; Kardash, I. E. Focused Electron Beam-Induced Deposition of Iron- and Carbon-Containing Nanostructures from Triiron Dodecacarbonyl Vapor. *High Energy Chem.* **2005**, *39* (2), 65–68. https://doi.org/10.1007/s10733-005-0015-4.

(86) Kunz, R. R.; Mayer, T. M. Catalytic Growth Rate Enhancement of Electron Beam Deposited Iron Films. *Appl. Phys. Lett.* **1987**, *50* (15), 962–964. https://doi.org/10.1063/1.97999.
(87) Kunz, R. R.; Allen, T. E.; Mayer, T. M. Selective Area Deposition of Metals Using Low-energy Electron Beams. *J. Vac. Sci. Technol. B Microelectron. Process. Phenom.* **1987**, *5* (5), 1427–1431. https://doi.org/10.1116/1.583629.
(88) Shimojo, M.; Takeguchi, M.; Tanaka, M.; Mitsuishi, K.; Furuya, K. Electron Beam-Induced Deposition Using Iron Carbonyl and the Effects of Heat Treatment on Nanostructure. *Appl. Phys. A* **2004**, *79* (8), 1869–1872. https://doi.org/10.1007/s00339-004-2952-z.
(89) Shimojo, M.; Zhang, W.; Takeguchi, M.; Tanaka, M.; Mitsuishi, K.; Furuya, K. Nanodot and Nanorod Formation in Electron-Beam-Induced Deposition Using Iron Carbonyl. *Jpn. J. Appl. Phys.* **2005**, *44* (7S), 5651. https://doi.org/10.1143/JJAP.44.5651.
(90) Takeguchi, M.; Shimojo, M.; Furuya, K. Fabrication of Magnetic Nanostructures Using Electron Beam Induced Chemical Vapour Deposition. *Nanotechnology* **2005**, *16* (8), 1321–1325. https://doi.org/10.1088/0957-4484/16/8/057.
(91) Takeguchi, M.; Shimojo, M.; Furuya, K. Fabrication of Alpha-Iron and Iron Carbide Nanostructures by Electron-Beam Induced Chemical Vapor Deposition and Postdeposition Heat Treatment. *Jpn. J. Appl. Phys.* **2005**, *44* (7S), 5631. https://doi.org/10.1143/JJAP.44.5631.
(92) Tanaka, M.; Chu, F.; Shimojo, M.; Takeguchi, M.; Mitsuishi, K.; Furuya, K. Position- and Size-Controlled Fabrication of Iron Silicide Nanorods by Electron-Beam-Induced Deposition Using an Ultrahigh-Vacuum Transmission Electron Microscope. *Appl. Phys. Lett.* **2005**, *86* (18), 183104. https://doi.org/10.1063/1.1922576.
(93) Tanaka, M.; Shimojo, M.; Takeguchi, M.; Mitsuishi, K.; Furuya, K. Formation of Iron Nano-Dot Arrays by Electron Beam-Induced Deposition Using an Ultrahigh Vacuum Transmission Electron Microscope. *J. Cryst. Growth* **2005**, *275* (1), e2361–e2366. https://doi.org/10.1016/j.jcrysgro.2004.11.337.
(94) Che, R. C.; Takeguchi, M.; Shimojo, M.; Zhang, W.; Furuya, K. Fabrication and Electron Holography Characterization of FePt Alloy Nanorods. *Appl. Phys. Lett.* **2005**, *87* (22), 223109. https://doi.org/10.1063/1.2136071.
(95) Zhang, W.; Shimojo, M.; Takeguchi, M.; Che, R.-C.; Furuya, K. Generation Mechanism and in Situ Growth Behavior of α-Iron Nanocrystals by Electron Beam Induced Deposition. *Adv. Eng. Mater.* **2006**, *8* (8), 711–714. https://doi.org/10.1002/adem.200600026.
(96) Takeguchi, M.; Shimojo, M.; Che, R.; Furuya, K. Fabrication of a Nano-Magnet on a Piezo-Driven Tip in a TEM Sample Holder. *J. Mater. Sci.* **2006**, *41* (9), 2627–2630. https://doi.org/10.1007/s10853-006-7825-8.
(97) Tanaka, M.; Chu, F.; Shimojo, M.; Takeguchi, M.; Mitsuishi, K.; Furuya, K. Formation of Iron Silicide Nano-Islands on Si Substrates by Metal Organic Chemical Vapor Deposition under Electron Beams. *J. Mater. Sci.* **2006**, *41* (9), 2667–2671. https://doi.org/10.1007/s10853-006-7868-x.

(98) Shimojo, M.; Takeguchi, M.; Furuya, K. Formation of Crystalline Iron Oxide Nanostructures by Electron Beam-Induced Deposition at Room Temperature. *Nanotechnology* **2006**, *17* (15), 3637–3640. https://doi.org/10.1088/0957-4484/17/15/003.
(99) Zhang, W.; Shimojo, M.; Takeguchi, M.; Furuya, K. Electron Beam-Induced Formation of Nanosized α-Fe Crystals. *J. Mater. Sci.* **2006**, *41* (9), 2577–2580. https://doi.org/10.1007/s10853-006-7783-1.
(100) Zhang, W.; Che, R.; Takeguchi, M.; Shimojo, M.; Furuya, K. Formation of Fe–Pt Intermetallic Phase in Nanostructures by Electron-Beam-Induced Deposition and Postdeposition Alloying Processes. *Surf. Interface Anal.* **2006**, *38* (12–13), 1527–1529. https://doi.org/10.1002/sia.2410.
(101) Shimojo, M.; Takeguchi, M.; Mitsuishi, K.; Tanaka, M.; Furuya, K. Mechanisms of Crystalline Iron Oxide Formation in Electron Beam-Induced Deposition. *Jpn. J. Appl. Phys.* **2007**, *46* (9S), 6247. https://doi.org/10.1143/JJAP.46.6247.
(102) Takeguchi, M.; Shimojo, M.; Furuya, K. Nanostructure Fabrication by Electron-Beam-Induced Deposition with Metal Carbonyl Precursor and Water Vapor. *Jpn. J. Appl. Phys.* **2007**, *46* (9S), 6183. https://doi.org/10.1143/JJAP.46.6183.
(103) Tanaka, M.; Mitsuishi, K.; Takeguchi, M.; Shimojo, M.; Furuya, K.; Koguchi, N. Electron-Beam-Induced Deposition of Fe Nanoparticles and Thin Films on SrTiO3 Substrates. *Jpn. J. Appl. Phys.* **2007**, *46* (9S), 6243. https://doi.org/10.1143/JJAP.46.6243.
(104) Hochleitner, G.; Wanzenboeck, H. D.; Bertagnolli, E. Electron Beam Induced Deposition of Iron Nanostructures. *J. Vac. Sci. Technol. B Microelectron. Nanometer Struct. Process. Meas. Phenom.* **2008**, *26* (3), 939–944. https://doi.org/10.1116/1.2907781.
(105) Lukasczyk, T.; Schirmer, M.; Steinrück, H.-P.; Marbach, H. Generation of Clean Iron Structures by Electron-Beam-Induced Deposition and Selective Catalytic Decomposition of Iron Pentacarbonyl on Rh(110). *Langmuir* **2009**, *25* (19), 11930–11939. https://doi.org/10.1021/la901612u.
(106) Schirmer, M.; Walz, M.-M.; Papp, C.; Kronast, F.; Gray, A. X.; Balke, B.; Cramm, S.; Fadley, C. S.; Steinrück, H.-P.; Marbach, H. Fabrication of Layered Nanostructures by Successive Electron Beam Induced Deposition with Two Precursors: Protective Capping of Metallic Iron Structures. *Nanotechnology* **2011**, *22* (47), 475304. https://doi.org/10.1088/0957-4484/22/47/475304.
(107) Porrati, F.; Sachser, R.; Walz, M.-M.; Vollnhals, F.; Steinrück, H.-P.; Marbach, H.; Huth, M. Magnetotransport Properties of Iron Microwires Fabricated by Focused Electron Beam Induced Autocatalytic Growth. *J. Phys. Appl. Phys.* **2011**, *44* (42), 425001. https://doi.org/10.1088/0022-3727/44/42/425001.
(108) Vollnhals, F.; Woolcot, T.; Walz, M.-M.; Seiler, S.; Steinrück, H.-P.; Thornton, G.; Marbach, H. Electron Beam-Induced Writing of Nanoscale Iron Wires on a Functional Metal Oxide. *J. Phys. Chem. C* **2013**, *117* (34), 17674–17679. https://doi.org/10.1021/jp405640a.
(109) Gavagnin, M.; Wanzenboeck, H. D.; Shawrav, M. M.; Belic, D.; Wachter, S.; Waid, S.; Stoeger–Pollach, M.; Bertagnolli, E. Focused Electron Beam-Induced CVD of Iron: A Practical Guide for Direct Writing. *Chem. Vap. Depos.* **2014**, *20* (7-8–9), 243–250. https://doi.org/10.1002/cvde.201407118.

(110) Gavagnin, M.; Wanzenboeck, H. D.; Wachter, S.; Shawrav, M. M.; Persson, A.; Gunnarsson, K.; Svedlindh, P.; Stöger-Pollach, M.; Bertagnolli, E. Free-Standing Magnetic Nanopillars for 3D Nanomagnet Logic. *ACS Appl. Mater. Interfaces* **2014**, *6* (22), 20254–20260. https://doi.org/10.1021/am505785t.
(111) Shawrav, M. M.; Belić, D.; Gavagnin, M.; Wachter, S.; Schinnerl, M.; Wanzenboeck, H. D.; Bertagnolli, E. Electron Beam-Induced CVD of Nanoalloys for Nanoelectronics. *Chem. Vap. Depos.* **2014**, *20* (7-8–9), 251–257. https://doi.org/10.1002/cvde.201407119.
(112) Ribar, A.; Danko, M.; Országh, J.; Ferreira da Silva, F.; Utke, I.; Matejčík, Š. Dissociative Excitation Study of Iron Pentacarbonyl Molecule. *Eur. Phys. J. D* **2015**, *69* (4), 117. https://doi.org/10.1140/epjd/e2015-50755-x.
(113) Lau, Y. M.; Chee, P. C.; Thong, J. T. L.; Ng, V. Properties and Applications of Cobalt-Based Material Produced by Electron-Beam-Induced Deposition. *J. Vac. Sci. Technol. A* **2002**, *20* (4), 1295–1302. https://doi.org/10.1116/1.1481040.
(114) Ervin, M. H.; Nichols, B. M. Electron Beam Induced Deposition of Cobalt for Use as Single- and Multiwalled Carbon Nanotube Growth Catalyst. *J. Vac. Sci. Technol. B Microelectron. Nanometer Struct. Process. Meas. Phenom.* **2009**, *27* (6), 2982–2985. https://doi.org/10.1116/1.3250259.
(115) Gazzadi, G. C.; Mulders, H.; Trompenaars, P.; Ghirri, A.; Affronte, M.; Grillo, V.; Frabboni, S. Focused Electron Beam Deposition of Nanowires from Cobalt Tricarbonyl Nitrosyl (Co(CO)3NO) Precursor. *J. Phys. Chem. C* **2011**, *115* (40), 19606–19611. https://doi.org/10.1021/jp206562h.
(116) Gazzadi, G. C.; Mulders, J. J. L.; Trompenaars, P.; Ghirri, A.; Rota, A.; Affronte, M.; Frabboni, S. Characterization of a New Cobalt Precursor for Focused Beam Deposition of Magnetic Nanostructures. *Microelectron. Eng.* **2011**, *88* (8), 1955–1958. https://doi.org/10.1016/j.mee.2010.12.031.
(117) Rosenberg, S. G.; Barclay, M.; Fairbrother, D. H. Electron Beam Induced Reactions of Adsorbed Cobalt Tricarbonyl Nitrosyl (Co(CO)3NO) Molecules. *J. Phys. Chem. C* **2013**, *117* (31), 16053–16064. https://doi.org/10.1021/jp404905t.
(118) Papp, P.; Engmann, S.; Kučera, M.; Stano, M.; Matejčík, Š.; Ingólfsson, O. An Experimental and Theoretical Study on Structural Parameters and Energetics in Ionization and Dissociation of Cobalt Tricarbonyl Nitrosyl. *Int. J. Mass Spectrom.* **2013**, *356*, 24–32. https://doi.org/10.1016/j.ijms.2013.09.011.
(119) Vollnhals, F.; Drost, M.; Tu, F.; Carrasco, E.; Späth, A.; Fink, R. H.; Steinrück, H.-P.; Marbach, H. Electron-Beam Induced Deposition and Autocatalytic Decomposition of Co(CO)3NO. *Beilstein J. Nanotechnol.* **2014**, *5* (1), 1175–1185. https://doi.org/10.3762/bjnano.5.129.
(120) Pablo-Navarro, J.; Sangiao, S.; Magén, C.; de Teresa, J. M. Magnetic Functionalization of Scanning Probes by Focused Electron Beam Induced Deposition Technology. *Magnetochemistry* **2021**, *7* (10), 140. https://doi.org/10.3390/magnetochemistry7100140.
(121) Lasseter, J.; Rack, P. D.; Randolph, S. J. Selected Area Deposition of PtCx Nanostructures: Implications for Functional Coatings of 3D Nanoarchitectures. *ACS Appl. Nano Mater.* **2022**, *5* (8), 10890–10899. https://doi.org/10.1021/acsanm.2c02182.

(122) Córdoba, R. Editorial for the Special Issue on Nanofabrication with Focused Electron/Ion Beam Induced Processing. *Micromachines* **2021**, *12* (8), 893. https://doi.org/10.3390/mi12080893.
(123) Huth, M.; Porrati, F.; Dobrovolskiy, O. V. Focused Electron Beam Induced Deposition Meets Materials Science. *Microelectron. Eng.* **2018**, *185–186*, 9–28. https://doi.org/10.1016/j.mee.2017.10.012.
(124) Lewis, J. A.; Smay, J. E.; Stuecker, J.; Cesarano, J. Direct Ink Writing of Three-Dimensional Ceramic Structures. *J. Am. Ceram. Soc.* **2006**, *89* (12), 3599–3609. https://doi.org/10.1111/j.1551-2916.2006.01382.x.
(125) Lewis, J. A. Direct Ink Writing of 3D Functional Materials. *Adv. Funct. Mater.* **2006**, *16* (17), 2193–2204. https://doi.org/10.1002/adfm.200600434.
(126) Jeon, H.; Schmidt, R.; Barton, J. E.; Hwang, D. J.; Gamble, L. J.; Castner, D. G.; Grigoropoulos, C. P.; Healy, K. E. Chemical Patterning of Ultrathin Polymer Films by Direct-Write Multiphoton Lithography. *J. Am. Chem. Soc.* **2011**, *133* (16), 6138–6141. https://doi.org/10.1021/ja200313q.
(127) Malinauskas, M.; Danilevičius, P.; Juodkazis, S. Three-Dimensional Micro-/Nano-Structuring via Direct Write Polymerization with Picosecond Laser Pulses. *Opt. Express* **2011**, *19* (6), 5602–5610. https://doi.org/10.1364/OE.19.005602.
(128) Zhang, B.; He, J.; Li, X.; Xu, F.; Li, D. Micro/Nanoscale Electrohydrodynamic Printing: From 2D to 3D. *Nanoscale* **2016**, *8* (34), 15376–15388. https://doi.org/10.1039/C6NR04106J.
(129) Piner, R. D.; Zhu, J.; Xu, F.; Hong, S.; Mirkin, C. A. "Dip-Pen" Nanolithography. *Science* **1999**. https://doi.org/10.1126/science.283.5402.661.
(130) Osgood, R. M. Laser Microchemistry and Its Application to Electron-Device Fabrication. *Annu. Rev. Phys. Chem.* **1983**, *34* (1), 77–101. https://doi.org/10.1146/annurev.pc.34.100183.000453.
(131) Ehrlich, D. J.; Tsao, J. Y. Chapter 3 - Laser Direct Writing for VLSI* *This Work Was Supported by the Defense Advanced Research Projects Agency, the Department of the Air Force (in Part under a Specific Program Sponsored by the Air Force Office of Scientific Research), and the Army Research Office. In *VLSI Electronics Microstructure Science*; Einspruch, N. G., Ed.; Elsevier, 1983; Vol. 7, pp 129–164. https://doi.org/10.1016/B978-0-12-234107-6.50008-9.
(132) Bert Huis in 't Veld; Overmeyer, L.; Schmidt, M.; Wegener, K.; Malshe, A.; Bartolo, P. Micro Additive Manufacturing Using Ultra Short Laser Pulses. *CIRP Ann.* **2015**, *64* (2), 701–724. https://doi.org/10.1016/j.cirp.2015.05.007.
(133) Piqué, A.; Auyeung, R. C. Y.; Kim, H.; Charipar, N. A.; Mathews, S. A. Laser 3D Micro-Manufacturing. *J. Phys. Appl. Phys.* **2016**, *49* (22), 223001. https://doi.org/10.1088/0022-3727/49/22/223001.
(134) Hirt, L.; Reiser, A.; Spolenak, R.; Zambelli, T. Additive Manufacturing of Metal Structures at the Micrometer Scale. *Adv. Mater.* **2017**, *29* (17), 1604211. https://doi.org/10.1002/adma.201604211.
(135) Winkler, R.; Geier, B.; Plank, H. Spatial Chemistry Evolution during Focused Electron Beam-Induced Deposition: Origins and Workarounds. *Appl. Phys. A* **2014**, *117* (4), 1675–1688. https://doi.org/10.1007/s00339-014-8496-y.

(136) Rodríguez, L. A.; Deen, L.; Córdoba, R.; Magén, C.; Snoeck, E.; Koopmans, B.; Teresa, J. M. D. Influence of the Shape and Surface Oxidation in the Magnetization Reversal of Thin Iron Nanowires Grown by Focused Electron Beam Induced Deposition. *Beilstein J. Nanotechnol.* **2015**, *6* (1), 1319–1331. https://doi.org/10.3762/bjnano.6.136.
(137) Utke, I.; Bret, T.; Laub, D.; Buffat, Ph.; Scandella, L.; Hoffmann, P. Thermal Effects during Focused Electron Beam Induced Deposition of Nanocomposite Magnetic-Cobalt-Containing Tips. *Microelectron. Eng.* **2004**, *73–74*, 553–558. https://doi.org/10.1016/j.mee.2004.02.084.
(138) Randolph, S. J.; Fowlkes, J. D.; Rack, P. D. Effects of Heat Generation during Electron-Beam-Induced Deposition of Nanostructures. *J. Appl. Phys.* **2005**, *97* (12), 124312. https://doi.org/10.1063/1.1942627.
(139) Mutunga, E.; Winkler, R.; Sattelkow, J.; Rack, P. D.; Plank, H.; Fowlkes, J. D. Impact of Electron-Beam Heating during 3D Nanoprinting. *ACS Nano* **2019**, *13* (5), 5198–5213. https://doi.org/10.1021/acsnano.8b09341.
(140) Winkler, R.; Lewis, B. B.; Fowlkes, J. D.; Rack, P. D.; Plank, H. High-Fidelity 3D-Nanoprinting via Focused Electron Beams: Growth Fundamentals. *ACS Appl. Nano Mater.* **2018**, *1* (3), 1014–1027. https://doi.org/10.1021/acsanm.8b00158.
(141) Stanford, M. G.; Lewis, B. B.; Noh, J. H.; Fowlkes, J. D.; Roberts, N. A.; Plank, H.; Rack, P. D. Purification of Nanoscale Electron-Beam-Induced Platinum Deposits via a Pulsed Laser-Induced Oxidation Reaction. *ACS Appl. Mater. Interfaces* **2014**, *6* (23), 21256–21263. https://doi.org/10.1021/am506246z.
(142) Mutunga, E.; Winkler, R.; Sattelkow, J.; Rack, P. D.; Plank, H.; Fowlkes, J. D. Impact of Electron-Beam Heating during 3D Nanoprinting. *ACS Nano* **2019**, *13* (5), 5198–5213. https://doi.org/10.1021/acsnano.8b09341.
(143) Faust, M.; Enders, M.; Bruns, M.; Bräse, S.; Gao, K.; Seipenbusch, M. Synthesis of Nanostructured Pt/Oxide Catalyst Particles by MOCVD Process at Ambient Pressure. *Surf. Coat. Technol.* **2013**, *230*, 284–289. https://doi.org/10.1016/j.surfcoat.2013.06.088.
(144) Lewis, B. B.; Winkler, R.; Sang, X.; Pudasaini, P. R.; Stanford, M. G.; Plank, H.; Unocic, R. R.; Fowlkes, J. D.; Rack, P. D. 3D Nanoprinting via Laser-Assisted Electron Beam Induced Deposition: Growth Kinetics, Enhanced Purity, and Electrical Resistivity. *Beilstein J. Nanotechnol.* **2017**, *8*, 801–812. https://doi.org/10.3762/bjnano.8.83.
(145) Pablo-Navarro, J.; Winkler, R.; Haberfehlner, G.; Magén, C.; Plank, H.; De Teresa, J. M. In Situ Real-Time Annealing of Ultrathin Vertical Fe Nanowires Grown by Focused Electron Beam Induced Deposition. *Acta Mater.* **2019**, *174*, 379–386. https://doi.org/10.1016/j.actamat.2019.05.035.
(146) Pablo-Navarro, J.; Magén, C.; de Teresa, J. M. Purified and Crystalline Three-Dimensional Electron-Beam-Induced Deposits: The Successful Case of Cobalt for High-Performance Magnetic Nanowires. *ACS Appl. Nano Mater.* **2018**, *1* (1), 38–46. https://doi.org/10.1021/acsanm.7b00016.
(147) Fernández-Pacheco, A.; Teresa, J. M. D.; Córdoba, R.; Ibarra, M. R. Magnetotransport Properties of High-Quality Cobalt Nanowires Grown by Focused-Electron-Beam-Induced Deposition. *J. Phys. Appl. Phys.* **2009**, *42* (5), 055005. https://doi.org/10.1088/0022-3727/42/5/055005.

(148) Culjak, I.; Abram, D.; Pribanic, T.; Dzapo, H.; Cifrek, M. A Brief Introduction to OpenCV. In *2012 Proceedings of the 35th International Convention MIPRO*; 2012; pp 1725–1730.
(149) Smith, R. An Overview of the Tesseract OCR Engine. In *Ninth International Conference on Document Analysis and Recognition (ICDAR 2007)*; 2007; Vol. 2, pp 629–633. https://doi.org/10.1109/ICDAR.2007.4376991.
(150) Lasseter, J.; Rack, P. D.; Randolph, S. J. Selected Area Deposition of High Purity Gold for Functional 3D Architectures. *Nanomaterials* **2023**, *13* (4), 757. https://doi.org/10.3390/nano13040757.
(151) Mulders, J. J. L. Practical Precursor Aspects for Electron Beam Induced Deposition. *Nanofabrication* **2014**, *1* (1). https://doi.org/10.2478/nanofab-2014-0007.
(152) Dorp, W. F. van; Hagen, C. W. A Critical Literature Review of Focused Electron Beam Induced Deposition. *J. Appl. Phys.* **2008**, *104* (8), 081301. https://doi.org/10.1063/1.2977587.
(153) Silvis-Cividjian, N.; Hagen, C. W. Electron-Beam–Induced Nanometer-Scale Deposition. In *Advances in Imaging and Electron Physics*; Elsevier, 2006; Vol. 143, pp 1–235. https://doi.org/10.1016/S1076-5670(06)43001-9.
(154) Utke, I.; Swiderek, P.; Höflich, K.; Madajska, K.; Jurczyk, J.; Martinović, P.; Szymańska, I. B. Coordination and Organometallic Precursors of Group 10 and 11: Focused Electron Beam Induced Deposition of Metals and Insight Gained from Chemical Vapour Deposition, Atomic Layer Deposition, and Fundamental Surface and Gas Phase Studies. *Coord. Chem. Rev.* **2022**, *458*, 213851. https://doi.org/10.1016/j.ccr.2021.213851.
(155) Carden, W. G.; Lu, H.; Spencer, J. A.; Fairbrother, D. H.; McElwee-White, L. Mechanism-Based Design of Precursors for Focused Electron Beam-Induced Deposition. *MRS Commun.* **2018**, *8* (2), 343–357. https://doi.org/10.1557/mrc.2018.77.
(156) Botman, A.; Mulders, J. J. L.; Weemaes, R.; Mentink, S. Purification of Platinum and Gold Structures after Electron-Beam-Induced Deposition. *Nanotechnology* **2006**, *17* (15), 3779–3785. https://doi.org/10.1088/0957-4484/17/15/028.
(157) Belić, D.; Shawrav, M. M.; Gavagnin, M.; Stöger-Pollach, M.; Wanzenboeck, H. D.; Bertagnolli, E. Direct-Write Deposition and Focused-Electron-Beam-Induced Purification of Gold Nanostructures. *ACS Appl. Mater. Interfaces* **2015**, *7* (4), 2467–2479. https://doi.org/10.1021/am507327y.
(158) Botman, A.; Mulders, J. J. L.; Hagen, C. W. Creating Pure Nanostructures from Electron-Beam-Induced Deposition Using Purification Techniques: A Technology Perspective. *Nanotechnology* **2009**, *20* (37), 372001. https://doi.org/10.1088/0957-4484/20/37/372001.
(159) Lewis, B. B.; Stanford, M. G.; Fowlkes, J. D.; Lester, K.; Plank, H.; Rack, P. D. Electron-Stimulated Purification of Platinum Nanostructures Grown via Focused Electron Beam Induced Deposition. *Beilstein J. Nanotechnol.* **2015**, *6*. https://doi.org/10.3762/bjnano.6.94.
(160) Mehendale, S.; Mulders, J. J. L.; Trompenaars, P. H. F. A New Sequential EBID Process for the Creation of Pure Pt Structures from MeCpPtMe3. *Nanotechnology* **2013**, *24* (14), 145303. https://doi.org/10.1088/0957-4484/24/14/145303.

(161) Botman, A.; Hesselberth, M.; Mulders, J. J. L. Improving the Conductivity of Platinum-Containing Nano-Structures Created by Electron-Beam-Induced Deposition. *Microelectron. Eng.* **2008**, *85* (5), 1139–1142. https://doi.org/10.1016/j.mee.2007.12.036.
(162) Fang, J.-Y.; Qin, S.-Q.; Zhang, X.-A.; Liu, D.-Q.; Chang, S.-L. Annealing Effect of Platinum-Incorporated Nanowires Created by Focused Ion/Electron-Beam-Induced Deposition. *Chin. Phys. B* **2014**, *23* (8), 088111. https://doi.org/10.1088/1674-1056/23/8/088111.
(163) Roberts, N. A.; Fowlkes, J. D.; Magel, G. A.; Rack, P. D. Enhanced Material Purity and Resolution via Synchronized Laser Assisted Electron Beam Induced Deposition of Platinum. *Nanoscale* **2012**, *5* (1), 408–415. https://doi.org/10.1039/C2NR33014H.
(164) Hirt, L.; Reiser, A.; Spolenak, R.; Zambelli, T. Additive Manufacturing of Metal Structures at the Micrometer Scale. *Adv. Mater.* **2017**, *29* (17), 1604211. https://doi.org/10.1002/adma.201604211.
(165) Mohr-Weidenfeller, L.; Häcker, A.-V.; Reinhardt, C.; Manske, E. Two-Photon Direct Laser Writing Beyond the Diffraction Limit Using the Nanopositioning and Nanomeasuring Machine. *Nanomanufacturing Metrol.* **2021**, *4* (3), 149–155. https://doi.org/10.1007/s41871-021-00100-y.
(166) Keller, L.; Al Mamoori, M. K. I.; Pieper, J.; Gspan, C.; Stockem, I.; Schröder, C.; Barth, S.; Winkler, R.; Plank, H.; Pohlit, M.; Müller, J.; Huth, M. Direct-Write of Free-Form Building Blocks for Artificial Magnetic 3D Lattices. *Sci. Rep.* **2018**, *8* (1), 6160. https://doi.org/10.1038/s41598-018-24431-x.
(167) Fischer, P.; Sanz-Hernández, D.; Streubel, R.; Fernández-Pacheco, A. Launching a New Dimension with 3D Magnetic Nanostructures. *APL Mater.* **2020**, *8* (1), 010701. https://doi.org/10.1063/1.5134474.
(168) Sanz-Hernández, D.; Hamans, R. F.; Osterrieth, J.; Liao, J.-W.; Skoric, L.; Fowlkes, J. D.; Rack, P. D.; Lippert, A.; Lee, S. F.; Lavrijsen, R.; Fernández-Pacheco, A. Fabrication of Scaffold-Based 3D Magnetic Nanowires for Domain Wall Applications. *Nanomaterials* **2018**, *8* (7), 483. https://doi.org/10.3390/nano8070483.
(169) Arnold, G.; Winkler, R.; Stermitz, M.; Orthacker, A.; Noh, J.-H.; Fowlkes, J. D.; Kothleitner, G.; Huth, M.; Rack, P. D.; Plank, H. Tunable 3D Nanoresonators for Gas-Sensing Applications. *Adv. Funct. Mater.* **2018**, *28* (19), 1707387. https://doi.org/10.1002/adfm.201707387.
(170) Höflich, K.; Feichtner, T.; Hansjürgen, E.; Haverkamp, C.; Kollmann, H.; Lienau, C.; Silies, M. Resonant Behavior of a Single Plasmonic Helix. *Optica* **2019**, *6* (9), 1098–1105. https://doi.org/10.1364/OPTICA.6.001098.
(171) Kosters, D.; de Hoogh, A.; Zeijlemaker, H.; Acar, H.; Rotenberg, N.; Kuipers, L. Core–Shell Plasmonic Nanohelices. *ACS Photonics* **2017**, *4* (7), 1858–1863. https://doi.org/10.1021/acsphotonics.7b00496.
(172) Benedetti, A.; Alam, B.; Esposito, M.; Tasco, V.; Leahu, G.; Belardini, A.; Li Voti, R.; Passaseo, A.; Sibilia, C. Precise Detection of Circular Dichroism in a Cluster of Nano-Helices by Photoacoustic Measurements. *Sci. Rep.* **2017**, *7* (1), 5257. https://doi.org/10.1038/s41598-017-05193-4.
(173) Esposito, M.; Tasco, V.; Todisco, F.; Benedetti, A.; Sanvitto, D.; Passaseo, A. Three Dimensional Chiral Metamaterial Nanospirals in the Visible Range by Vertically

Compensated Focused Ion Beam Induced-Deposition. *Adv. Opt. Mater.* **2014**, *2* (2), 154–161. https://doi.org/10.1002/adom.201300323.
(174) Esposito, M.; Tasco, V.; Cuscunà, M.; Todisco, F.; Benedetti, A.; Tarantini, I.; Giorgi, M. D.; Sanvitto, D.; Passaseo, A. Nanoscale 3D Chiral Plasmonic Helices with Circular Dichroism at Visible Frequencies. *ACS Photonics* **2015**, *2* (1), 105–114. https://doi.org/10.1021/ph500318p.
(175) Esposito, M.; Tasco, V.; Todisco, F.; Benedetti, A.; Tarantini, I.; Cuscunà, M.; Dominici, L.; Giorgi, M. D.; Passaseo, A. Tailoring Chiro-Optical Effects by Helical Nanowire Arrangement. *Nanoscale* **2015**, *7* (43), 18081–18088. https://doi.org/10.1039/C5NR04674B.
(176) Tasco, V.; Esposito, M.; Todisco, F.; Benedetti, A.; Cuscunà, M.; Sanvitto, D.; Passaseo, A. Three-Dimensional Nanohelices for Chiral Photonics. *Appl. Phys. A* **2016**, *122* (4), 280. https://doi.org/10.1007/s00339-016-9856-6.
(177) Esposito, M.; Tasco, V.; Todisco, F.; Cuscunà, M.; Benedetti, A.; Sanvitto, D.; Passaseo, A. Triple-Helical Nanowires by Tomographic Rotatory Growth for Chiral Photonics. *Nat. Commun.* **2015**, *6* (1), 6484. https://doi.org/10.1038/ncomms7484.
(178) Pakeltis, G.; Hu, Z.; Nixon, A. G.; Mutunga, E.; Anyanwu, C. P.; West, C. A.; Idrobo, J. C.; Plank, H.; Masiello, D. J.; Fowlkes, J. D.; Rack, P. D. Focused Electron Beam Induced Deposition Synthesis of 3D Photonic and Magnetic Nanoresonators. *ACS Appl. Nano Mater.* **2019**, *2* (12), 8075–8082. https://doi.org/10.1021/acsanm.9b02182.
(179) Anyanwu, C. P.; Pakeltis, G.; Rack, P. D.; Masiello, D. J. Nanoscale Characterization of Individual Three-Dimensional Split Ring Resonator Dimers and Trimers. *ACS Appl. Opt. Mater.* **2023**, *XXXX* (XXX), XXX–XXX. https://doi.org/10.1021/acsaom.2c00157.
(180) Kuhness, D.; Gruber, A.; Winkler, R.; Sattelkow, J.; Fitzek, H.; Letofsky-Papst, I.; Kothleitner, G.; Plank, H. High-Fidelity 3D Nanoprinting of Plasmonic Gold Nanoantennas. *ACS Appl. Mater. Interfaces* **2021**, *13* (1), 1178–1191. https://doi.org/10.1021/acsami.0c17030.
(181) Seewald, L. M.; Sattelkow, J.; Brugger-Hatzl, M.; Kothleitner, G.; Frerichs, H.; Schwalb, C.; Hummel, S.; Plank, H. 3D Nanoprinting of All-Metal Nanoprobes for Electric AFM Modes. *Nanomaterials* **2022**, *12* (24), 4477. https://doi.org/10.3390/nano12244477.
(182) Plank, H.; Winkler, R.; Schwalb, C. H.; Hütner, J.; Fowlkes, J. D.; Rack, P. D.; Utke, I.; Huth, M. Focused Electron Beam-Based 3D Nanoprinting for Scanning Probe Microscopy: A Review. *Micromachines* **2020**, *11* (1), 48. https://doi.org/10.3390/mi11010048.
(183) Sattelkow, J.; Fröch, J. E.; Winkler, R.; Hummel, S.; Schwalb, C.; Plank, H. Three-Dimensional Nanothermistors for Thermal Probing. *ACS Appl. Mater. Interfaces* **2019**, *11* (25), 22655–22667. https://doi.org/10.1021/acsami.9b04497.
(184) Utke, I.; Michler, J.; Winkler, R.; Plank, H. Mechanical Properties of 3D Nanostructures Obtained by Focused Electron/Ion Beam-Induced Deposition: A Review. *Micromachines* **2020**, *11* (4), 397. https://doi.org/10.3390/mi11040397.
(185) B. Lewis, B.; A. Mound, B.; Srijanto, B.; D. Fowlkes, J.; M. Pharr, G.; D. Rack, P. Growth and Nanomechanical Characterization of Nanoscale 3D Architectures Grown via

Focused Electron Beam Induced Deposition. *Nanoscale* **2017**, *9* (42), 16349–16356. https://doi.org/10.1039/C7NR05274J.
(186) Baum, T. H.; Jones, C. R. Laser Chemical Vapor Deposition of Gold. *Appl. Phys. Lett.* **1985**, *47* (5), 538–540. https://doi.org/10.1063/1.96119.
(187) Baum, T. H. Laser Chemical Vapor Deposition of Gold: The Effect of Organometallic Structure. *J. Electrochem. Soc.* **1987**, *134* (10), 2616. https://doi.org/10.1149/1.2100254.
(188) Parkhomenko, R. G.; Trubin, S. V.; Turgambaeva, A. E.; Igumenov, I. K. Deposition of Pure Gold Thin Films from Organometallic Precursors. *J. Cryst. Growth* **2015**, *414*, 143–150. https://doi.org/10.1016/j.jcrysgro.2014.09.034.
(189) Xie, H.; Li, Z.; Zhu, J.; Li, C. Atomic Layer Deposition of Gold Nanoparticles with Controlled Size and Distribution on Titania Support. *ChemNanoMat* **2022**, *8* (7), e202200116. https://doi.org/10.1002/cnma.202200116.
(190) Melechko, A. V.; Desikan, R.; McKnight, T. E.; Klein, K. L.; Rack, P. D. Synthesis of Vertically Aligned Carbon Nanofibres for Interfacing with Live Systems. *J. Phys. Appl. Phys.* **2009**, *42* (19), 193001. https://doi.org/10.1088/0022-3727/42/19/193001.
(191) Green, M. A.; Keevers, M. J. Optical Properties of Intrinsic Silicon at 300 K. *Prog. Photovolt. Res. Appl.* **1995**, *3* (3), 189–192. https://doi.org/10.1002/pip.4670030303.
(192) Ergun, S.; Yasinsky, J. B.; Townsend, J. R. Transverse and Longitudinal Optical Properties of Graphite. *Carbon* **1967**, *5* (4), 403–408. https://doi.org/10.1016/0008-6223(67)90057-7.
(193) Butland, A. T. D.; Maddison, R. J. The Specific Heat of Graphite: An Evaluation of Measurements. *J. Nucl. Mater.* **1973**, *49* (1), 45–56. https://doi.org/10.1016/0022-3115(73)90060-3.
(194) Chung, D. D. L. Review Graphite. *J. Mater. Sci.* **2002**, *37* (8), 1475–1489. https://doi.org/10.1023/A:1014915307738.
(195) Ciambriello, L.; Cavaliere, E.; Gavioli, L. Influence of Roughness, Porosity and Grain Morphology on the Optical Properties of Ultrathin Ag Films. *Appl. Surf. Sci.* **2022**, *576*, 151885. https://doi.org/10.1016/j.apsusc.2021.151885.
(196) Klein, K. L.; Melechko, A. V.; McKnight, T. E.; Retterer, S. T.; Rack, P. D.; Fowlkes, J. D.; Joy, D. C.; Simpson, M. L. Surface Characterization and Functionalization of Carbon Nanofibers. *J. Appl. Phys.* **2008**, *103* (6), 061301. https://doi.org/10.1063/1.2840049.
(197) Merkulov, V. I.; Hensley, D. K.; Melechko, A. V.; Guillorn, M. A.; Lowndes, D. H.; Simpson, M. L. Control Mechanisms for the Growth of Isolated Vertically Aligned Carbon Nanofibers. *J. Phys. Chem. B* **2002**, *106* (41), 10570–10577. https://doi.org/10.1021/jp025647f.
(198) Melechko, A. V.; McKnight, T. E.; Hensley, D. K.; Guillorn, M. A.; Borisevich, A. Y.; Merkulov, V. I.; Lowndes, D. H.; Simpson, M. L. Large-Scale Synthesis of Arrays of High-Aspect-Ratio Rigid Vertically Aligned Carbon Nanofibres. *Nanotechnology* **2003**, *14* (9), 1029–1035. https://doi.org/10.1088/0957-4484/14/9/318.
(199) Stanford, M. G.; Mahady, K.; Lewis, B. B.; Fowlkes, J. D.; Tan, S.; Livengood, R.; Magel, G. A.; Moore, T. M.; Rack, P. D. Laser-Assisted Focused He+ Ion Beam

Induced Etching with and without XeF2 Gas Assist. *ACS Appl. Mater. Interfaces* **2016**, *8* (42), 29155–29162. https://doi.org/10.1021/acsami.6b09758.
(200) Singh, U. B.; Pannu, C.; Agarwal, D. C.; Ojha, S.; Khan, S. A.; Ghosh, S.; Avasthi, D. K. Large Electronic Sputtering Yield of Nanodimensional Au Thin Films: Dominant Role of Thermal Conductivity and Electron Phonon Coupling Factor. *J. Appl. Phys.* **2017**, *121* (9), 095308. https://doi.org/10.1063/1.4977845.
(201) Werner, W. S. M.; Glantschnig, K.; Ambrosch-Draxl, C. Optical Constants and Inelastic Electron-Scattering Data for 17 Elemental Metals. *J. Phys. Chem. Ref. Data* **2009**, *38* (4), 1013–1092. https://doi.org/10.1063/1.3243762.
(202) Lasseter, J.; Gellerup, S.; Ghosh, S.; Yun, S. J.; Vasudevan, R.; Unocic, R. R.; Olunloyo, O.; Retterer, S. T.; Xiao, K.; Randolph, S. J.; Rack, P. D. Selected Area Manipulation of MoS2 via Focused Electron Beam-Induced Etching for Nanoscale Device Editing. *ACS Appl. Mater. Interfaces* **2024**. https://doi.org/10.1021/acsami.3c17182.
(203) Mak, K. F.; McGill, K. L.; Park, J.; McEuen, P. L. The Valley Hall Effect in MoS2 Transistors. *Science* **2014**, *344* (6191), 1489–1492. https://doi.org/10.1126/science.1250140.
(204) Sarkar, D.; Liu, W.; Xie, X.; Anselmo, A. C.; Mitragotri, S.; Banerjee, K. MoS2 Field-Effect Transistor for Next-Generation Label-Free Biosensors. *ACS Nano* **2014**, *8* (4), 3992–4003. https://doi.org/10.1021/nn5009148.
(205) Li, H.; Wu, J.; Yin, Z.; Zhang, H. Preparation and Applications of Mechanically Exfoliated Single-Layer and Multilayer MoS2 and WSe2 Nanosheets. *Acc. Chem. Res.* **2014**, *47* (4), 1067–1075. https://doi.org/10.1021/ar4002312.
(206) Zeng, M.; Xiao, Y.; Liu, J.; Yang, K.; Fu, L. Exploring Two-Dimensional Materials toward the Next-Generation Circuits: From Monomer Design to Assembly Control. *Chem. Rev.* **2018**, *118* (13), 6236–6296. https://doi.org/10.1021/acs.chemrev.7b00633.
(207) Sachid, A. B.; Tosun, M.; Desai, S. B.; Hsu, C.-Y.; Lien, D.-H.; Madhvapathy, S. R.; Chen, Y.-Z.; Hettick, M.; Kang, J. S.; Zeng, Y.; He, J.-H.; Chang, E. Y.; Chueh, Y.-L.; Javey, A.; Hu, C. Monolithic 3D CMOS Using Layered Semiconductors. *Adv. Mater.* **2016**, *28* (13), 2547–2554. https://doi.org/10.1002/adma.201505113.
(208) Kim, M.; Seo, J.; Kim, J.; Moon, J. S.; Lee, J.; Kim, J.-H.; Kang, J.; Park, H. High-Crystalline Monolayer Transition Metal Dichalcogenides Films for Wafer-Scale Electronics. *ACS Nano* **2021**, *15* (2), 3038–3046. https://doi.org/10.1021/acsnano.0c09430.
(209) Chubarov, M.; Choudhury, T. H.; Hickey, D. R.; Bachu, S.; Zhang, T.; Sebastian, A.; Bansal, A.; Zhu, H.; Trainor, N.; Das, S.; Terrones, M.; Alem, N.; Redwing, J. M. Wafer-Scale Epitaxial Growth of Unidirectional WS2 Monolayers on Sapphire. *ACS Nano* **2021**, *15* (2), 2532–2541. https://doi.org/10.1021/acsnano.0c06750.
(210) Choudhary, N.; Islam, M. A.; Kim, J. H.; Ko, T.-J.; Schropp, A.; Hurtado, L.; Weitzman, D.; Zhai, L.; Jung, Y. Two-Dimensional Transition Metal Dichalcogenide Hybrid Materials for Energy Applications. *Nano Today* **2018**, *19*, 16–40. https://doi.org/10.1016/j.nantod.2018.02.007.

(211) Haas, J.; Ulrich, F.; Hofer, C.; Wang, X.; Braun, K.; Meyer, J. C. Aligned Stacking of Nanopatterned 2D Materials for High-Resolution 3D Device Fabrication. *ACS Nano* **2022**, *16* (2), 1836–1846. https://doi.org/10.1021/acsnano.1c09122.
(212) Liu, Y.; Nan, H.; Wu, X.; Pan, W.; Wang, W.; Bai, J.; Zhao, W.; Sun, L.; Wang, X.; Ni, Z. Layer-by-Layer Thinning of MoS2 by Plasma. *ACS Nano* **2013**, *7* (5), 4202–4209. https://doi.org/10.1021/nn400644t.
(213) Zhang, R.; Drysdale, D.; Koutsos, V.; Cheung, R. Controlled Layer Thinning and P-Type Doping of WSe2 by Vapor XeF2. *Adv. Funct. Mater.* **2017**, *27* (41), 1702455. https://doi.org/10.1002/adfm.201702455.
(214) Yao, G.; Zhao, D.; Hong, Y.; Wu, S.; Liu, D.; Qiu, M. Direct Electron-Beam Patterning of Monolayer MoS2 with Ice. *Nanoscale* **2020**, *12* (44), 22473–22477. https://doi.org/10.1039/D0NR05948J.
(215) Yao, G.; Zhao, D.; Hong, Y.; Zheng, R.; Qiu, M. Ice-Assisted Electron-Beam Lithography for MoS2 Transistors with Extremely Low-Energy Electrons. *Nanoscale Adv.* **2022**, *4* (11), 2479–2483. https://doi.org/10.1039/D2NA00159D.
(216) Wei, Z.; Liao, M.; Guo, Y.; Tang, J.; Cai, Y.; Chen, H.; Wang, Q.; Jia, Q.; Lu, Y.; Zhao, Y.; Liu, J.; Chu, Y.; Yu, H.; Li, N.; Yuan, J.; Huang, B.; Shen, C.; Yang, R.; Shi, D.; Zhang, G. Scratching Lithography for Wafer-Scale MoS2 Monolayers. *2D Mater.* **2020**, *7* (4), 045028. https://doi.org/10.1088/2053-1583/aba99f.
(217) Rani, E.; Wong, L. S. High-Resolution Scanning Probe Nanolithography of 2D Materials: Novel Nanostructures. *Adv. Mater. Technol.* **2019**, *4* (7), 1900181. https://doi.org/10.1002/admt.201900181.
(218) Chen, X.; Kohring, M.; Assebban, M.; Tywoniuk, B.; Bartlam, C.; Moses Badlyan, N.; Maultzsch, J.; Duesberg, G. S.; Weber, H. B.; Knirsch, K. C.; Hirsch, A. Covalent Patterning of 2D MoS2. *Chem. – Eur. J.* **2021**, *27* (52), 13117–13122. https://doi.org/10.1002/chem.202102021.
(219) Gobbi, M.; Bonacchi, S.; Lian, J. X.; Vercouter, A.; Bertolazzi, S.; Zyska, B.; Timpel, M.; Tatti, R.; Olivier, Y.; Hecht, S.; Nardi, M. V.; Beljonne, D.; Orgiu, E.; Samorì, P. Collective Molecular Switching in Hybrid Superlattices for Light-Modulated Two-Dimensional Electronics. *Nat. Commun.* **2018**, *9* (1), 2661. https://doi.org/10.1038/s41467-018-04932-z.
(220) Gao, Y.; Wang, S.; Wang, B.; Jiang, Z.; Fang, T. Recent Progress in Phase Regulation, Functionalization, and Biosensing Applications of Polyphase MoS2. *Small* **2022**, *18* (34), 2202956. https://doi.org/10.1002/smll.202202956.
(221) Hu, L.; Shan, X.; Wu, Y.; Zhao, J.; Lu, X. Laser Thinning and Patterning of MoS2 with Layer-by-Layer Precision. *Sci. Rep.* **2017**, *7* (1), 15538. https://doi.org/10.1038/s41598-017-15350-4.
(222) Thiruraman, J. P.; Masih Das, P.; Drndić, M. Irradiation of Transition Metal Dichalcogenides Using a Focused Ion Beam: Controlled Single-Atom Defect Creation. *Adv. Funct. Mater.* **2019**, *29* (52), 1904668. https://doi.org/10.1002/adfm.201904668.
(223) Jadwiszczak, J.; Keane, D.; Maguire, P.; Cullen, C. P.; Zhou, Y.; Song, H.; Downing, C.; Fox, D.; McEvoy, N.; Zhu, R.; Xu, J.; Duesberg, G. S.; Liao, Z.-M.; Boland, J. J.; Zhang, H. MoS2 Memtransistors Fabricated by Localized Helium Ion Beam

Irradiation. *ACS Nano* **2019**, *13* (12), 14262–14273. https://doi.org/10.1021/acsnano.9b07421.
(224) Randolph, S. J.; Fowlkes, J. D.; Rack, P. D. Focused Electron-Beam-Induced Etching of Silicon Dioxide. *J. Appl. Phys.* **2005**, *98* (3), 034902. https://doi.org/10.1063/1.1991976.
(225) Stanford, M. G.; Pudasaini, P. R.; Cross, N.; Mahady, K.; Hoffman, A. N.; Mandrus, D. G.; Duscher, G.; Chisholm, M. F.; Rack, P. D. Tungsten Diselenide Patterning and Nanoribbon Formation by Gas-Assisted Focused-Helium-Ion-Beam-Induced Etching. *Small Methods* **2017**, *1* (4), 1600060. https://doi.org/10.1002/smtd.201600060.
(226) Stanford, M. G.; Mahady, K.; Lewis, B. B.; Fowlkes, J. D.; Tan, S.; Livengood, R.; Magel, G. A.; Moore, T. M.; Rack, P. D. Laser-Assisted Focused He+ Ion Beam Induced Etching with and without XeF2 Gas Assist. *ACS Appl. Mater. Interfaces* **2016**, *8* (42), 29155–29162. https://doi.org/10.1021/acsami.6b09758.
(227) Schoenaker, F. J.; Córdoba, R.; Fernández-Pacheco, R.; Magén, C.; Stéphan, O.; Zuriaga-Monroy, C.; Ibarra, M. R.; Teresa, J. M. D. Focused Electron Beam Induced Etching of Titanium with XeF2. *Nanotechnology* **2011**, *22* (26), 265304. https://doi.org/10.1088/0957-4484/22/26/265304.
(228) Ganczarczyk, A.; Geller, M.; Lorke, A. XeF2 Gas-Assisted Focused-Electron-Beam-Induced Etching of GaAs with 30 Nm Resolution. *Nanotechnology* **2010**, *22* (4), 045301. https://doi.org/10.1088/0957-4484/22/4/045301.
(229) Gonzalez, C. M.; Slingenbergh, W.; Timilsina, R.; Noh, J.-H.; Stanford, M. G.; Lewis, B. B.; Klein, K. L.; Liang, T.; Fowlkes, J. D.; Rack, P. D. Evaluation of Mask Repair Strategies via Focused Electron, Helium, and Neon Beam Induced Processing for EUV Applications. In *Extreme Ultraviolet (EUV) Lithography V*; SPIE, 2014; Vol. 9048, pp 135–141. https://doi.org/10.1117/12.2046712.
(230) Boden, S. A.; Moktadir, Z.; Bagnall, D. M.; Mizuta, H.; Rutt, H. N. Focused Helium Ion Beam Milling and Deposition. *Microelectron. Eng.* **2011**, *88* (8), 2452–2455. https://doi.org/10.1016/j.mee.2010.11.041.
(231) Randolph, S.; Toth, M.; Cullen, J.; Chandler, C.; Lobo, C. Kinetics of Gas Mediated Electron Beam Induced Etching. *Appl. Phys. Lett.* **2011**, *99* (21), 213103. https://doi.org/10.1063/1.3662928.
(232) Martin, A. A.; McCredie, G.; Toth, M. Electron Beam Induced Etching of Carbon. *Appl. Phys. Lett.* **2015**, *107* (4), 041603. https://doi.org/10.1063/1.4927593.
(233) Taniguchi, J. T. J.; Miyamoto, I. M. I.; Ohno, N. O. N.; Honda, S. H. S. Electron Beam Assisted Chemical Etching of Single Crystal Diamond Substrates. *Jpn. J. Appl. Phys.* **1996**, *35* (12S), 6574. https://doi.org/10.1143/JJAP.35.6574.
(234) Rack, P. D.; Randolph, S.; Deng, Y.; Fowlkes, J.; Choi, Y.; Joy, D. C. Nanoscale Electron-Beam-Stimulated Processing. *Appl. Phys. Lett.* **2003**, *82* (14), 2326–2328. https://doi.org/10.1063/1.1565696.
(235) Edinger, K.; Becht, H.; Bihr, J.; Boegli, V.; Budach, M.; Hofmann, T.; Koops, H. W. P.; Kuschnerus, P.; Oster, J.; Spies, P.; Weyrauch, B. Electron-Beam-Based Photomask Repair. *J. Vac. Sci. Technol. B Microelectron. Nanometer Struct. Process. Meas. Phenom.* **2004**, *22* (6), 2902–2906. https://doi.org/10.1116/1.1808711.

(236) Liang, T.; Stivers, A. R. Damage-Free Mask Repair Using Electron-Beam-Induced Chemical Reactions; Engelstad, R. L., Ed.; Santa Clara, CA, 2002; p 375. https://doi.org/10.1117/12.472312.
(237) Noh, J. H.; Fowlkes, J. D.; Timilsina, R.; Stanford, M. G.; Lewis, B. B.; Rack, P. D. Pulsed Laser-Assisted Focused Electron-Beam-Induced Etching of Titanium with XeF2: Enhanced Reaction Rate and Precursor Transport. *ACS Appl. Mater. Interfaces* **2015**, *7* (7), 4179–4184. https://doi.org/10.1021/am508443s.
(238) J. Urbanos, F.; Black, A.; Bernardo-Gavito, R.; Parga, A. L. V. de; Miranda, R.; Granados, D. Electrical and Geometrical Tuning of MoS 2 Field Effect Transistors via Direct Nanopatterning. *Nanoscale* **2019**, *11* (23), 11152–11158. https://doi.org/10.1039/C9NR02464F.
(239) Huang, Y.; Wu, J.; Xu, X.; Ho, Y.; Ni, G.; Zou, Q.; Koon, G. K. W.; Zhao, W.; Castro Neto, A. H.; Eda, G.; Shen, C.; Özyilmaz, B. An Innovative Way of Etching MoS2: Characterization and Mechanistic Investigation. *Nano Res.* **2013**, *6* (3), 200–207. https://doi.org/10.1007/s12274-013-0296-8.
(240) Chen, S.; Kim, S.; Chen, W.; Yuan, J.; Bashir, R.; Lou, J.; van der Zande, A. M.; King, W. P. Monolayer MoS2 Nanoribbon Transistors Fabricated by Scanning Probe Lithography. *Nano Lett.* **2019**, *19* (3), 2092–2098. https://doi.org/10.1021/acs.nanolett.9b00271.
(241) Son, J.; Kwon, J.; Kim, S.; Lv, Y.; Yu, J.; Lee, J.-Y.; Ryu, H.; Watanabe, K.; Taniguchi, T.; Garrido-Menacho, R.; Mason, N.; Ertekin, E.; Huang, P. Y.; Lee, G.-H.; M. Van Der Zande, A. Atomically Precise Graphene Etch Stops for Three Dimensional Integrated Systems from Two Dimensional Material Heterostructures. *Nat. Commun.* **2018**, *9* (1), 3988. https://doi.org/10.1038/s41467-018-06524-3.
(242) Ryu, H.; Kim, D.; Kwon, J.; Park, S. K.; Lee, W.; Seo, H.; Watanabe, K.; Taniguchi, T.; Kim, S.; Van Der Zande, A. M.; Son, J.; Lee, G. Fluorinated Graphene Contacts and Passivation Layer for MoS $_2$ Field Effect Transistors. *Adv. Electron. Mater.* **2022**, *8* (10), 2101370. https://doi.org/10.1002/aelm.202101370.
(243) Friedli, V.; Utke, I. Optimized Molecule Supply from Nozzle-Based Gas Injection Systems for Focused Electron- and Ion-Beam Induced Deposition and Etching: Simulation and Experiment. *J. Phys. Appl. Phys.* **2009**, *42* (12), 125305. https://doi.org/10.1088/0022-3727/42/12/125305.
(244) Winkler, R.; Fowlkes, J.; Szkudlarek, A.; Utke, I.; Rack, P. D.; Plank, H. The Nanoscale Implications of a Molecular Gas Beam during Electron Beam Induced Deposition. *ACS Appl. Mater. Interfaces* **2014**, *6* (4), 2987–2995. https://doi.org/10.1021/am405591d.
(245) Weaver, C. F.; Friedman, H. A. *LITERATURE SURVEY OF THE FLUORIDES AND OXYFLUORIDES OF MOLYBDENUM.*; ORNL-TM-1976; Oak Ridge National Lab. (ORNL), Oak Ridge, TN (United States), 1967. https://doi.org/10.2172/4209093.
(246) Farigliano, L. M.; Paredes-Olivera, P. A.; Patrito, E. M. Ab-Initio Molecular Dynamics Simulations of the Reactivity of MoS2 towards F2 Molecules: Implications for Etching Processes. *Appl. Surf. Sci.* **2023**, *607*, 154637. https://doi.org/10.1016/j.apsusc.2022.154637.

(247) Ke, J.-A.; Garaj, S.; Gradečak, S. Nanopores in 2D MoS2: Defect-Mediated Formation and Density Modulation. *ACS Appl. Mater. Interfaces* **2019**, *11* (29), 26228–26234. https://doi.org/10.1021/acsami.9b03531.
(248) Parkin, W. M.; Balan, A.; Liang, L.; Das, P. M.; Lamparski, M.; Naylor, C. H.; Rodríguez-Manzo, J. A.; Johnson, A. T. C.; Meunier, V.; Drndić, M. Raman Shifts in Electron-Irradiated Monolayer MoS2. *ACS Nano* **2016**, *10* (4), 4134–4142. https://doi.org/10.1021/acsnano.5b07388.
(249) Stanford, M. G.; Pudasaini, P. R.; Belianinov, A.; Cross, N.; Noh, J. H.; Koehler, M. R.; Mandrus, D. G.; Duscher, G.; Rondinone, A. J.; Ivanov, I. N.; Ward, T. Z.; Rack, P. D. Focused Helium-Ion Beam Irradiation Effects on Electrical Transport Properties of Few-Layer WSe2: Enabling Nanoscale Direct Write Homo-Junctions. *Sci. Rep.* **2016**, *6* (1), 27276. https://doi.org/10.1038/srep27276.
(250) Lin, W.; Li, Q.; Belianinov, A.; Sales, B. C.; Sefat, A.; Gai, Z.; Baddorf, A. P.; Pan, M.; Jesse, S.; Kalinin, S. V. Local Crystallography Analysis for Atomically Resolved Scanning Tunneling Microscopy Images. *Nanotechnology* **2013**, *24* (41), 415707. https://doi.org/10.1088/0957-4484/24/41/415707.
(251) Berg, S.; Kutra, D.; Kroeger, T.; Straehle, C. N.; Kausler, B. X.; Haubold, C.; Schiegg, M.; Ales, J.; Beier, T.; Rudy, M.; Eren, K.; Cervantes, J. I.; Xu, B.; Beuttenmueller, F.; Wolny, A.; Zhang, C.; Koethe, U.; Hamprecht, F. A.; Kreshuk, A. Ilastik: Interactive Machine Learning for (Bio)Image Analysis. *Nat. Methods* **2019**, *16* (12), 1226–1232. https://doi.org/10.1038/s41592-019-0582-9.
(252) He, Z.; Zhao, R.; Chen, X.; Chen, H.; Zhu, Y.; Su, H.; Huang, S.; Xue, J.; Dai, J.; Cheng, S.; Liu, M.; Wang, X.; Chen, Y. Defect Engineering in Single-Layer MoS2 Using Heavy Ion Irradiation. *ACS Appl. Mater. Interfaces* **2018**, *10* (49), 42524–42533. https://doi.org/10.1021/acsami.8b17145.
(253) Matsunaga, M.; Higuchi, A.; He, G.; Yamada, T.; Krüger, P.; Ochiai, Y.; Gong, Y.; Vajtai, R.; Ajayan, P. M.; Bird, J. P.; Aoki, N. Nanoscale-Barrier Formation Induced by Low-Dose Electron-Beam Exposure in Ultrathin MoS2 Transistors. *ACS Nano* **2016**, *10* (10), 9730–9737. https://doi.org/10.1021/acsnano.6b05952.
(254) Komsa, H.-P.; Kurasch, S.; Lehtinen, O.; Kaiser, U.; Krasheninnikov, A. V. From Point to Extended Defects in Two-Dimensional MoS$\{\}_\{2\}$: Evolution of Atomic Structure under Electron Irradiation. *Phys. Rev. B* **2013**, *88* (3), 035301. https://doi.org/10.1103/PhysRevB.88.035301.
(255) Nan, H.; Wang, Z.; Wang, W.; Liang, Z.; Lu, Y.; Chen, Q.; He, D.; Tan, P.; Miao, F.; Wang, X.; Wang, J.; Ni, Z. Strong Photoluminescence Enhancement of MoS2 through Defect Engineering and Oxygen Bonding. *ACS Nano* **2014**, *8* (6), 5738–5745. https://doi.org/10.1021/nn500532f.
(256) Chakraborty, B.; Bera, A.; Muthu, D. V. S.; Bhowmick, S.; Waghmare, U. V.; Sood, A. K. Symmetry-Dependent Phonon Renormalization in Monolayer MoS2 Transistor. *Phys. Rev. B* **2012**.
(257) Wei, X.; Yu, Z.; Hu, F.; Cheng, Y.; Yu, L.; Wang, X.; Xiao, M.; Wang, J.; Wang, X.; Shi, Y. Mo-O Bond Doping and Related-Defect Assisted Enhancement of Photoluminescence in Monolayer MoS2. *AIP Adv.* **2014**, *4* (12), 123004. https://doi.org/10.1063/1.4897522.

(258) Baidoo, J. K.; Choi, S. H.; Agyapong-Fordjour, F. O.-T.; Boandoh, S.; Yun, S. J.; Adofo, L. A.; Ben-Smith, A.; Kim, Y. I.; Jin, J. W.; Jung, M.-H.; Jeong, H. Y.; Kim, Y.-M.; Lee, Y. H.; Kim, S. M.; Kim, K. K. Sequential Growth of Vertical Transition-Metal Dichalcogenide Heterostructures on Rollable Aluminum Foil. *ACS Nano* **2022**, *16* (6), 8851–8859. https://doi.org/10.1021/acsnano.1c10233.

VITA

John Lasseter was born in Raleigh, North Carolina but moved to Murfreesboro Tennessee when he was a young child. He attended Middle Tennessee State University for his undergrad in computer science and chemistry, with a minor in mathematics. He was mentored by Philip Rack, and advised by Steven Randolph during his Ph. D studies centering around direct-write processes in electron microscopes with the majority of his work performed at the Center for Nanophase Materials Science, at Oak Ridge National Lab.